Simulation, Preparation and Characterisation of Magnetocaloric Thin Films

Alex Evans

PhD Thesis submitted for the degree of
Doctor of Philosophy in Physical Science

School of Physics and Astronomy

Cardiff University

15 Dec 2021

Abstract

Heisenberg and related models have previously been developed to investigate the magnetocaloric effect. Here an Ising model was developed to simulate the GdSiGe crystal system and used to compare the two dominant phases, monoclinic and orthorhombic, to show a dependence on the inter slab bonding that is present in the orthorhombic phase but not the monoclinic phase and the T_c. The model uniquely utilises 2 Ising models, representing each phase, to compare internal energies and derive a first-order phase change point. The Monte Carlo (MC) method with consideration for only nearest neighbour sites, magnetic coupling strength (J) calculated using the Ruderman-Kittel-Kasuya-Yosida (RKKY) model and an external field H was applied. The cohesive energy, under the assumption of the nearly free electron, was used to show indistinguishability in favour of individual phases. This indistinguishability leads to a first-order coupled magnetic and structural transition over a second-order magnetic transition usually expected from Ising models.

Thin-film Magnetocaloric GdSiGe and LaFeCoSi were grown on SiO_2 and AlN, SQUID and VSM magnetometry are used to investigate the phase transition and Curie temperature. X-ray, polarised neutron reflectometry and AFM measurements are used to investigate the structural and surface characteristics. For both materials, there exists a distinct change compared to their bulk coun-

terpart.

The Curie temperature of both materials moved from the bulk counterparts, with LaFeCoSi having an $\sim$ 8 K lower T_c and GdSiGe an up to 13 K higher T_c. A maximum entropy change for GdSiGe thin film was found to be 0.45 $JkgK^{-1} \pm$ 0.14 $JkgK^{-1}$ for a 0 to 5T field change, smaller than the bulk counterpart at 40.2 $JkgK^{-1}$ also for a change of 5 T [1] but at a higher T_c, the optimal growth temperature of the GdSiGe sample with the most significant entropy change was also not at the expected point based on theory. With the maximum monoclinic phase present at 553K being the expected optimum temperature but maximum entropy was found for the sample grown at 503K.

Using surface, structural and magnetic measurements, optimum temperature and growth parameters are determined, and a complex, layered, magnetic structure is shown to exist due to surface and interface effects. The optimal temperature for deposition of GdSiGe was found to be 503K and a 20mTorr Ar chamber pressure. LaFeCoSi thin films are found to have a maximum entropy change response when deposited at 293 K, the lowest possible temperature in the PLD system used. The actual optimum deposition temperature is possibly lower due to the increased stability of the $NaZn_{13}$ structure at lower temperatures.

Thin-film LaFeCoSi also has an entropy change different from its bulk counterpart, with a lower T_c, a maximum entropy change value found to be 1.394 $JkgK^{-1}\pm$ 0.34 and a negative entropy change of the same magnitude at a much lower temperature of 220 K-240 K.

There are also changes in the materials' magnetic and thermal hysteresis with some thin-film GdSiGe samples showing almost no thermal hysteresis but LaFeCoSi samples universally having an increased coercivity.

To my funders, supervisors, school, colleagues, family and friends.

Thank you.

Supporting Publications, Presentations and Posters

- RAMS conference 2018, "The Ising Model for the Study of $Gd_5(Si_xGe_{1-x})_4$", A. Evans[1], D. Read[1], G. Min[2], September 2018, [Poster]

- ISIS User Meeting 2019, "Ising Model Calculations of the Monoclinic and Orthorhombic Phases in Magnetocaloric $Gd_5(Si_xGe_{1-x})_4$", A. Evans[1], D. Read[1], G. Min[2], April 2019, [Poster]

- Magnetism 2019, "Ising Model Calculations of the Monoclinic and Orthorhombic Phases in Magnetocaloric $Gd_5(Si_xGe_{1-x})_4$", A. Evans[1], D. Read[1], G. Min[2], February 2019, [Poster]

- MMM 2019, "Ising Model Simulations of the Magnetocaloric Material $Gd_5(Si_xGe_{1-x})_4$", A. Evans[1], D. Read[1], G. Min[2], November 2019, [Poster]

- MMM 2019, "Structural and magnetic phase transition coupling in magnetocaloric $LaFeCoSi$ thin films ", A. Evans[1], D. Read[1], G. Min[2], November 2019, [Poster]

- "Toward Improved Environmental Stability of Polymer: Fullerene and Polymer:Nonfullerene Organic Solar Cells: A Common Energetic Origin of Light-

and Oxygen-Induced Degradation", ACS Energy Lett. 2019, 4, 846-852, *E. M. Speller*[3], *A. J. Clarke*[3], *A. Evans*[1], [Publication]

- "Fluorine doped tin oxide as an alternative of indium tin oxide for bottom electrode of semi-transparent organic photovoltaic devices", AIP Advances 9, 085220 (2019) *A. Way*[3], *J. Luke*[3], *A. Evans*[1], [Publication]

1. School of Physics and Astronomy, Cardiff University, The Parade, Cardiff, CF23 3AA, United Kingdom

2. School of Engineering, Cardiff University, The Parade, Cardiff, CF23 3AA, United Kingdom

3. SPECIFIC, College of Engineering, Swansea University, Bay Campus, Fabian Way, Swansea SA1 8EN, United Kingdom

Contents

List of Figures

xiii

List of Tables

Introduction

The Magnetocaloric Effect (MCE) is the adiabatic change in temperature of a material as a function of the change in an external magnetic field, hence the name *Magneto* relating to Magnetism and *Caloric* relating to Heat. The effect arises from the balancing of the magnetic, electronic and lattice entropies of the system during an adiabatic process. Where a decrease in the magnetic entropy would be negated by an increase in the others which is usually most noticeable in the lattice entropy resulting in a measurable temperature change. Materials that exhibit the MCE are usually part of a larger group of materials known as multi-caloric materials [11, 12], these materials' adiabatic temperature change is driven by either the magnetocaloric (external magnetic field-based), barocaloric

(pressure/stress/strain-based) or electrocaloric (electric field-based) effects or a combination of the three.

The MCE was first discovered by Emil Warburg in 1881 [13] in iron but did not gain more interest until the early 20th century when Debye suggested using the MCE to reach temperatures below 4K [14]. Later, Giauque [15] was awarded a Nobel Prize in Chemistry for achieving temperatures $< 1\ K$ by using this process with $Gd_2(SO_4)_3.8H_2O$, low-temperature physicists have come to know the effect as "adiabatic demagnetisation cooling". Given the higher heat capacity requirements, room temperature applications wouldn't prove viable until 1976 when Brown showed Gd could be applicable with a room temperature transition [16]. The increased heat capacity of room temperature magnetocaloric materials would mean materials with increased entropy changes at the transition would be targeted to increase ΔT. But the major breakthrough in the room temperature MCE field came in 1997 when Pecharsky and Gschneider published work on the first $Gd_5(Si_{1-x}Ge_x)_4$ system, $Gd_5Si_2Ge_2$, showing what was dubbed the Giant Magnetocaloric Effect (GMCE)[3]. The GMCE source was shown to be a coupling between the magnetic and crystallographic phase change, where a series of Si/Ge bonds existing in a ferromagnetic orthorhombic layered structure are sheared during the lateral movement of the layers transitioning to a paramagnetic monoclinic system, giving a response far superior to previous materials and increasing the availability for research in the MCE field. Later, coupling a multicaloric like effect with a crystallographic phase change would lead to the discovery of the Giant Electrocaloric Effect (GECE) which is analogous to the GMCE but less investigated or exploited.

Conventional refrigeration takes advantage of Vapour-Compression Refrigeration Systems (VCRS), which is the cyclic compression and decompression of a fluid or gas. The fluid or gas is moved to be in contact with the desired object during its cold, decompressed stage and moved to dump excess heat in its

compressed stage [4]. Although this technology has become very cost-effective, it has reached very close to its theoretical upper efficiencies, limiting available research and advancements in the area. The damage chlorofluorocarbons (CFCs) cause to the ozone has meant newer VCRS now use alternatives such as hydro-chlorofluorocarbons (HCFCs) and hydro-fluorocarbons (HFCs), these materials although less damaging still are contributing to environmental damage and are set to be phased out under the Montreal Protocol and further EU regulation. MCE materials show promise as a replacement for VCRS based systems for several reasons; materials used tend to be non-toxic, non-destructive to the environment, show potential for a higher refrigeration efficiency, due to their solid nature can be more compact requiring less material and less prone to failure. MCs have the potential to vastly improve the efficiency of cooling systems by reducing the number of moving parts and by having an improved theoretical Carnot efficiency by up to 50%, MCs would also not require the use of environmentally harmful gases in the cooling apparatus, unlike the current compressor-based systems[4, 17].

Several prototypes and simulated cooling systems have been created as proof of concept that these materials are a viable alternative to pressure cooling, although none have yet to go into production and further research into optimising the chosen bulk material is still required[18, 19, 20].

MCs also have the potential to be miniaturised and embedded in much smaller systems than freezers and coolers. Miniaturisation would allow greater temperature control of some more advanced electronic systems such as mobile phones. At the moment this is strictly theoretical, and as of yet, there is no documented small electronic system containing a magnetocaloric material.

$Gd_5(Si_{1-x}Ge_x)_4$ systems are among the most studied MCE materials at room temperature due to their being described early by Pecharsky and Gschneider, their high degree of response and interesting phase transition that appears to be reasonably resilient to doping [3]. Many Gd based working refrigeration units

have been produced and tested due to their Curie temperature ~ 294 K but the field is still lacking in the nanoscale region. There is some research into powdered $Gd_5(Si_{1-x}Ge_x)_4$ showing a significant reduction in its response [21] as well as one group headed by Ravi Hadimani showing successful thin-film fabrication [22].

$La(Fe_{1-x}Si_x)_{13}$ systems, although entered research later than that of $Gd_5(Si_{1-x}Ge_x)_4$ have also become of particular interest. Due mainly to the interesting magnetic and thermal hysteresis, or lack thereof present within the material. $La(Fe_{1-x}Si_x)_{13}$ has an interesting phase structure that is difficult to achieve and is prone to develop secondary phases [4]. The nature of the transition differs significantly from $Gd_5(Si_{1-x}Ge_x)_4$ as well, in that it is both an isotropic expansion over the transition not a magnetostructural change and an itinerant electron metamagnetic transition. Rare Earth (RE) metals have become prominent throughout the MCE field due to their significant moment and many having tunable Curie temperatures close to room temperature when doped. Their high expense is proving to be a problem for the field, but lanthanum based systems are a hopeful remedy to this due to their abundance when compared to other RE materials.

1.1 Aim of the Research

The research will aim to investigate the effects of thin-film deposition upon magnetocaloric materials further and draw a comparison with the bulk counterpart. $Gd_5(Si_{1-x}Ge_x)_4$ and $La(Fe_{1-x-y}Co_ySi_x)_{13}$ are materials of interest as they undergo a first-order phase transition, near to room temperature, making them ideal for real-world applications.

Both $Gd_5(Si_{1-x}Ge_x)_4$ and $La(Fe_{1-x-y}Co_ySi_x)_{13}$, although being magnetocaloric materials, have an altered effect when under pressure or strained in some form due to the MCE in both phase transitions being magnetic and structurally coupled,

so we also investigate the structural effects and interactions at interfaces.

Further investigation into nanoengineering of magnetocalorics has been attempted before but has been purely exploratory [23]. The effects of further reducing the dimensions of the material may prove to be of interest to the research and are investigated.

Simulations using Ising models to replicate the effect driving the transition are created to help better understand the transition, what drives it, and any potential limitations of the materials. We replicate the MCE within $Gd_5(Si_{1-x}Ge_x)_4$ by investigating both the high and low temperature phases and comparing the internal energy.

Theory

2.1 Phase Transitions

A material is said to be in a particular phase if several thermodynamic charac-
teristics exist, the main one being that they are uniform on the microscopic level.
External and internal changes can induce a shift in a thermodynamic property
causing a system to transition from one phase to another. A simple example is
the transition of water to ice and vice versa, whereby water is in an initial liquid
phase which changes to a solid phase and back again. Solid to solid phases are
possible, water ice itself can take the form of one of 17 known solid phases [24]
dependent upon factors such as pressure and temperature.

A phase transition can be broadly described as one of two regimes first described by Ehrenfest, a First-Order Phase Transition (FOPT), or a Second-Order Phase Transition (SOPT) sometimes known as a continuous transition. The main difference being the nature of the change, FOPTs have a sudden discontinuity in the first derivative of the free energy with respect to some other thermodynamic property where one phase is abruptly ended at a critical temperature (T_{crit}), and there is an associated latent heat. SOPTs have a continuous change from one phase to another and a continuous first derivative, but a discontinuous second derivative about the T_{crit} where both phases will coexist in diminishing quantities on either side of the phase transition. Morrison et al. have shown the existence of both FOPT and SOPT transitions in a single CoMnSiGe system, where a tricritical temperature of 262 K exists, below which the transition is FOPT with a latent heat. Above 262 K the transition is continuous [25].

FOPT transitions as a result of the latent heat are not strictly reversible, as there is an energy barrier to return to previous phases. During an adiabatic transition, this is usually seen as a change in internal temperature as phonon energy is absorbed. Due to the barrier near the T_{crit} of a FOPT many stochastic metastable phases exist and these states fluctuate in size and at a critical nucleation will grow to form a new dominant phase in the system. The rate of growth is generally much faster than the nucleation rate (the time taken for critical nuclei to form) and both are heavily affected by impurities within the system. The nucleation phase also may not always be the final phase the system comes to be stable in, but a precursory metastable phase [26].

Phase changes are a complex problem that can occur due to many competing external factors such as temperature, pressure, magnetic fields and electric fields, but can be simplified if the system is said to go from an ordered to a disordered state. In this system, a selected order parameter, usually one that is measurable in both phase states with a known value before the transition and a vanishing value

afterwards can be used. Within a ferromagnetic system undergoing a transition the net magnetisation can be used as an order parameter, liquid to gas transitions can use the density. Other methods for describing a phase change involve energy calculations of the two phases as a function of one of the external factors and finding a point of intersection of the energies corresponding to a critical point [27, 28].

2.2 Magnetism

This section will give an overview of the theory and origin of magnetism.

Magnetism in materials will arise from the electrons within the system, be it localised electrons or itinerant electrons organised to have a net non-zero magnetic moment, spontaneously or driven by an external field. Atomic nuclei will also produce a magnetic field, but it is several orders of magnitude smaller than that produced by the electrons.

Classically, explaining magnetism as a whole has not been done, Niels Bohr first showed this in 1911 [29] using statistics to describe how a thermally active average moment will always tend to zero. Thus a quantum-mechanical understanding, principally of the Pauli exclusion principle is needed.

The Pauli exclusion principle states that two fermions cannot be in the same quantum state, i.e. cannot share both their spatial and spin state. Thus there can only be two electrons for a single spatial state, and they must have opposite spin states. Hunds' rule also states that every orbital within a sub-level will fill singly before double occupancy and that all singly occupied orbitals will have the same spin.

In a system where the remaining unpaired orbitals can align a magnetic moment can be measured. An itinerant magnetic system gains its moment through different mechanisms but with a similar outcome, that being the aligning of elec-

tron moments. Within an Itinerant system the outer electrons move almost independently from their core and form an electron gas. The correlation of the moments of the electrons is then the contributing factor to both the materials' magnetism and electronic conduction. Counter-intuitively, one would assume a disordered moment would provide a lower energy level, however, in some systems, due to the associated energy from an interaction between the molecular field and the electron gas magnetisation, the energy cost of ordering moments is reduced overall [30].

Materials have spontaneous magnetisation if a given amount of magnetic moments all lie in a shared orientation to one another, and they can be sub-categorised by their response to external magnetic fields. The types of magnetism most commonly found are Diamagnetism, Paramagnetism, Ferromagnetism, Anti-ferromagnetism, Ferrimagnetism and Super-paramagnetism.
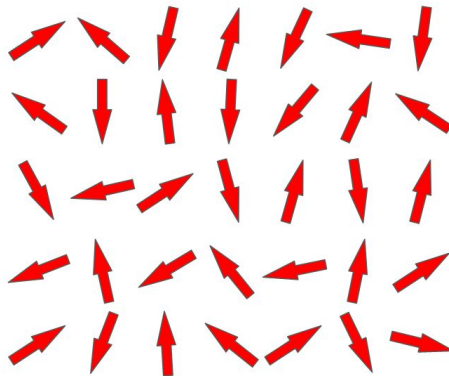
Figure 2.1: *Orientation of paramagnetic moments with zero external field.*

Paramagnetism arises from the unpaired electrons present within the system; thermal fluctuations dominate these electrons and so they will point in random directions, as shown in figure 2.1. An external field applied to this system will cause the spins to begin to align, as the external field overcomes the fluctuations the spins will align more and more. The magnetisation/applied field

relationship can be best described using the Brillouin function for an idealised paramagnet[31].

Ferromagnetism arises from the same process to that of paramagnetism with one extra factor, the tendency for the internal moments to align with each other without an external field, creating a spontaneous moment in zero field as shown in figure 2.2. This alignment can be attributed to several competing exchange interactions between atoms that are covered later in this chapter. Anisotropy arising from internal stresses and strains, crystalline structure and material shape then generates a preferred direction for the spins to align. The direct exchange and other exchanges are discussed further in section 2.5.

Areas of the material will all contain moments parallel to each other. However, not all given moments will align in a large system; they will form islands of common alignment known as domains. The existence of these domains reduces the internal magnetostatic energy, and are separated by thin domain walls where the orientation transitions from alignment with one domain to the other over just a few atoms. Domain walls can be moved, and domains aligned with one another using an external magnetic field.

As an external field is applied, it will eventually overcome the separate aligned domains, forcing all to eventually align with the field and become saturated. This change in the domain alignment is due to the balancing of several internal energies, to reduce the Landau-Lifshitz free energy. Where the Landau-Lifshitz is the linear combination of the exchange energy, magnetostatic energy, crystalline and shape anisotropy, and the Zeeman energy. When applying an external field, those domains closest to parallel with it will have a reduced Zeeman energy and a therefore reduced Landau-Lifshitz energy, but those unaligned will have an increased Zeeman energy. When the size of the Zeeman energy becomes significant enough the domains will realign to reduce the total Landau-Lifshitz energy. Due to the resistance to change from their current state, a form of history is present within

10

the material known as hysteresis. Due to microscopic or macroscopic shape, a preferred magnetic field angle can also be seen. Giving the material an "easy axis", where lower fields are required for saturation, and "hard axis" , where larger fields are required[31].
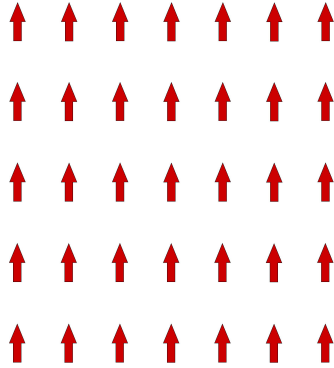
Figure 2.2: *Orientation of ferromagnetic moments with zero external field. The strength of the moment is proportional to the length of the arrow.*

The ferromagnetic magnetisation of a material is an ordered state, decreasing the entropy of the system. Thermal fluctuations within the material will do the opposite and increase the system entropy. For a system to be considered ferromagnetic its magnetic ordering effects must overcome its thermal fluctuations. At high enough temperatures, thermal fluctuations will overcome the magnetic ordering and the material will lose its ferromagnetism. This point is known as the Curie temperature and is a magnetic phase transition.

Ferrimagnetism has a similar moment ordering to that of ferromagnetism, but with a contingent of secondary atoms within the unit cell that have a magnetic moment opposing the mass alignment, see fig 2.3. These opposing alignments have a smaller net total moment, so at zero external fields, there is still a spontaneous magnetisation present. When an external field is applied, an anisotropy becomes present, whereby the field interacts and enhances mainly in one direction but to a smaller degree in the other[31].
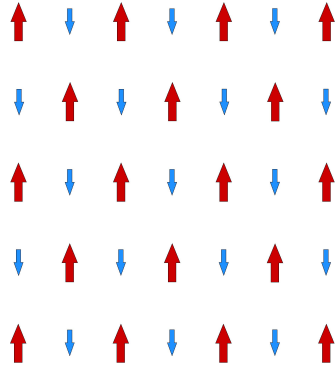
Figure 2.3: *Orientation of ferrimagnetic moments with zero external field. The strength of the moment is proportional to the length of the arrow.*

Anti-ferromagnetism also arises from a process of spins with a tendency to align but in opposing directions to their neighbours, as shown in figure 2.4 due to a negative exchange interaction with neighbouring atoms. With no external field, anti-ferromagnetic materials will have a vanishing magnetisation. As an external field is applied, the anti-ferromagnetic material will have a non-zero net magnetisation, whereby a group of moments in one orientation will begin to overcome their opposing neighbours in the other[31].
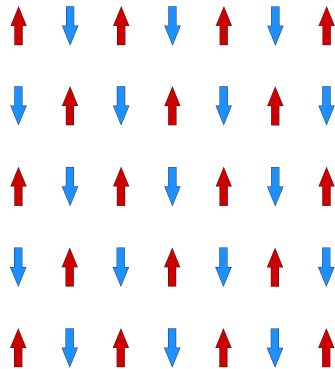
Figure 2.4: *Orientation of anti-ferromagnetic moments with zero external field. The strength of the moment is proportional to the length of the arrow.*

Similar to the Curie temperature described earlier, thermal fluctuations will overcome the opposing alignment and cause a level of randomness in the magnetic

ordering at sufficiently high temperatures. This phase change, specifically for anti-ferromagnets, is known as the Néel temperature.

Diamagnetism is most measurable in materials that present no other forms of magnetism due to its magnitude usually being much smaller. It is present in all materials, and its response is of an internal field that opposes an applied external field[31].

2.3   The Magnetocaloric Effect

The magnetocaloric effect is the temperature response that is found in magnetic materials when placed in and removed from a magnetic field. In the simplest of explanations, it appears as the magnetic field causes the domains and magnetic moments within the material to align. Thus reducing the entropy of the system, this in turn creates an increase in temperature of the system to maintain internal energy as an adiabatic process. The reverse is true when the system is removed from a magnetic field; it is this process that is being studied with the hope of further understanding and exploiting it.

The effect is defined by the relationship

$$\frac{\delta S}{\delta M} = \frac{\delta H}{\delta T} \tag{2.1}$$

where S is the entropy, M is the magnetisation, H is the external magnetic field and T is the system temperature. which leads to the expression

$$\Delta S(T, \Delta H) = \int_{H_i}^{H_f} \frac{\delta M(T, H)}{\delta T} \delta H \tag{2.2}$$

where H_i and H_f are initial and final applied magnetic fields. Taking into account the first and second laws of thermodynamics, an equation describing the entropy of the system and the change in heat capacity can be derived

$$\Delta S(T, H) = \int_{T_0}^{T} \frac{C(H_i)}{T} \delta T - \int_{T_0}^{T} \frac{C(H_f)}{T} \delta T \qquad (2.3)$$

Where C(H_i) and C(H_f) are the heat capacity at the two corresponding H fields in Figure 2.5, T is the temperature with T_0 being the initial temperature and S the entropy [32]. By substituting this equation into the one above, an expression for the adiabatic temperature change can be found

$$\Delta T_{ad}(T, \Delta H) = - \int_{H_i}^{H_f} \frac{T}{C_p(T, H)} \frac{\delta M(T, H)}{\delta T} \delta H \qquad (2.4)$$

As the C_p varies greatly with both temperature and field, it cannot be treated as a constant but the ΔT_{ad} can still be calculated if the value of C_p is known for a series of temperatures and fields between H_i and H_f.

This adiabatic temperature change allows for the full description of the magnetocaloric effect, in that it provides a full solution for the entropic and temperature change. A Plot of the relationship is shown in figure 2.5.

14
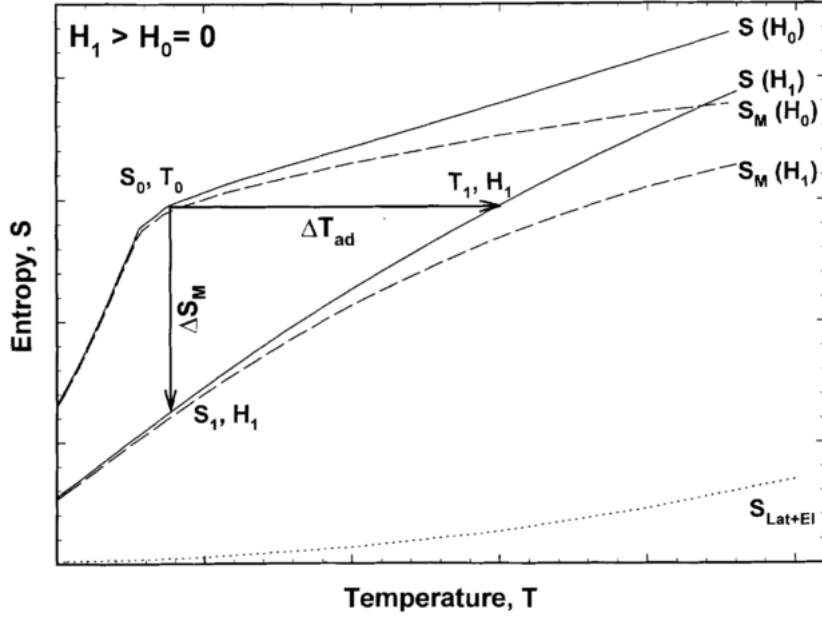
Figure 2.5: *Graph showing the effect a magnetic field has on magnetocaloric materials entropy versus temperature, where H_0 and H_1 represent two different applied fields, H_0 being 0T. Figure reproduced from Kobe et al[2]*

.

In Figure 2.5 the difference in the temperature/entropy relationship due to an external magnetic field is presented. It can be seen that the magnetic component of the entropy dominates over the lattice and electron components in this process with S representing their combined components of S_M and S_{Lat+El}.

For the purpose of an indirect measurement, such as the one that will be conducted using a SQUID magnetometer, the entropy change will have to be calculated, this is further described in section 4.5. The adiabatic magnetisation along S_0, T_0 to S_1, T_0, and the adiabatic temperature change along S_1, T_0 to S_1, T_1 can be characterised as below

$$\Delta S = S_1 - S_0 \tag{2.5}$$

at the entropy change step, where $\Delta T \approx 0$ and

15

$$\Delta T = T_1 - T_0 \tag{2.6}$$

at the entropy change step, where $\Delta S \approx 0$.

Magnetocaloric refrigerators are estimated to be capable of reaching 60% efficiency when compared to the ideal (Carnot) cycle [4], while their compressed gas counterparts are capable of just 40%. This efficiency has driven a community of magnetic refrigeration prototypers to produce an array of viable models, The first appeared in 1975 by Brown [16], but several competing models have emerged since [33, 34, 35, 36]. Both magnetocalorics and compressed gas refrigerators will use a refrigerant medium to absorb and move heat away at the correct point in the cycle and to move it away from the point needing to be cooled. Although the work proposed for this PhD is not to create prototype refrigerators, the above-cited papers act as proof of the viability of the technology and the need for further understanding.

2.4   First Order Phase Transition Materials

A first-order phase transition (FOPT) within a magnetocaloric material can lead to an enhanced effect; known as the giant magnetocaloric effect (GMCE).

It occurs as a result of both the entropy change and the thermal hysteresis that is present due to the crystal structure change in conjunction with the change in temperature, or the large volume change and magnetoelastic coupling experienced during magnetisation. As the system will have a latent heat associated with the phase change, a large change in energy is created. This, combined with the already existent heat from the entropy change will create a much more significant, temperature change. Lyubina et al. lay out a method for 'resetting' the material that allows for the measurement of the material entropy change alone by heating well above or well below the transition temperature between each temperature

point measured [32].

These transitions within the material will occur within a very narrow regime of temperatures. One of the main objectives of modern magnetocaloric research is to move this temperature range to within that of room temperature or a desired operating temperature. Broadening the range over which these transitions can occur is also of interest [37, 4]. Changing the structure will damage the material, causing cracks and fissures to appear. Reducing this stress on the material will help its introduction commercially.

Materials that experience a magnetic order and crystallographic symmetry alteration when in a changing magnetic field and temperature are known as magnetic-martensitic materials. If the change is discontinuous, as is in first order transitions, their characteristics close to the transition can best be described using the Clausius-Clapeyron equation [26]

$$\frac{dP}{dT} = \frac{\Delta s}{\Delta v} = \frac{L}{T\Delta v} \tag{2.7}$$

Where P is the system pressure, T is the temperature, Δs is the change in entropy, Δv is the change in volume, and L is the specific latent heat.

Equation 2.7 better describes FOPT transitions than 2.1 as it includes consideration for the volume change, but with the correct measurement protocol equation 2.1 can be used.

Since the discovery of the GMCE, many have used the simple relation described in equation 2.1 to report on the change in entropy, however, as the very nature of first-order is discontinuous this cannot strictly describe its behaviour and has led many to misreport an enlarged entropy change response [38]. A process of 'resetting' suggested by Lyubina et al. eradicates this problem, by reaching a stable state between measurement points by heating well above or cooling well below the critical point [32].

Mean field theory can be applied to further understand a phase transition, as

demonstrated in 1962 by Bean et al. [39] who published the following equation
for the systems Gibbs free energy

$$G_v = -HM_s\sigma cos(\frac{\phi}{2}) - \frac{Nk_bT_c\sigma^2 cos\phi}{2} + \frac{[(\nu - \nu_0)/\nu_0]^2}{2k_b}$$
$$- T(S_{spin} + S_{lattice}) + P(\nu - \nu_o)/\nu_o$$

(2.8)

Where H is the applied magnetic field, M_s is the magnetic saturation, σ
the relative magnetisation, ϕ the angle between sub-lattice magnetisations (0 for
ferromagnetic, π for anti-ferromagnetic), ν is the volume, ν_0 the volume where
there no exchange interaction, N the number of particles per unit volume of ν_0, T
the temperature and P the pressure. While assuming a spin half system system,
neglecting the lattice parameter and substituting in $T_c = T_0[1 + \beta(\nu - \nu_0)/\nu_0]$,
from section 2.6.6. where β is the slope of dependence of T_c on volume, it can be
reduced to the equation

$$\frac{T}{T_0} = (\frac{\sigma}{tanh^-1\sigma})(1 + \frac{\eta\sigma^2}{3} - PK\beta)$$

(2.9)

Where $\eta = \frac{3}{2}Nk_bKT_o\beta$, and K is the compressibility.

It is shown that for values of $\eta < 1$, the material will undergo a second-order
transition and for values of $\eta > 1$ the material will undergo a first-order transition,
meaning the phase transition is directly affected by the size, volume and strain
of the material through the compressibility factor K. This allows for thin-film
investigations to look into its dependency on shape and strain, and ultimately to
exploit these relationships.

2.5 Magnetic Coupling

The long-range magnetic ordering described in section 2.2 arises from microscopic
interactions between many ions. The complete magnetic description of a system
is usually formed from a combination of interactions between electrons, nuclear

interactions and external fields. These small scale interactions collectively form large scale alignments that lead to macroscale magnetism [31].

2.5.1 Direct Exchange Interaction

The direct exchange interaction describes the interaction between two identical particles. For localised, unpaired electrons this effect appears as a short-range interaction and directly depends upon the overlap of the unpaired electrons between neighbouring atoms in a lattice. The orthogonality of the orbitals affects the sign of the exchange, with orthogonal overlap forming a positive exchange, favouring a ferromagnetic interaction [31].

2.5.2 Dipole-Dipole

The dipole dipole interaction describes the direct interaction of 2 magnetic dipoles on the microscopic scale. Considered a weak interaction above $1\ K$ it does not contribute greatly to the long range ordering seen at higher temperatures. The dipole-dipole interaction can be described as

$$H = \frac{-\mu_0}{4\pi\mathbf{r}^3}(3(\mathbf{m} \cdot \mathbf{r})\mathbf{r} - \mathbf{m}) + \frac{2\mu_0}{3}\mathbf{m}\delta^3(\mathbf{r}) \tag{2.10}$$

Where μ_0 is the permeability of free space, $\mathbf{r}$ is the vector from the dipole to the point being calculated and $\mathbf{m}$ is the magnetic moment of the dipole.

Despite the weakness of the dipole-dipole interaction, it does affect material ordering at extremely low temperatures; it also contributes to the sum of magnetic interactions [31].

2.5.3 Super-Exchange

The super-exchange interaction is the interaction between magnetic ions mediated by a third non-magnetic particle. It is a strong, usually anti-ferromagnetic

interaction, but can appear as a ferromagnetic interaction given the mediating atom is connected to the donor sites at 90 degrees.

First proposed in 1934 by Hendrik Kramers to describe the interaction between Mn sites in MnO, it was further expanded upon by Goodenough, Kanamori and Anderson (GKA). The GKA rules allow for the prediction of spin alignment with the next nearest neighbour separated ions [40].

It is caused by a virtual hopping of ions between the two magnetic sites via the degenerated and occupancy of the third mediating non-magnetic site. The third site has an overlap with the magnetic ions, so anti-alignment with each of the neighbouring sites leads to an interaction between the magnetic sites ions.

2.5.4 Double-Exchange

Similar to the super exchange, the double exchange involves the transfer of an electron between two magnetic sites. Unlike super-exchange, the two magnetic sites will have different valence states and maintain their spin orientation, making it a ferromagnetic interaction. It was first described by Clarence Zener in 1951 [41].

2.5.5 RKKY

The Ruderman Kittel Kasuya Yosida (RKKY) exchange model is a similar mechanism to the super-exchange in that it has a third mediating body between the magnetic ions. For the RKKY model, the mediating body is the conduction electrons. For this reason, the model has more applicability and impact within metals, whereas the super-exchange tends to dominate within insulators.

The interaction can be explained simply as a localised spin polarising the conduction electrons, the then polarised electrons couple to another localised spin. It is thereby indirectly coupling the first spin and last spin. The RKKY coupling applies to both unpaired localised electrons and the magnetic nuclear

atomic cores in the lattice. For Rare Earth (RE) materials, the xenon like core shell of the small orbital electrons screens most of the interaction for the nucleus. The 4f electrons are also shielded by the 5s and 5p electrons, resulting in a weak direct exchange and a dominant indirect interaction mediated by the conduction electrons for rare earth materials [42].

The interaction can be described by the coupling RKKY $J(R_{ij})$ as

$$J(R_{ij}) = 9\pi(\frac{j^2}{E_f})[\frac{2k_f R_{ij} cos(2k_f R_{ij}) - sin(2k_f R_{ij})}{2k_f R_{ij}^4}] \tag{2.11}$$

Where j is an ion-conductive electron coupling coefficient, E_f is the Fermi energy, k_f is the Fermi wave-vector and R_{ij} is the distance between the two ion sites.

Equation 2.11 contains sine functions of the ionic distance R_{ij}, this results in a sinusoidal dependence of the sign of the interaction with distance. The R^4 factor also means the magnitude of the interaction tappers off at longer distances. Despite this, the RKKY interaction is usually of a more extended range than those previously described.

2.6 Magnetic Phase Transition Models

The broken symmetry of a phase transition can be described by a systems microscopic properties, with many microscopic entities forming a canonical macroscopic change. To further understand the interplay of symmetry breaking and the magnetocaloric effect, many phase transition models have been suggested. Some of these models are discussed in this section.

2.6.1 Landau Theory

The Landau theory is a mean-field model of ferromagnetic to paramagnetic transitions; the model best describes the system close to the T_c. It consists of writing

the systems free energy, while in a ferromagnetic state, as a power series that only contains the even powers to maintain global symmetry. This free energy can be written as

$$F(M) = F_0 + a(T)M^2 + bM^4 + ... \tag{2.12}$$

Where $F(M)$ is the free energy, M is the magnetisation, F_0 is a constant, b is a positive constant and $a(T)$ is a temperature dependent coefficient.
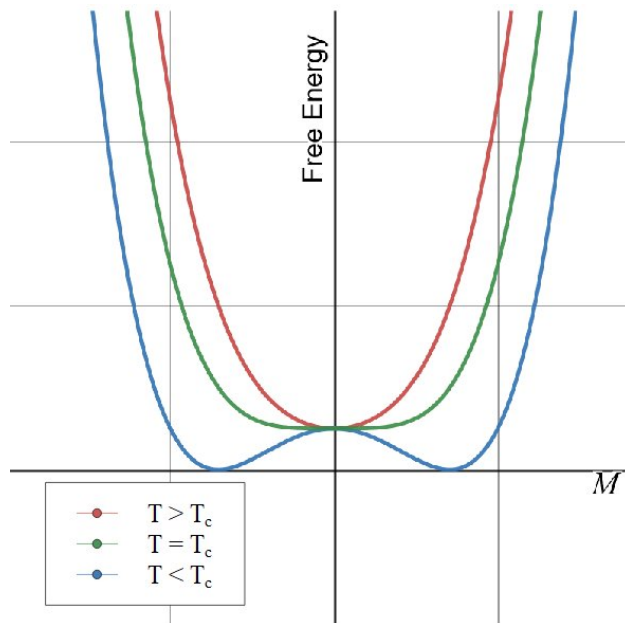
Figure 2.6: *Free Energy at three separate temperatures, above, at and below T_c.*

Higher orders are required for itinerant systems. By minimising, it can be shown that there are two possible solutions to M, either

$$M = 0 \quad or \quad M = \pm(\frac{a_0(T_c - T)}{2b})^{1/2} \tag{2.13}$$

Where a_0 is a positive constant.

Given both of these solutions, the ferromagnetic and paramagnetic phases can both be described. This model does fail to describe the critical point; however,

where $T = T_c$. The model can describe a SOPT system but must be expanded up to the sixth even order to describe a FOPT correctly [43]. The Landau theory approach also does not take into account volume or pressure changes.

2.6.2 N-Dimensional Models

To further understand the MCE simplified cellular automata models of magnetism are used, these work by providing a set of rules for an individual site based upon its neighbours in a lattice. The model provides no rules for the macro-structure and allows the model to run iteratively, producing global phenomena from just near neighbour interactions.

N-dimensional models are a subgroup of cellular automata studied within the statistical physics community. Their applicability to a variety of real world phenomena is described in section 3.6. They rely upon a random number generation, discussed below, and a set of lattice parameters and rules. Some well studied models, Ising, Potts and Heisenberg are further described below.

2.6.3 Monte-Carlo Method

The Monte-Carlo method is a method to estimate analytical solutions using a stochastic approach, usually employed for problems where the analytical solution is proven difficult or impossible. The application in statistical physics allows for the probing of complex phase space in a given system. The majority of Monte Carlo studies into the phase space of a system will use one of 2 methods; the Wang-Landau method, or the Metropolis-Hastings method. A brief overview of the former will be given, with a more in-depth discussion of the latter [44].

2.6.4 Wang-Landau Method

The Wang-Landau method is a temperature-independent method to calculate the density of states of a system. Once the density of states is calculated, all other thermodynamic variables can be found.

The method relies upon random walks in energy space, at each energy site a comparison is made to a function of the inverse of the density of states. Once this comparison is made the probability of revisiting that site is modified by a chosen modification factor. Usually, this modification factor will make revisiting sites less and less likely, thereby increasing the likelihood of visiting more complex energy states. By recording the number of visits to each energy state, a density of states for the system can be estimated.

As the length of the random walk increases the model will produce a density of states that approaches the real density of states of the given system.

2.6.5 Metropolis-Hastings Method

The Metropolis-Hastings method is used to minimise the energy of the system by randomly flipping spin sites in a fixed lattice and comparing the new to the old system [44].

Because of the detailed balance assumption, where at equilibrium in the system a Markov process is equal to its reverse process, the probability of the state S_1 becoming S_2 is equal to state S_2 becoming S_1 during each iteration of the algorithm. Comparing this to the canonical ensemble gives a likely hood of transition P_{1-2} from S_1 to S_2 as

$$P_{1-2} = P_{2-1}e^{-\Delta E/k_b T} \tag{2.14}$$

Where P_{2-1} is the transition from S_2 to S_1, ΔE is the difference in energy of S_1 to S_2, k_b is the Boltzmann constant and T is the temperature of the system.

By choosing an appropriate value for P_{1-2}, the probability of accepting a given flip can be calculated. In 1953 Metropolis et al. [45] proposed the now widely used condition

$$P_{1-2} = \begin{cases} e^{-\Delta E/k_b T} & where \Delta E > 0 \\ 1 & where \Delta E \leqslant 0 \end{cases} \quad (2.15)$$

Under these conditions, an energy difference ΔE of zero or less is guaranteed to cause a transition to the new spin state S_2. However, if ΔE is greater than zero, there is still a probability of transition proportional to Boltzmann distribution.

By using this algorithm to calculate a new state's energy and to decide to switch, a prediction for the lowest stable energy state can be made. The process of retaining the favourable state over multiple iterations is known as a Markov chain and should theoretically lead to the energy minima. There are however some pitfalls with this method that must be considered when implementing, firstly, an energy well that does not truly represent the lowest state, but merely an energy state too deep to escape can lead to erroneous results. Secondly, if there exists a degenerate low energy state, a single run will only predict one at random. To overcome both of these large iteration chains with multiple runs should be used.

Ising Model

Ising, Potts and Heisenberg models can all be thought of as specific cases of the n-dimensional model. Their main difference being the degrees of freedom the spins are allowed to exist in, with Ising being n=1, Potts being n=2 and Heisenberg being n=3. The Ising model is a simple approximation of a magnetic system that allows for a phase transition under the right scenarios. The approximation assumes the system is entirely made up of a lattice of spins S with a binary set of values with a coupling constant J between neighbours. The model is analogous to a magnetic system with a finite number of possible spin directions.

Ising, Potts and Heisenberg models can all be written in 1, 2, 3 or more dimensions, with differing interactions in each dimension, shown in figure 2.7.
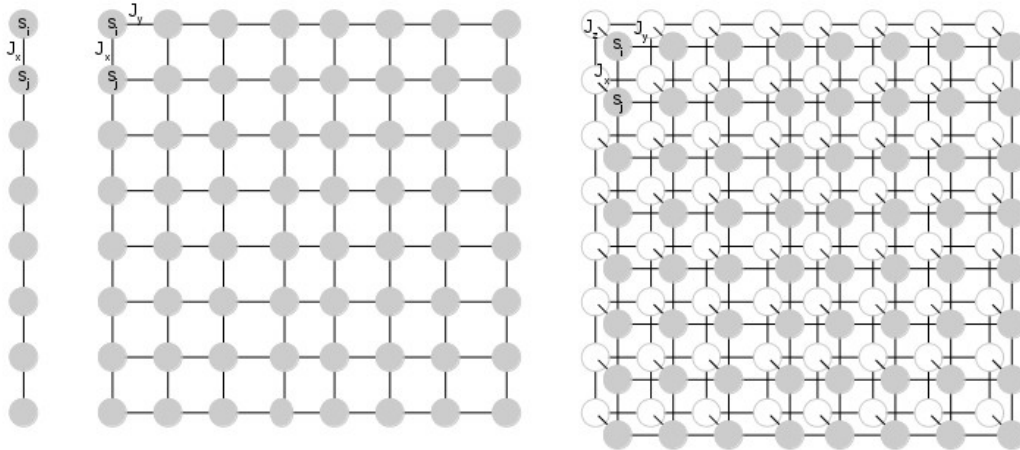
Figure 2.7: *From left to right shows the basic Ising lattice for 1, 2 and 3 dimensions, with each site having a spin S value and J being separated into x, y and z components to indicate possible differing interactions.*

The basic Ising models all follow the same principle, a Monte-Carlo Metropolis method is used to randomly select and test a sites likelihood to flip based on the energy of the site and compared to the temperature of the system. The first term represents the interaction of the ith site with all other neighbouring sites through a ferromagnetic exchange coupling and the second term, a Zeeman effect, due to external fields as described by the Hamiltonian

$$\mathcal{H} = -J \sum_{i,j,} S_i S_j - H \sum_i S_i \tag{2.16}$$

Where $\mathcal{H}$ is the Hamiltonian, J is the magnetic coupling constant with components $(J_1, \; ... \; J_n)$ for n dimensions, S is the spin at a single site, and H is the applied external field.

This model allows for the internal interaction from the neighbouring sites as well as the external interaction from the field applied to be taken into account.

This will also allow for a direct comparison with experimental data from SQUID and VSM as described in section 4.5 and 4.6 respectively. The average magnetisation can be taken using the equation

$$M = \frac{1}{N} \sum_i S_i \qquad (2.17)$$

Where M is the magnetisation and N is the total number of spin sites.

The model was famously proposed by and solved in 1 dimension by Ising for his PhD thesis in 1924. The two-dimensional model was later solved by Onsanger in 1944 with the expression for magnetisation being solved exactly as

$$M = (1 - [\sinh 2\beta J_1 \sinh 2\beta J_2]^2)^{\frac{1}{8}} \qquad (2.18)$$

Where J_1 and J_2 are the horizontal and vertical coupling interaction energies and $\beta = \frac{1}{k_b T}$, K_b being the Boltzmann constant and T the temperature of the system.

There has not been reported an exact solution to the problem in 3 or higher dimensions; this has lead to several approaches that take advantage of modern computers to simulate an approximate answer, including cluster-variation, effective field theory, mean-field theory and the Monte Carlo metropolis technique. Models discussed from here onwards will use the Monte Carlo metropolis method with only nearest neighbour interactions being considered for equation 2.16 and all subsequent Hamiltonian first terms. The magnetisation and energy data produced by each simulation can be used to find an entropy change and temperature change associated with the phase transition.

There have been several papers comparing the Ising model to MCE materials [46, 47, 48] due to the rise in interest of the GMCE and the presence of a phase transition in both the model and the materials. The ability to measure the magnetic moment and specific heat of both allows for direct comparison and could drive the experimental research to better tune the selected materials based

on model parameters that can be calculated.

Typical Ising models do not account for defects within the structure, however introducing rules for specific sites that are chosen or randomly distributed can induce defect like behaviour.

Potts Model

The Ising model can be thought of as a simplification of the Potts model in which the spins have a degree of freedom reduced. As such, the Potts model allows the spin to have a value outside of the normal +/-1 restriction of the Ising model. Where the spin S can be described as

$$S = \{1, ...q\} \ , \ q = \{2, ... \inf\} \tag{2.19}$$

and the Hamiltonian dimensions instead becomes

$$\mathcal{H} = -J \sum_{i,j} \delta_{S_i S_j} - H \sum_i S_i \tag{2.20}$$

Where q can take any value from 2 to infinity and δ is the true form of the Dirac delta function. This difference allows the spins to take a number of directions in a circle depending on the choice of q.

The advantage of the Potts model over the Ising model is that it can simulate a FOPT similar to those described in chapter 1 through mean-field approximations [49], whereas the Ising model can only show FOPT after being heavily modified. Neither the un-modified Ising or Potts models are capable of modelling a distortion in the lattice at transition however [50].

Heisenberg Model

Just as the Ising model can be thought of as a simplification of the Potts, the Potts model can also be thought of as a simplification of the Heisenberg model.

Given the only restraints usually employed is to limit the interaction to only consider nearest neighbour interactions.

In the Heisenberg model, each site has an associated spin $\boldsymbol{S_i}$ that interacts with its nearest neighbour sites. The mediating coupling J_{ij} is also a vector quantity. The added complexity of this model means there is no analytical solution, given the higher degrees of freedom the spin site is given. The Hamiltonian is given as

$$\mathcal{H} = -\frac{1}{2}\sum_{i,j} J_{ij}\boldsymbol{S_i}\boldsymbol{S_j} - H\sum_i S_i^z \tag{2.21}$$

Where S_i^z is the z component of the spin, parallel to an external applied field H.

Hubbard Model

The Hubbard model describes the non-localised to localised electron transition, or the conductive to insulator transition on the macroscale and is based on the tight binding model. The Hubbard Hamiltonian consists of 2 components, the first is the kinetic energy described by the tight binding model, arising from electron hopping between sites. The second is an opposing Coulomb force between two electrons sharing an orbital. The Hamiltonian is given as

$$H_{Hubbard} = -t\sum_{i,j,\sigma}(c_{i\sigma}^\dagger c_{j\sigma} + c_{j\sigma}^\dagger c_{i\sigma}) + U\sum_i n_{ij\uparrow}n_{ij\downarrow} \tag{2.22}$$

Where t is the hopping integral, $c_{i\sigma}^\dagger c_{j\sigma}$ are the creation and annihilation operators, U is the Hubbard term representing coulomb repulsion and $n_{ij\uparrow}n_{ij\downarrow}$ are the density operators of spin states.

The ratio of the first and second term t/U allows for the description of an insulator, conductor and the transition between them. With a dominant t model leading towards a highly conductive system and a U dominant model leading towards an insulating system. In the $U \rightarrow 0$ system the model returns to the

tight-binding model description.

2.6.6 Bean-Rodbell Model

The Bean-Rodbell model is a macroscopic phenomenological model that is an expansion of the Weiss molecular mean-field model. The model ignores the complexities of magneto-elastic interactions in favour of comparing the volume change across a FOPT. This allows the model to simulate distortion in the lattice across a transition, which other fixed lattice systems cannot. It does, however, neglect the effects the changing volume has on the interactions between lattice sites [39].

Despite this simplification, the model can accurately predict a T_c by assuming the dominant factor in determining a T_c is the volume/inter-atomic spacing change. The volume T_c relationship is given as

$$T_c = T_0(1 + \beta(\frac{\nu - \nu_0}{\nu_0}))$$ (2.23)

Where T_0 is the Curie temperature calculated for the same lattice but incompressible, ν_0 is the initial volume of the system, ν is the volume after volume change, and β is a coefficient dependant upon the temperature/volume relationship.

Introducing this T_c prediction into the Gibbs free energy equation 2.8 and assuming a ferromagnetic to paramagnetic transition ($\phi = 0$) gives

$$G_v = -HM_s\sigma - \frac{1}{2}Nk_b(T_0(1 + \beta(\frac{\nu - \nu_0}{\nu_0})))\sigma^2$$
$$+ \frac{[(\nu - \nu_0)/\nu_0]^2}{2k_b} - T(S_{spin} + S_{lattice}) + P(\nu - \nu_o)/\nu_o$$ (2.24)

Where H is the external magnetic field, M_s is is the magnetic saturation, σ the relative magnetisation, N the number of particles per unit volume of $_0$, P the pressure and $S_{spin} + S_{lattice}$ the entropy contribution from the spin states and lattice.

2.6.7 Partition Function

A partition function is used to understand many of the statistical models discussed above. It is a useful function that can be used to describe many of the thermodynamic variables needed to study the MCE including the free energy, entropy and magnetisation of the system when in equilibrium. The classical definition can be given as

$$Z = \sum_i e^{-\beta E_i} \qquad (2.25)$$

Where Z is the partition function, $\beta = \frac{1}{k_B T}$ and E_i is the energy of the system. The magnetisation can be described using the partition function as

$$< M > = \sum_i M_i e^{-E_i/Z} \qquad (2.26)$$

Where $< M >$ is the average magnetisation of the system per site and M_i is the Magnetisation of each individual site.

An important variable to consider when using a partition function is the equivalency, p. This represents the likelihood of the system having an energy E and is given as

$$p = \frac{e^E}{Z} \qquad (2.27)$$

Using the equivalency, the entropy of the system can be calculated using

$$S = pln(p) \qquad (2.28)$$

Where S is the entropy of the system at a given state.

Finally, from the Entropy calculation a free energy can be given as

$$F = E - TS \qquad (2.29)$$

Where F is the Helmholtz free energy and T the temperature of the system at a given state.

Literature Review

3.1 $Gd_5(Si_xGe_{1-x})_4$

3.1.1 Discovery

Gd is the only known pure element with an MCE near room temperature, with a $T_c \sim 293~K$. Being one of the most commonly studied MC materials, it is now widely treated as a benchmark for future research and comparison. Being a strong magnetocaloric material in itself, Gd has received a massive amount of research and is used to produce working prototypes. Pure Gd has been shown to have an adiabatic temperature change as high as, $\Delta T_{ad} = 5.9$ K, and an entropy change $\Delta S = 5~Jkg^{-1}K^{-1}$ in a 0 to 2 T field. The Gd MCE is a lambda like

SOPT transition. However, the high price of pure Gd means it is unlikely to enter the mass market, therefore looking for cheaper alloys of Gd without affecting the scale of the MCE has increased in interest. With doping from other rare earth materials (Tm, Er, Ho, Dy, Tb) or Mn, Gds' T_c can be manipulated to lower temperatures without much change in the scale of the MCE.

Even though the MCE effect has been known for over a century, the new drive for further room temperature research began when Pecharsky et al. [3] reported an entropy change more than two times greater than ever reported before close to room temperature. This entropy change increase was known as the Giant MagnetoCaloric Effect (GMCE) and drove the study of the MCE close to phase transitions.
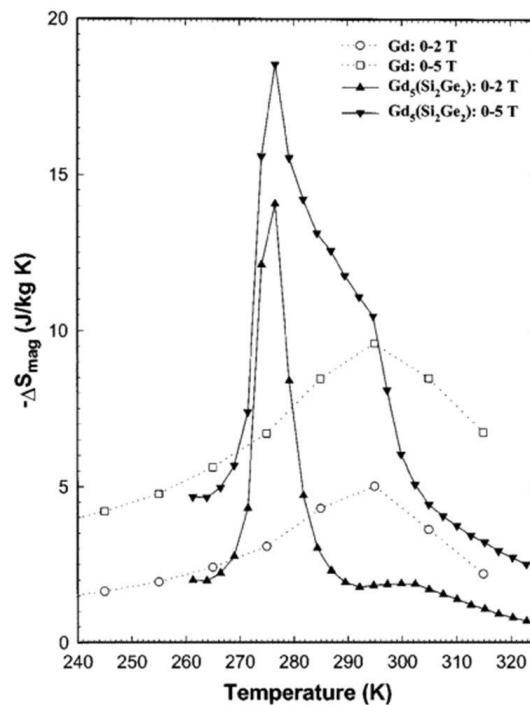
Figure 3.1: *The change in entropy for both gadolinium (often used as a reference material as it was the largest reported before this discovery) and GdSiGe at two varying fields. Figure reproduced from Pecharsky et al. [3].*

Forming more complex alloys, with a focus on introducing Si or Ge has produced a much more extensive temperature range over which the T_c is controllable. With GdScGe and GdScSi compounds having Curie temperatures of 252 K and 348 K respectively [51, 52, 37, 17, 4]. However, $Gd_5(Si_xGe_{1-x})_4$ is the Gd alloy that has produced the most interest within the Gd based MC community. Thanks to its full, tunable T_c from 125 K to 310 K it operates well within the desired range for refrigeration. The FOPT also means the MCE is far more significant in terms of ΔT_{ad} and ΔS than its pure Gd counterpart, see figure 3.1.

GdSiGe (Gadolinium Silicon Germanium) is a material that experiences a first-order phase transition with a large tunable range from 125 K to 310 K when in the form

$$Gd_5(Si_xGe_{1-x})_4$$
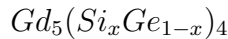
a value of x = 0.2 and x = 0.5 will create a transition at 125 K and 310 K respectively with a linear relationship between.

When above its transition temperature, between these points, the material will be in a paramagnetic state with a monoclinic crystal structure. When below the transition temperature, the material will be in a ferromagnetic state with an orthorhombic crystal structure. The transition is the period in which the material is shifting from one to another and as a FOPT the transition is sudden. This shifting does, however, create a thermal hysteresis within the material as there is a latent heat associated with the phase transition.

$Gd_5Si_2Ge_2$ has a coupled magnetic and structural transition which gives it a much larger response when compared to Gd, which undergoes a second-order magnetic transition. The only previous material known to exhibit the GMCE was FeRh at the time, but it had a far more substantial thermal hysteresis and a Curie temperature at an unfavourable value for commercial applications.
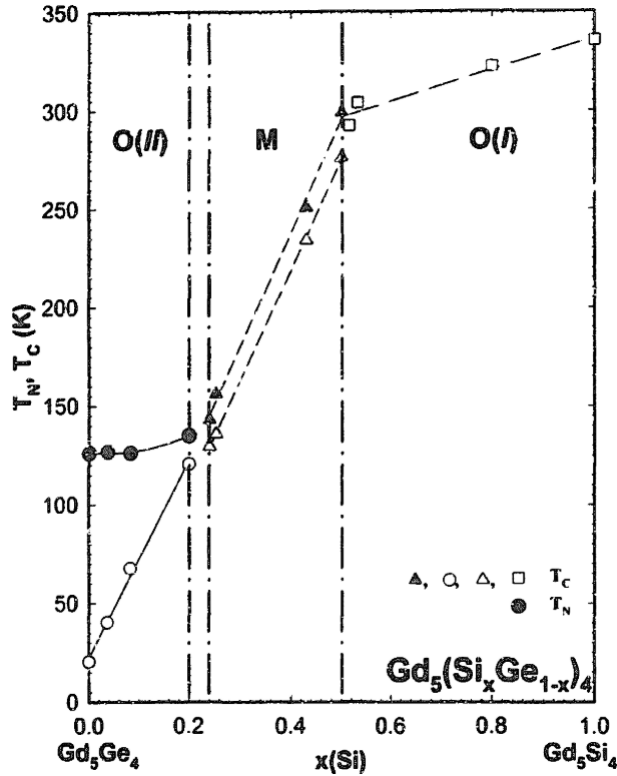
Figure 3.2: *phase diagram of $Gd_5(Si_xGe_{1-x})_4$ at zero magnetic field. Dashed and solid lines indicate magnetic phase boundaries and dot-dashed lines indicate crystallographic phase boundaries. Figure reproduced from Pecharsky et al. [3].*

The crystallographic data presented in table 3.1 from Mozharivskyj et al. [9], data for the orthorhombic phase of $Gd_5Si_2Ge_2$ is taken as the dominant phase below 300 C.

Due to the materials tendency to form inhomogeneous $Gd_5Ge_3, Gd_5Ge_4, Gd_5Si_3$ and Gd_5Si_4 phases after creation, it has been found that high-temperature annealing helps to homogenise the material. Annealing will increase the available magnetocaloric material and magnetocaloric response. This is due to the high temperature allowing the Si and Ge atoms to reorganise and reorder within the material and remove the predominantly orthorhombic Gd_5Si_4 -like phases that exist when at high temperature [53].

36

Table 3.1: *Crystallographic data for $Gd_5Si_2Ge_2$ and Gd_5Si_4, reproduced from Pecharsky [3]*

T,°C	space group	str. type	a,Å	b,Å	c,Å	γ,°
200	$P112_1/a^a$+Pmna	$Gd_5Si_2Ge_2{}^a$+Gd_5Si_4	7.597(1)	14.853(3)	7.797(2)	93.09(1)
300	$P112_1/a$	$Gd_5Si_2Ge_2$	7.613(2)	14.868(3)	7.819(2)	92.83(2)
310	$Pmna^a$+$P112_1/a$	$Gd_5Si_4{}^a$+$Gd_5Si_2Ge_2$	7.5420(8)	14.845(2)	7.825(2)	90
320	$Pmna^a$+$P112_1/a$	$Gd_5Si_4{}^a$+$Gd_5Si_2Ge_2$	7.5427(9)	14.852(2)	7.830(2)	90
330	$Pmna$	Gd_5Si_4	7.5444(8)	14.851(2)	7.830(2)	90

3.1.2   Doping $Gd_5(Si_xGe_{1-x})_4$

A significant amount of work has gone into reducing the latent heat within other research groups [4], mainly via doping with other materials. There are some promising candidates when substituting Ge sites with Cu, Ga, Mn and Fe which all reduce the hysteresis by a significant amount[54, 55]. Fe reduces hysteresis to close to zero, with the most significant decrease being

$$Gd_5Ge_{1.75}Si_2Fe_{0.25}$$
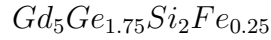
The four doping materials mentioned above have little to no effect on the phase transition, however while attempting to dope in other materials the phase change tends to disappear.

To bring $Gd_5(Si_{1-x}Ge_x)_4$ to real-world applications reducing magnetic and thermal hysteresis is required, and increasing the ΔS is also an objective to increase its likelihood of uptake. Co, Cu, Ga, Mn, Al, Bi, Sn and Fe [54, 56] all decrease the magnetic hysteresis, with Fe substitution of Si or Ge reducing the hysteresis to almost none. Unfortunately the doping leads to other phases forming, reducing the overall MCE. There have been attempts to replace the Gd constituents with other RE materials. Most reduce the MCE and lead to a large

shift in T_c or a change in the type of the transition to a SOPT [4].

3.1.3 $Gd_5(Si_xGe_{1-x})_4$ **Structure**
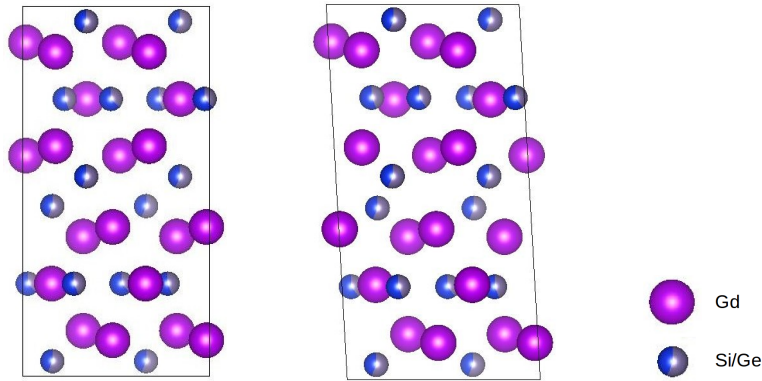
Figure 3.3: $Gd_5(Si_xGe_{1-x})_4$ *in its two main phases close to room temperature.*
(Left) Low temperature orthorhombic phase, (Right) High temperature monoclinic
phase. The Si/Ge atoms are presented as a fraction of their preferred occupancy
of the given site.

The large FOPT is due to the magnetostructural transition in $Gd_5(Si_xGe_{1-x})_4$
for $0.24 \leqslant x < 0.5$ from a orthorhombic (space group Pnma) ferromagnetic phase
to a monoclinic (space group $P112_1/a$) paramagnetic phase, figure 3.3, in which
there is a shearing of the planes and breaking of the Si/Ge-Si/Ge bonds leading
to the latent heat in the system. For values of $x < 0.24$ the compound takes
an orthorhombic Gd_5Ge_4 like structure that experiences a SOPT at much lower
temperatures. There exists a small regime at much lower x that can be in a low-
temperature ferromagnetic phase, a higher temperature anti-ferromagnetic phase
and a high-temperature paramagnetic phase. For values of $x > 0.5$ the compound
takes an orthorhombic Gd_5Si_4 like structure that experiences a SOPT at higher
temperatures.

3.2 $La_1(Fe_xSi_{1-x})_{13}$

3.2.1 Discovery

Another material of interest is LaFeSi due to it also having a first-order phase transition close to room temperature. Being far cheaper to produce than GdSiGe, LaFeSi has found widespread use within the research community [18]. LaFeSi based material represents one of the forefronts of room temperature magnetocalorics due to their large entropy change and relatively low price compared to the more extensively studied Gd based materials. The desired ferromagnetic, face-centred cubic $NaZn_13$-type phase ($Fm\bar{3}c$) is known to be unstable in its simplest form ($LaFe_{13}$), but substituting Fe sites with either Si, Al or Co can allow the material to become stable, figure 3.4. Hu et al. [57] reported a $\Delta S \simeq 20~Jkg^{-1}K^{-1}$ at 210 K, for a field change of 5 T. Describing this as a FOPT due to an itinerant electron metamagnetic transition, during which the crystal symmetry does not change, but through the isotropic magneto-volume change there is a decrease in volume of $\simeq 1\%$. Hu et al. also showed a SOPT transition when there is a significantly higher quantity of Si. Company et al. also found that for values of $x \leqslant 2.5$ in $LaFe_{13-x}Si_x$ the desired $NaZn_13$ phase is formed, but for values of $x > 2.5$ an alternative tetragonal structure forms [58].

There is a transition from FOPT to SOPT within the cubic $La_1(Fe_xSi_{1-x})_{13}$, as low Si content is a FOPT type transition that gradually changes to a SOPT as Si concentration increases. This increasing Si reduces the materials maximum ΔS but also decreases the hysteresis of the material. The phase transition is intrinsically linked to the Si concentration, or the Fe/Si ratio. The higher Si concentration that leads to a SOPT leaning transition also increases the T_c. To more effectively increase the T_c without decreasing ΔS introducing either Co or H can work [4]. Co introduced as a substitution is effective at increasing the materials T_c above room temperature while maintaining stability but will increase

heat capacity. Hydrogen doping is shown not to change the heat capacity but does become unstable at higher temperatures [59].

De Oliviera et al. [60] showed that generally magnetocalorics could be described by one of two systems, one where the electrons can assume to be localised like GdSiGe and described by a Heisenberg-like Hamiltonian wave. And a second, like LaFeSi systems which entail an itinerant electron system and is best represented by using band theory to form a Hamiltonian of the system. The fact that LaFeSi has the second system is why it has a much smaller thermal hysteresis when compared to GdSiGe, where the itinerant electron system has a double well free energy structure with a small barrier separating the FM and PM states, creating a small thermal hysteresis with a crystal volume change of $< 1\%$.

Al stabilised $NaZn_{13}$ like $LaFeAl$ materials have received less study due to their reduced ΔS compared to Si stabilised. However, they display an exciting phase relationship with the Fe/Al ratio and with Co doping [61]. Doping Al into LaFeSi also causes a reduction in the entropy change when compared to undoped LaFeSi but is also actively researched [62].
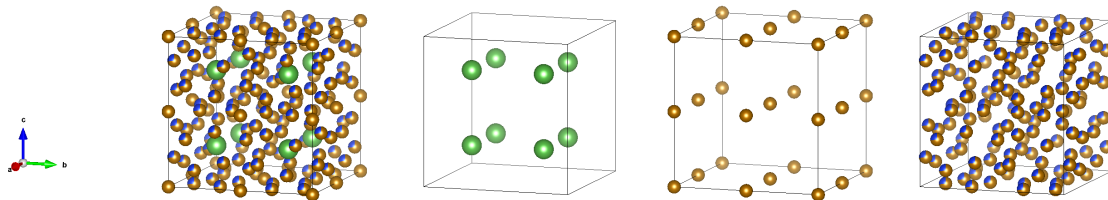
Figure 3.4: *From left to right, LaFeSi $NaZn_{13}$-type structure, La at 8a sites, Fe at 8b sites and the remaining 96i sites that have a random distribution of Si and Fe.*

3.2.2 $La_1(Fe_xSi_{1-x})_{13}$ Structure

Containing 112 atoms per unit cell $La_1(Fe_xSi_{1-x})_{13}$ is a difficult material to synthesise, with a tendency to form $\alpha - Fe$, high La phases and contain other

Table 3.2: *Table reproduced from Lyubina [10], $LaFe_{13-x}Si_x$ ΔS as a volume and mass term and ΔT_{ad}^{max}.*

Material	T_{max} (K)	H_f (T)	$-\Delta S_{max}$ $(kJm^{-1}K^1)$	$-\Delta S_{max}$ $(Jkg^{-1}K^1)$	ΔT_{ad}^{max} (K)	Reference
$LaFe_{11.6}Si_{1.4}$ (homogenised bulk)	196	1	147	22	4.2	Lyubina et al[65]
		2	160	24	7.8	
$LaFe_{11.6}Si_{1.4}$ (porous)	196	1	76	11	3.3	Lyubina[66]
		2	109	16	5.8	
$LaFe_{11.6}Si_{1.4}$ (nanocrystalline)	200	2	54	8	2.2	Lyubina[66]
		5	96	14		
$LaFe_{11.6}Si_{1.4}$ (homogenised melt-spun)	201	1	68	10	2.2	Lyubina et al[67]
		2	107	16	4.1	Lyubina[66]
		5	151	22		
$LaFe_{11.6}Si_{1.4}$ (homogenised melt-spun)	220	2	35	5		Lyubina et al[65]
		5	102	15		
$LaFe_{11.6}Si_{1.4}$ (homogenised melt-spun)	234	2	25	4		Lyubina et al[65]
		5	83	12		
$LaFe_{11.14}Co0.76Si_{1.1}$	267	1	52	7.2	1.8	Rosendahl Hansen et al[68]
$LaFe_{10.92}Co0.98Si_{1.1}$	293	1	38	5.3	1.2	Rosendahl Hansen et al[68]
$LaFe_{10.61}Co1.29Si_{1.1}$	327	1	30	4.2		Rosendahl Hansen et al[68]
$LaFe_{11.6}Si_{1.4}H_{1.2}$	273	5	118	17		Lyubina et al[65]
$LaFe_{11.6}Si_{1.4}H_{1.6}$	333	5	140	21		Lyubina et al[67]
$LaFe_{11.6}Si_{1.4}H_{2.3}$	342	5	120	18		Lyubina et al[65]
$LaFe_{11.35}Mn_{0.39}Si_{1.26}H_{1.53}$	282	1.6	75	11		Barcza et al[69]
$LaFe_{11.35}Mn_{0.39}Si_{1.26}H_{1.53}$	289	1.6	88	13		Barcza et al[69]
$LaFe_{11.35}Mn_{0.39}Si_{1.26}H_{1.53}$	295	1.6	82	12		Barcza et al[69] height

impurities. Employing long periods of annealing, several days at 1273 K or higher can reduce impurities but can still result in an inhomogeneous material containing several phases. Several synthesis techniques improve this annealing time and the purity of the material, for example melt spinning techniques lead to a vastly reduced annealing time for similar results [63, 64]. Reactive ball milling can also improve the homogeneity and annealing time of samples [65].

Reproduced from Lyubina [10] table 3.2 shows the properties of various growths, structures and material compositions. Their large Relative Cooling Power (RCP) and low magnetic hysteresis make the $La_1(Fe_xSi_{1-x})_{13}$ family of materials a very

attractive magnetocaloric to study. The relative abundance of the constituents and low toxicity also make it a more viable option for real-world applications. The $\approx 1\%$ volume change during the FOPT transition leads to a thermal hysteresis associated with degradation after repeated cycling through the transition.

LaFeSi has found extensive use in bulk due to the high change in entropy when doped with hydrogen, and high ability to tune the Curie temperature when doped with Cobalt. Vacuumshmelze GmbH provides the material in bulk form with a Curie temperature ranging from 261 K to 310 K, an ideal operating range for modern cooling needs. There is already some research into melt spun LaFeSi,[63, 70] where a dimension of the sample is reduced similar to those produced by PLD. Despite this, it has not yet been reported as a thin-film material (on the order of ~ 100 nm). This may be due to its tendency to develop other phases in large volumes of the bulk material ($> 5\%$).

3.3   Other Rare Earth Metal Based Materials

A large proportion of research has gone into rare earth metal-based alloys, of which GdSiGe and LaFeSi are both members. Over the last two decades others with large GMCEs close to room temperature have been discovered and researched, such as $ErCo_2$, $HoCo_2$, $DyCo_2$ [71, 72] and manganites of the form $La(X)MnO_3$ where X = Ca, Sr or Ba [73]. A comparison of some of the popular research materials by Franco et al. [4] and their entropy change with temperature presented in figure 3.5 left. A comparison of temperature change was also collected by Liu et al. [52] and presented in figure 3.5 right.
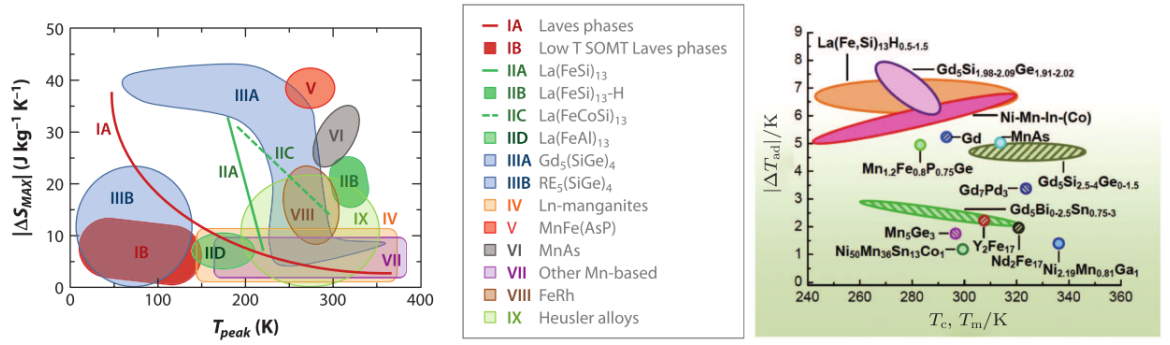
Figure 3.5: *shows the entropy change versus peak temperature measured for several materials on the left and temperature change on the right, reproduced with permission from [4].*

3.4   Thin Films

Magnetocalorics have been extensively studied in bulk form for many years, with a drastic increase in interest after the discovery of the GMCE in 1997 [8]. There has been a large quantity of research into the bulk properties of a wide range of materials, but there is still interest in finding new materials. An alternative method for exploring this phenomenon in detail is to grow these materials as thin films and novel devices [74]. Depositing multiple layers of magnetocaloric materials open a path to improving the FOPT transitions working temperature without reducing the effective MCE; this would entail growing multiple layers of magnetocalorics with relatively close T_c to each other on top of one another. The transition of one layer will then trigger the next to transition as well, causing a cascade in the material. Any study into nano-structured magnetocalorics will depend on both the starting bulk material and other factors only noticeable at the nanoscale such as particle size and strain.

In recent years there have been reports of many successful growths of magnetocaloric materials as thin films [75, 76, 77, 78]. However, it was in 2013 a

successful report of GdSiGe appeared [22]. Due to the large surface area to volume ratio when compared to bulk thin-film magnetocaloric devices seem ideal for thermal conductivity reasons. Second-order materials such as Gd have been processed as thin films previously [76]. They are shown to have a broadening of the entropy change in which the transition occurs, with their already wide operating temperature this further promotes their application for general temperature control systems. However to become viable the reduction in entropy and adiabatic temperature change are obstacles that will have to be overcome.

3.4.1   GSG thin film

GdSiGe has successfully been grown on a few occasions and its magnetic properties somewhat studied, Hadimani et al. being the principal investigators and the first to grow such a device [5].

Because it is a first-order transition material, GdSiGe thin-film behaves differently to its bulk counterpart. A broader transition similar to that of a second-order transition replaces the sharp entropy change peak seen in bulk, likely originating from the shearing being inhibited by the thin film size or orientation growth. This broadening could prove beneficial for commercial applications as it allows the material to operate over a wider temperature span.

Figure 3.6 shows a comparison between the thin-film and bulk GdSiGe, the left has composition $Gd_5Si_{2.7}Ge_{1.3}$ while the right has $Gd_5Si_2Ge_2$, the thin film has a reduction in entropy change, but its peak is over a broader temperature scale. The majority of Hadimani et al.'s thin-film $Gd_5(Si_xGe_{1-x})_4$ are on the order of 700 $nm \sim 1$ μm, but a significant change in the response compared to the bulk is observed.

44
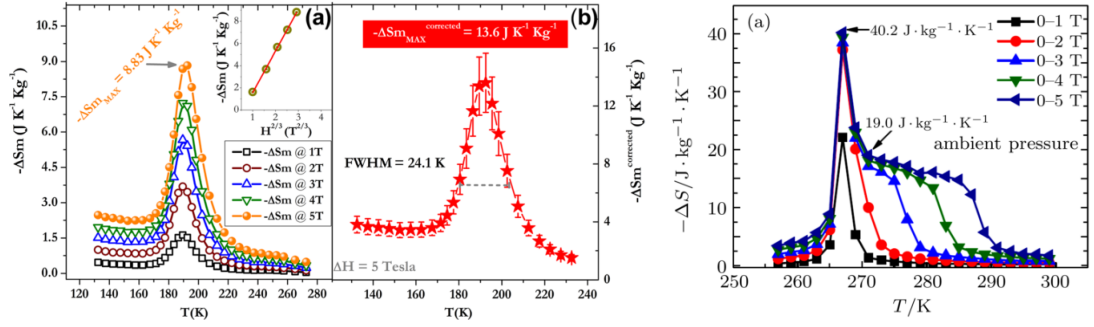
Figure 3.6: *Left (a) shows the change in entropy versus temperature for thin film GdSiGe, (b) is the corrected graph to account for unwanted phases within the sample, taken from [5]. Right is the same measurement for bulk material, taken from [1].*

3.4.2   Melt-spun $La_1(Fe_xSi_{1-x})_{13}$ ribbons

A distinct drawback of the $La_1(Fe_xSi_{1-x})_{13}$ system is the long annealing periods needed to reach the desired $NaZn_{13}$-type phase. Melt-spinning is a process known to reduce segregation within magnetic materials and increase the formation of metastable phases.

Melt-spinning $La_1(Fe_xSi_{1-x})_{13}$ is a promising preparation process due to its rapid solidification and peritectoid reaction that leads to a higher percentage of the desired 1:13 phase forming. Further annealing for approximately one hour, as a result, leads to a similar level of 1:13 phase compared to bulk annealed for several weeks. [65, 63] There is also evidence that this process can increase the Curie temperature when compared to the bulk, increasing the possible operational temperature. Both thermal and magnetic hysteresis decrease, two further drawbacks common to FOPT materials.

The process of melt spinning does cause a structural inhomogeneity across its thickness however, due to the cooling wheel employed having direct contact with one side of the ribbon, there is a cooling gradient formed across the thickness.

Hou et al. [79] showed a change in solidification and crystallisation processes across the ribbon dependent on the proximity to the Cu wheel used. They also showed that the side directly in contact with the wheel would form the 1:13 desired phase more readily than the opposite, concluding that the side furthest from the Cu wheel had almost no 1:13 phase forming.

3.5 Other Rare Earth Metal Based Materials

Thin film Magnetocalorics of Manganites have been more extensively studied than other materials, with the first reported MCE being reported in 1996 by Morelli et al. [80]. Morelli et al showed a MCE in a 2.4 μm thick layer of $La_{0.67}M_{0.33}MnO_3$ grown on $LaAlO_3$ substrate. Along with Hadimani et al [5] and Miller et al [76], Morelli et al would show a reduction in the MCE for thin film magnetocalorics when compared to bulk counterpart, a reduction that can be attributed to the finite scaling factor of nanostructures.

Later, Debnath et al would however grow $La_{0.7}M_{0.3}MnO_3/SrRuO_3$ lattices grown to a thickness of 200 nm and still observe a MCE. The MCE observed by Debnath et al would not show a reduced ΔS, but one that was equal to or greater than bulk counter parts[81], indicating nanoscale structural engineering of the thin films may mitigate the finite scaling factors. Inducing strain through piezoelectrics has also been shown to change the nature of MCE in thin film form, with Moya et al [82] showing an increased ΔS in $La_{0.7}M_{0.3}MnO_3$ grown on $BaTiO_3$.

3.5.1 PLD sputtering

LaFeSi(Co, H) has had no successful report of being grown as a thin film, as a material that shows performance close to that of GdSiGe with significant cost benefits it seems an ideal candidate for this research. Checca et al. [83] have

very recently reported on $La_1(Fe_xSi_{1-x})_{13}$ nanoparticles being produces via PLD, however.

PLD is a promising growth technique as it is known to maintain the stoichiometry of a complex target due to its fast deposition from the high powered laser. Checca et al. showed a tendency for a cubic structure to stabilise in a stoichiometry of $LaFe_5Si_8$, concluding that this structure is magnetocaloric and of the desired phase. The group show that there are two main types of nanoparticles forming during the PLD process, the first is a non-magnetocaloric amorphous particle containing La, Fe and Si. The second nanoparticles are a two shell structure; an outer amorphous layer surrounds an inner layer that crystallised to either the desired 1:13 $NaZn_13$-type phase or the undesirable $\alpha - Fe$ phase.

Using Selected Area Electron Diffraction (SAED) analysis, the group show that despite the $\alpha - Fe$ forming, it does not form in the same nanoparticles as the desired $NaZn_{13}$-type phase, concluding that an appropriate separation method (a high field magnet in proximity during deposition) may increase the levels of desired $NaZn_{13}$-type nanoparticles. There is an increase in the Curie temperature for these nanoparticles, but the amorphous layer introduces a magnetically disordered layer that remains disordered to temperatures down to 4 K.

3.6 Ising Model

The Ising model is a simple and well studied model in statistical mechanics. First being described and investigated by Lens and Ising [84, 85] to study magnetic phase transitions in ferromagnetic materials, they introduced an exact solution for the one-dimensional model.

It was two decades later that Onsager [86] published the two-dimensional solution for the rectangular spin-1/2 lattice, this led to the Ising model gaining its prominence in the statistical mechanics' field.

Despite initially being devised for the study of magnetism, the Ising model has found useful applications in many systems that consider many-body interactions in a wide variety of research fields. Other studied non-magnetic specific physical phenomena include solid-liquid-gas transitions and phase coexistence, and ordered and disordered systems for pure materials and alloys [87, 88]. There is also use of the Ising model in biophysics/biology research where it has successfully and accurately modelled DNA helix melting and combining, cancerous tumour growth and enzyme and lipid critical behaviours [89, 90, 91]. The Ising model has even found application in the financial district, helping economic researchers further understand the driving forces behind a populations buying habits and economic segregation [92].

The focus of this work is however, on the original purpose of the Ising model, the application to phase transitions within ferromagnetic materials. The application to rare-earth materials is well documented [93] due to their long-range interactions which tend to cancel out the short-range components. The dominant long-range interactions have led to a considerable agreement between the theoretical Ising model and experimental data. Density Functional Theory (DFT) by both Pecharsky et al. and Samolyuk et al. [53, 94] have shown a relationship between the cohesive energy and magnetism of the two phases in question for $Gd_5Si_2Ge_2$ at 263 K, where a transition from the Orthorhombic to the Monoclinic phase happens at lower temperatures than the magnetic transition, driving a sudden magnetic change and a FOPT.

3.6.1 SOPT

Anejdal et al. [12] have previously shown the use of Ising models for studying magnetocalorics, finding a Curie temperature close to experimentally determined for a MnBi material by applying the experimentally determined crystal parameters to the array.

Sokolovskiy et al. have extensively studied [49] Heusler alloys by using DFT to calculate the many starting parameters and then employing them in an Ising/Potts model to investigate the magnetocaloric behaviour of various materials. They predict an increase in the inverse magnetocaloric effect for Heuslers with increasing quantities of Cr, Co or Al.

3.6.2 RKKY

There has been previous work on the use of RKKY in the Ising model reported by Ikeda et al. [95] where they successfully simulated pyrochlore $Pr_2Ir_2O_7$ at its lower temperature but found its transition to be a FOPT, where experimentally it is shown to be SOPT.

Motlagh and Rezaei also use the RKKY model to investigate amorphous, mixed spin systems where the RKKY interaction determines the exchange interaction lower than a given distance. By comparing the standard square and hexagonal lattice to a randomly distributed lattice, they show that a random lattice dominated by the RKKY interaction has a complex phase relationship similar to both the square and hexagonal. The ratio of the mixed spins also leads to a magnetic frustration within their system.

Pecharsky et al. showed the exchange coupling for Gd-Gd in $Gd_5(Si_xGe_{1x})_4$ vary from a positive to a negative value with increasing distance determining that the RKKY interaction is the source. However, Pecharsky et al. stated that the discontinuous transition is due to the super-exchange between layers being broken [3].

3.6.3 Ising model studies of $Gd_5Si_2Ge_2$

More recently, Jabrane et al. [93] showed simulations of $Gd_5Si_2Ge_2$ in its Orthorhombic phase and predicted a SOPT but neglected to include or compare to the Monoclinic phase. Despite this, Jabrane et al. report a good agreement

between their model and experimental data, with an $-\Delta S = 9.97 \; J/kg.K$ in a field of 5 T. They do however report a T_c for $Gd_5Si_2Ge_2$ at 263 K, significantly below the experimentally determined value. They also show that there is a large dependence of the MCE on the structure.

$Gd_5(Si_xGe_{1x})_4$ will later be presented in both its Orthorhombic and Monoclinic phase and give an energy comparison that leads to a different phase transition than reported by Jabrane et al.

3.6.4 Other models for MCEs- Bean-Rodbell, Heisenberg and potts

Potts and Heisenberg's models are similar statistical models to the Ising model with higher dimensionality for the spin variable. Collectively they are known as n-dimensional models and are also useful models for simulating and predicting the magnetocaloric effect for various materials.

Comtesse et al. [96, 93] use first principle DFT calculations in conjunction with a Potts model to describe the Heusler alloy, Ni-Co-Mn-In, predicting a significant inverse magnetocaloric effect resulting from a FOPT at 320 K and a smaller SOPT magnetocaloric effect at 380 K. They conclude that despite the presence of itinerant electrons, the localised electrons affect the size of the magnetocaloric effect.

Szalwski et al. use a Heisenberg model to study the magnetocaloric effect more generally [97]. Making a comparison to the mean-field approximation (MFA), they show an advantage to their model over the MFA in its ability to reproduce thermodynamic characteristics that are non-physical in the MFA model. They also show a comparison to phenomenological models derived from the Landau model of phase transitions and Arrott-Noakes equation, stating the superiority in n-dimensional models as they lack the need for extensive prior experimental data for the materials.

Methods and Experimental procedures

4.1 Introduction

In this chapter we will cover the techniques used for the simulations, fabrication and measurements of magnetocaloric thin films. Simulations are written using an Ising like model to infer an entropy change in the system, fabrication is performed using pulsed laser deposition and atomic force microscopy is used to confirm its thickness and granularity. Vibrating sample and superconducting quantum interference device magnetometry are all used to understand the magnetic phase transition, with x-ray reflectometry, x-ray reflectometry and polarised neutron reflectometry used to understand crystal structure, roughness and material layers

and their interplay with one another.

Each subsection is laid out as follows: theory explanation, equipment/model explanation and sample results or images to help the reader understand the experimental and computational procedures used and results encountered.

4.2   Modelling

Monte-Carlo Ising simulations are a widely used technique in computational physics. Their main draw is the cellular automata nature of the model in which neighbouring sites and randomly generated numbers determine one of a set of finite arrangements for each randomly selected site. This allows for thermal and magnetic averages to be calculated for complex, many body systems with statistical fluctuations, often leading away from a random initial state into something more homogeneous and stable [98, 99, 100].

4.2.1   Ising Model

The methods that will be discussed in this thesis implements a standard Metropolis algorithm to generate lattice values and evaluate the probability of a spin flip at a given site. This is done by comparing the initial energy E_i with that of the newly flipped site E_f, if the difference ΔE, where $\Delta E = E_f - E_i$, is < 0 the newly flipped site will remain flipped. If ΔE is > 0 then the probability of flip acceptance is calculated using a Boltzmann distribution

$$p_B = e^{-\Delta E/k_b T} \tag{4.1}$$

where p_B is the probability, k_b is the Boltzmann constant and T is the average temperature at the point of flipping.

A random number, p_r at this point is generated and compared to p_B. If $p_r < p_b$ the newly flipped site will remain flipped and a new site will be selected

for the same procedure. Should $p_r > p_b$, the site will return to its pre-flipped state and a new site will be selected. This continues for a finite, predetermined number of iterations.

The bulk of the simulation has been written in C with post processing written in python. The 3 dimensional lattice has been written to match the crystal structure of GdSiGe in both its Orthorhombic and Monoclinic phases as seen in figure 4.1 where only the rare earth element sites are considered to have a non-zero spin.
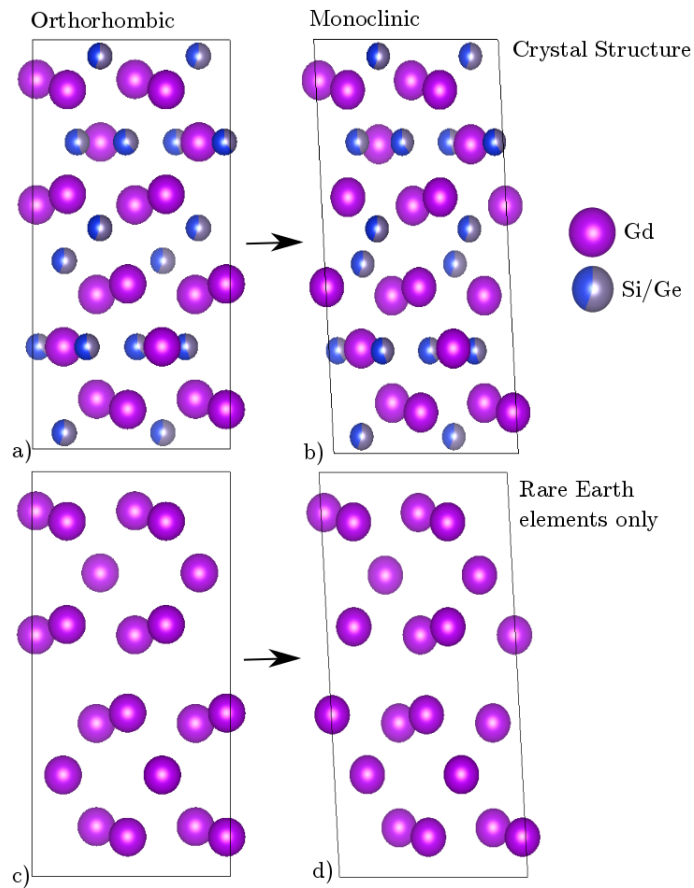
Figure 4.1: *a) Orthorhombic structure of GdSiGe. b) Monoclinic structure of GdSiGe. c) Orthorhombic structure of GdSiGe with only the rare earth elements. d) Monoclinic structure of GdSiGe with only the rare earth elements. the blue/grey represents the preference of the site to Si and Ge respectively.*

Simulations are run in the temperature range considered to be of interest for GdSiGe. At each point as it cycles through field and temperature, the previously discussed metropolis algorithm is run to an equilibrium point, where the code calculates the average magnetisation and energy of the systems. Subsequent variables are calculated post simulation from the magnetisation and energy data, such as specific heat, susceptibility, magnetic entropy and entropy change. Similar post processing is conducted on data from SQUID measurements and will be discussed in section 4.5. An example output of magnetisation data is given in figure 4.2.

4.2.2   Model Description
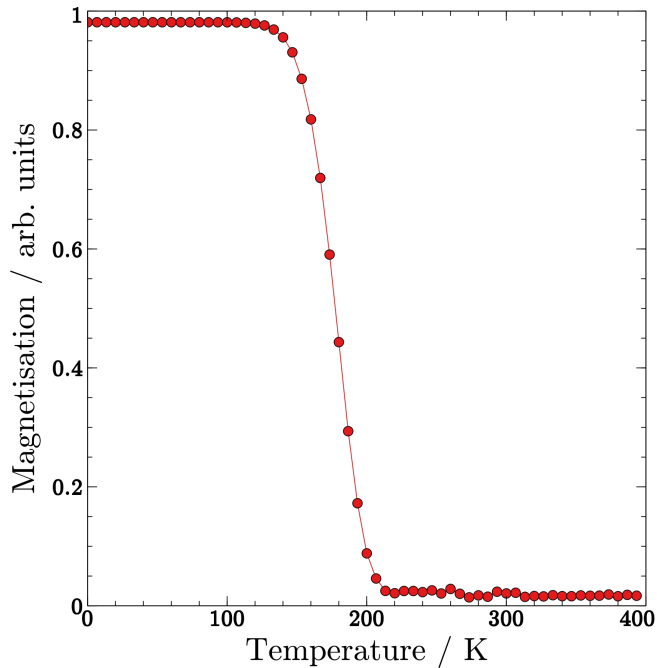
Figure 4.2: *example magnetic data taken from an Ising model simulation showing the transition from FM(< 150 K) to PM(> 220 K). With an intermediate regime existing between the FM and PM states).*

A FM state is seen at temperatures below 150 K, indicating that despite the random initial configuration, the vast majority of spins have aligned themselves with one another, producing a situation within the simulation that can be assigned to a FM like aligned spin state within a real structure. At temperatures above 220 K the magnetisation tends to 0, indicative of a PM state. In this regime the thermal fluctuations of the system, arising from the competition between p_b and p_r, drive the system into a disordered, random state.

Simulations also show a non-zero magnetisation at 0 T field for temperatures higher than the transition point that is not present in real world GSG. This non-zero moment at zero field is present in the results due to edge effects in the simulation, where a difference in the number of nearest neighbours leads to the outermost sites remaining in a ferromagnetic state throughout the simulations.

4.3   PLD

4.3.1   Operational Theory

Pulsed Laser Deposition (PLD) is a technique used for creating thin film materials via a high powered laser. A simple explanation is that a high powered laser is used to ablate a target material, creating a vapour which travels towards a substrate and is deposited to form a thin film of the target on top [101]. PLD is known for its good transfer of stoichiometric material from target to substrate and is chosen for this reason.

The laser is focused to a 1-2 mm point to hit the desired target within a vacuum chamber, repelling a plume of particles from the target parallel to the target surface, due both to recoil from the target and the Coulomb force, shown in diagram 4.3.

The depositions are performed within a chamber that has been pumped down to a low pressure of 7 $\mu Torr$ for several hours, to remove any oxygen or other

potential reactants, then filled with a known gas to allow for interactions before deposition or to remove some kinetic energy from the vapour as it is deposited and increase the size of the vapour plume. If the vapour has sufficient energy upon making contact with the substrate it can reflect back into the chamber and not deposit, interact with the substrate, damage already deposited material, change phase and/or cause re-emission of deposited material so control of the chamber atmosphere is crucial to the material growth.

The nucleation of the particles on the substrate is further affected by the substrate wafer itself, the heat and roughness directly effect the stoichiometry of the material forming. The substrate heat allows for the particles to diffuse across its surface to form islands or fall into steps. The substrate roughness will define how the device grows. If the surface is rough or has been intentionally cut to form steps the particles can diffuse towards the step edges and continue to create steps away from the substrate. Should the surface be sufficiently flat, the diffuse particles can preferentially form islands, which increase in size until they make contact with each other and form secondary islands. This process allows for a layer formation as opposed to the steps. The level of diffusion is all dependent upon the energy of the deposited material, with contributions from the substrate temperature and the remaining kinetic energy, making the substrate choice and deposition temperature further parameters to consider [22, 101, 102].

Ablation will change the topology of the target over time, causing troughs to be created by the laser. This will affect the uniformity of the plume produced, altering the deposition of the material. Rotating targets and moving the laser are used to evenly ablate the target surface, mitigating as much as possible as any factors causing a non uniform plume.
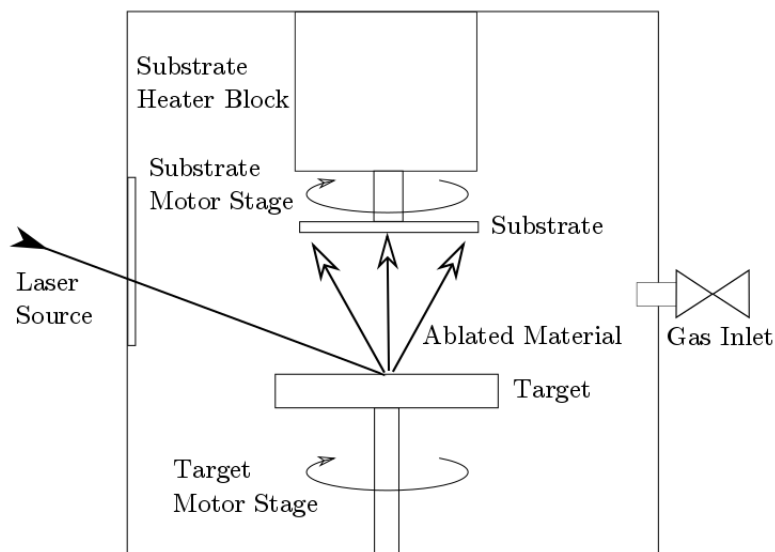
Figure 4.3: *Basic construct of a PLD chamber, the laser light enters through a glass window to the left, hitting the target and creating a plume of ablated material, both substrate and target are capable of rotating, a heater is attached above the substrate and a gas inlet allows for controlled flow.*

4.3.2   Equipment Description

The PLD used for this work has motors attached to the target and substrate to allow them to spin. There is also a mirror system allowing the laser to raster up and down the target as it rotates, allowing the target to ablate evenly, reducing the laser ruts created within the target and causing uneven amounts of vapour plume over time.

For the deposition substrate we used Si wafers with an oxide barrier layer, as well as AlN substrates. Both substrates were held at the same point next to each other on a spinning substrate holder, so every comparison between the substrates is from the exact same deposition process with the samples rotating within the plume to get a similar exposure. The chamber is evacuated to as low as 7 $\mu Torr$ using a turbo pump, allowed to sit at this pressure for several hours, and then

filled with Argon gas. It has been shown that the pressure within the chamber can affect the final surface roughness [103] so a range of pressures up to the operational maximum of 20 $mTorr$ were used. The laser used for the deposition has a wavelength of 248 nm and is capable of being pulsed at frequencies up to 100 Hz, with sustained frequencies up to 20 Hz. Once deposited, the films were allowed to cool at a steady, prolonged rate to avoid any damage or change to the structure. Substrates can be heated from room temperature to 1273 K, but depositions are conducted between 293 K and 723 K, justification for this is given in chapters 6.2 and 7.1.

Literature suggests that GdSiGe deposited onto silicon experiences a large amount of interfacial reactions [104] that can alter the target material, as such an oxide diffusion barrier for the Si wafers is used.

4.4   AFM/MFM

4.4.1   Operational Theory

An AFM uses a small tip attached to a cantilever, which moves up and down over the surface of a material. Depending upon the choice of tip material, several forces can deflect the tip away from the materials surface and then be measured, including Van-der-Waals forces, dipole-dipole interactions and mechanical contact forces for standard tips, electrostatic and magnetic forces for tips coated in a magnetic material (known as Magnetic Force Microscopy (MFM)) etc. A laser is reflected off of the top of the cantilever and its reflected spot is detected upon a four quadrant photo-diode. As the tip is repelled up and down the laser moves across the surface of the diodes altering the output voltage and allowing for the tracing of the movement and the position of the tip. The tip moves along in the x-y plane, allowing for the z plane to be measured by the reflected laser and building up a three dimensional map of the topology of the device [105, 106, 107].

There are two main ways to use an AFM; contact mode, and tapping mode. The first involves dragging the tip across the surface and measuring the response. The second vibrates the tip as it moves across, creating a less invasive or damaging way to measure the surface. For this work, tapping mode was used exclusively.
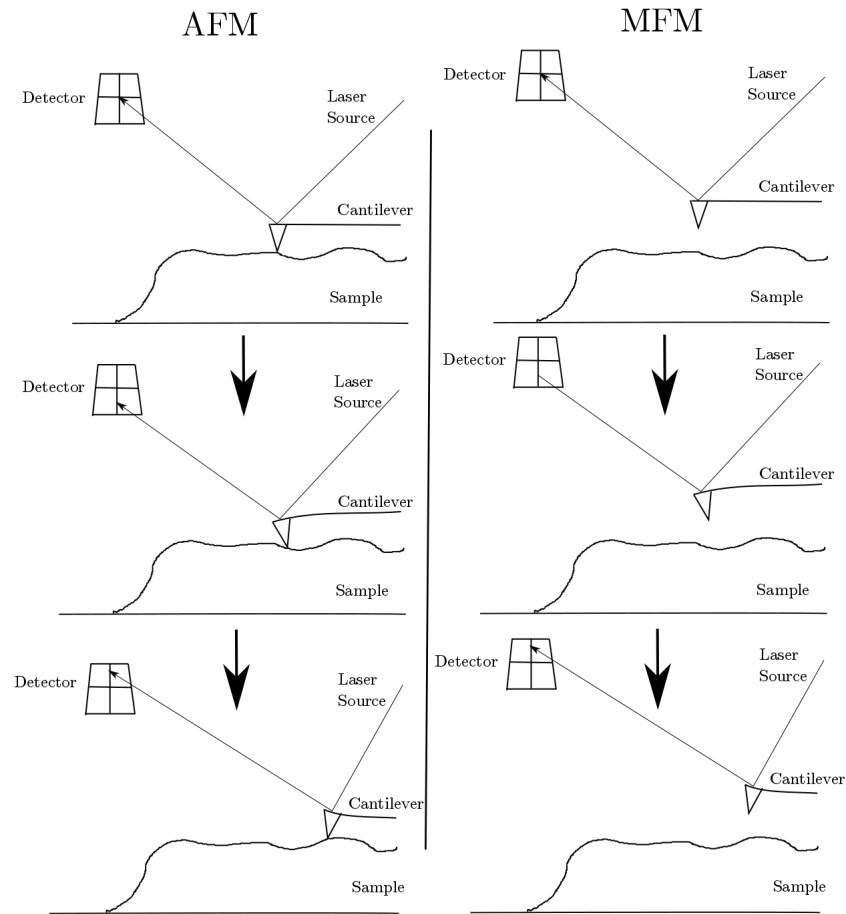
Figure 4.4: *Schematic diagram of the basic function of an AFM/MFM. proceeding from top to bottom shows the progression of the cantilever and tip along the surface and its affect on the laser path to the detector.*

AFM is not limited to a 2 dimensional image and is capable of much higher resolutions, but does come with its own limits. Often limited in scan size and each scan taking many minutes if not hours to complete make mapping a sample

a lengthy process. Tip interaction with the surface will also alter the raw data, unlike SEM the sample can cause artefacts by restricting/altering the tip motion. The tip does not form a perfect point, is usually polyhedron shaped and will degrade over time, meaning sections of the sample with steep edges or tall/deep features can come into contact with sections of the tip not directly at the point and create erroneous topography measurements.

Tip interaction with the sample does allow for more information to be gleaned however, given the correct tip selection and understanding of the data magnetic and electrostatic interactions can be measured, or with more modified tips thermal distribution, electrical conductivity and material stiffness. MFM is a secondary technique that can be used with the same equipment but an alternate magnetic tip. The basics are the same as the AFM, a tip moving across the surface of a sample measuring its topology, but after a standard AFM measurement is taken the tip is lifted (often $\sim$50-100 nm) above the sample and retraces the same path.

At this height above the sample the magnetic stray fields interacting with the coated tip are dominant, so a difference of the two measurements can be used to deduce a magnetic response map of the sample.

4.4.2 Equipment Description

A Digital instruments Dimensions 3100 AFM is used with a Bruker SCM-PIT-V2 SiSb tip, coated with PtIr for AFM and a Bruker MESP-LM-V2 SiSb tip coated with CoCr for MFM. The AFM is primarily used for edge step measurements like that in figure 4.5a and 4.5b to determine the sample deposition thickness and to measure the topological properties such as grain size and roughness. Figure 4.5a shows a step edge raw image from an AFM scan with the Si substrate to the left and GdSiGe deposit to the right. The image colour scale represents the height measured by the tip.

Post-processing is an important component of AFM as the piezoelectric nature of the scanner, large objects on the surface and tip wear can all cause artefacts to appear on images. Figure 4.5c gives a profile line scan over the edge in figure 4.5a, where it is evident that calculating a height would not be possible from the raw data and some form of correction is required.
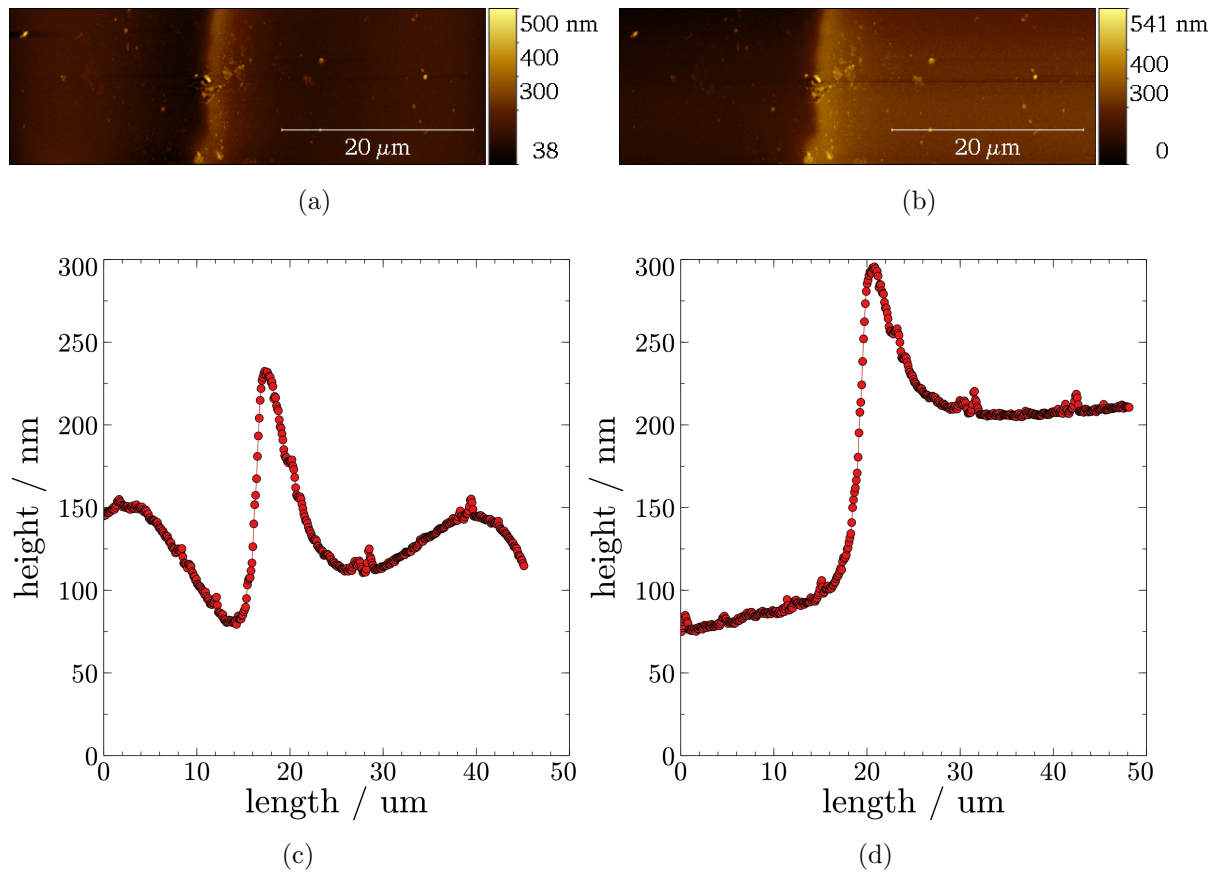
Figure 4.5: *a) shows the raw AFM image scan of an edge. b) the corrected image showing the same edge. c) gives a line scan over the raw image edge. d) gives a line scan over the corrected image edge.*

Gwyddion, the software used in this thesis, offers several data correction techniques. Simple 2D corrections can be applied using a plane level process where a flat plane is subtracted from the raw data to give a flat surface. Three-point

levelling, where the user marks three points that should be at the same level and a background plane is computed and subtracted from the raw data. Polynomial background removal, where a polynomial of a given order is fitted and its plane subtracted from the background. More complicated techniques for correcting drift due to thermal fluctuations and affine distortion can also be used if the image is rotated or straight edges appear to have a curve at the edges of images. Scanning artefacts such as scarring and step lines from the sample moving or incorrect height measurements can also be corrected with a polynomial line subtraction along the scar or height correction by matching sections in the slow scan axis. All techniques allow for a material thickness to be calculated from figure 4.5b and 4.5d.

4.5 SQUID

4.5.1 Operational Theory

The SQUID (Superconducting QUantum Interference Device) is considered to be the most sensitive of all instruments for measuring a magnetic field. [108] A DC SQUID, shown in figure 4.6, consists of a superconducting loop with two Josephson Junctions in each branch. An input current in the absence of an external magnetic field will be equal in both branches of the loop so that $I_a = I_b$, but the application of an external flux will induce a secondary screening current in both branches that circulates the loop causing $I_a \neq I_b$. With a sufficient flux a critical current can be reached in either branch and register a voltage across the device.
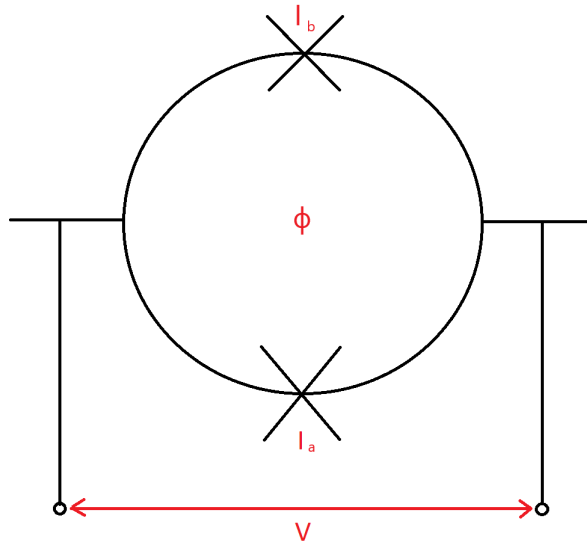
Figure 4.6: *schematic diagram of a basic SQUID, with a superconducting ring, 2 Josephson junctions and a voltage measurement across the device.*

The enclosed flux quanta within the loop must be an integer number, meaning as the applied flux increases, the SQUID will eventually prefer to increase the enclosed flux and in doing so reverse the induced current flow. This continues for every half-integer change in applied flux, resulting in a periodic relationship between the applied flux and voltage registered where each period is equal to a single flux quanta.

The SQUID being used operates in conjunction with a series of pick-up coils, a diagram is shown in figure 4.7. As SQUID Magnetometers are very sensitive to outside magnetic fields, gradiometer pick up coils can be used to exclude most external fields without interfering with the sample measurement. The response of a single coil to a magnetic dipole reduces as $\frac{1}{z^3}$, so a magnetic source closer to a single coil will have a significantly higher coupling to that coil. But a source at a larger distance from two or more coils will have a relatively uniform response in all coils, effectively rejecting most of the distant signal sources. Two or more gradiometers can be connected in series to enhance the rejection of distant sources.

A second order gradiometer is shown in figure 4.7 (b) and is the set-up used for this work.
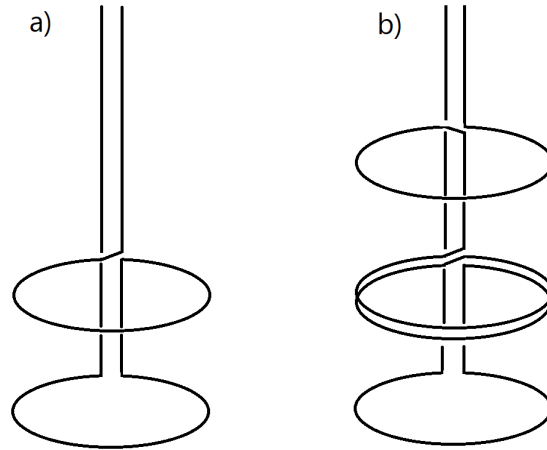
Figure 4.7: *Shows a first and second order gradiometer set up.*

Use of a SQUID for magnetocaloric measurements is considered to be an indirect measurement as the temperature of the device is not directly or continuously measured. This is the more common form of indirect measurement due to its speed and simplicity compared to using a calorimeter.

The more common methods for magnetocaloric measurements using a SQUID system are to use either an isofield or isothermal measurement. During an isofield measurement the magnetic field B applied is held at a constant value and the external temperature T of the SQUID is altered in regular steps. The applied field is then changed and the process repeats.

An isothermal measurement is conducted in a similar fashion whereby the system is brought to a temperature T and the field is swept through to a maximum and back again. The temperature is then increased or decreased and the process repeats. In both isothermal and isofield measurements the magnetisation is measured at each step interval, but because isofield measurements are less prone to causing spikes in ΔS calculations they were used for the majority of this work.

The relationship, equation 2.1, shows how the entropy is related to the two

controlled values of temperature T and field B and the measured value of magnetisation M. But due to the discrete temperature values that will be used for an isothermal measurement the ΔS values can be approximated to be

$$\Delta S = \Sigma_i \frac{M(T + (\frac{\Delta T}{2}), B_i) - M(T - (\frac{\Delta T}{2}), B_i)}{\Delta T}\Delta B_i \qquad (4.2)$$

Here ΔB_i is the step in field and ΔT is the step in temperature. A similar equation exists for the derivative of temperature [38].

This method is proven effective for novel materials that are completely reversible and show no hysteresis, however, the presence of a phase change shows a thermal hysteresis. To overcome this problem the measurement will have to form a loop whereby the temperature is measured in steps that are well below and above the phase position to ensure complete saturation of the new state through the device and the process must be completely reversed. Both isothermal and isofield measurements are used to characterise the magnetic component of phase transitions in this work [10].

4.5.2   Equipment Description

The main SQUID used is a Quantum Design MPMS XL, capable of fields up to 7 T and a temperature range of 1.9-400 K. The equipment has an absolute sensitivity of $10 \times 10^-11 \ J/T$ at 0-2.5 T and $600 \times 10^-11 \ J/T$ at 2.5 - 7 T. The temperature ranges used are 2-400 K as this covers the area of interest for room temperature magnetocalorics and allows for low temperature observations. Fields up to 3 T are used as samples are saturated well before this point.
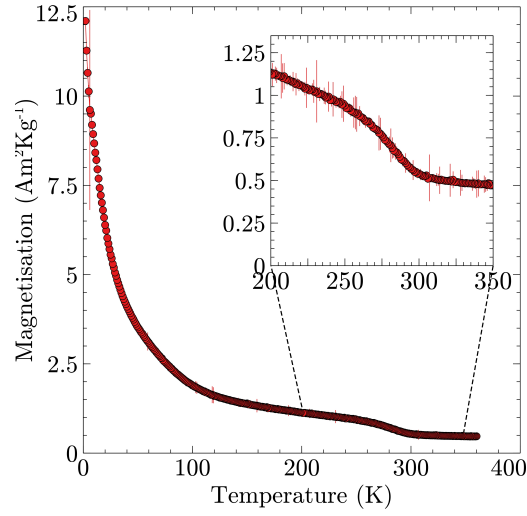
(a)
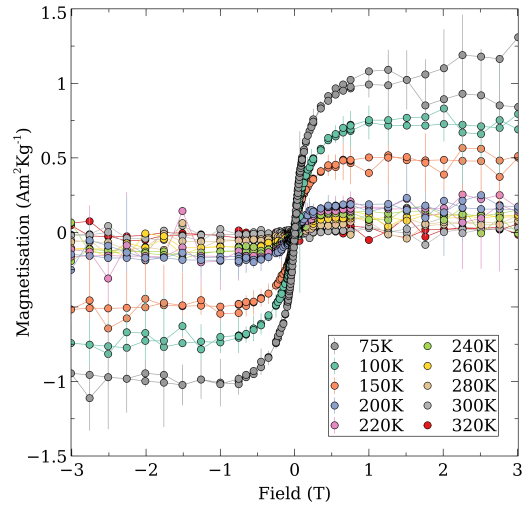
(b)

Figure 4.8: *a) magnetisation as a function of temperature for GdSiGe at a constant field of 200 mT. b) Hysteresis loops at temperatures from 75 K up to 320 K for GdSiGe.*

Figure 4.8a shows a magnetic temperature response of a magnetocaloric material. The change in gradient close to room temperature, enlarged in the inside graph, is indicative of a phase change. Figure 4.8b shows several hysteresis loops around this temperature, a transition from highly FM to PM can be seen and

this data can later be used to calculate an entropy change [22].

4.6   VSM

4.6.1   Operational Theory

VSM is a widely used magnetic measurement technique that relies on the electromagnetic inductance from Faraday's law, $\epsilon = -d\Phi_B/dt$, where a change in magnetic flux induces an EMF in a set of pick-up coils [109, 110]. As Faraday's law states there needs to be a change in magnetic flux, the sample is attached to a sample rod vibrating perpendicular to the face of the coils and an applied magnetic field as shown in figure 4.9.
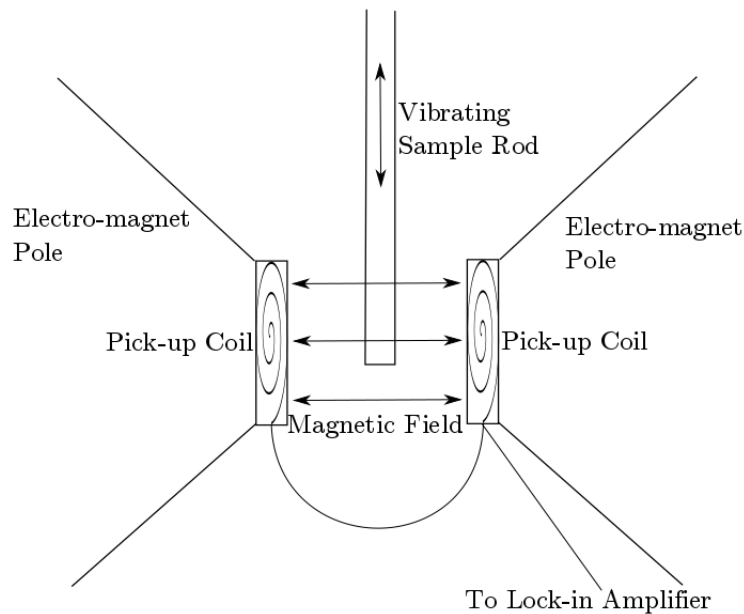
Figure 4.9: *schematic diagram of a basic VSM, with two electro-magnet poles to either side providing a field, pick up coils located within the magnets and a sample rod vibrating between the coils.*

This setup creates an EMF within the coils that is proportional to the sample

magnetisation. As the external field is motionless compared to the coils its contribution is ignored except where it has an affect on the sample itself. The coils are wound in opposing chirality cancelling each others contribution, theoretically allowing for just the sample space magnetisation to be measured.

4.6.2   Equipment Description

The equipment used is a Lake Shore cryotronics 7410-S VSM capable of fields of 3.42 T at room temperature, vibrating at 30 Hz.

Calibration is done by saturating the provided Ni sample to a known field of 0.5 T and setting the moment measured to a value of 6.987 $\times 10^{-3}$ J/T. As the samples to be measured are on the nanoscale, the time to thermal equilibrium is expected to be lower than 0.1 s, meaning direct phase switching measurements will not be possible.

4.7   XRR

4.7.1   Operational Theory

X-Ray Reflectometry (XRR) is a technique used to determine thickness, density and roughness for one or multiple thin film layers. XRR can be employed on both crystalline and amorphous layers. The technique relies upon the total reflection of the X-ray with respect to the surface and/or interface of the material. The measurement relies upon a source and detector, figure 4.10, being rotated about the sample and the incident rays recording as a function of the angle from the sample surface.
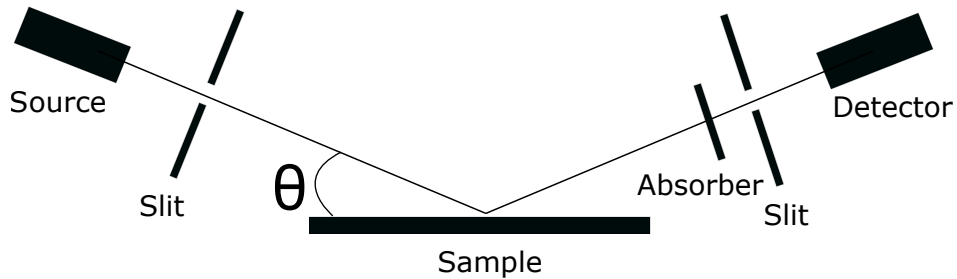
Figure 4.10: *Diagram of a XRR set up including the source, sample, detector slits and absorber.*

According to Snell's law, at a boundary an incident ray will be partially reflected at an angle Θ_r, while the rest will be transmitted through the boundary at angle Θ_t. Given a perfectly flat single surface the detected rays as a function of 2Θ would have a smooth decrease as 2Θ increased. But as secondary layers and interfaces are introduced, rays that were transmitted internally at angle Θ_t will now cause further reflections and internal transmission, leading to interference between the reflected rays and visible fringes in the detected rays vs 2Θ plot.

A differing electronic density between materials and at interfaces will cause interference in reflected X-rays that creates oscillations in Q called Kiessig fringes. The electron density and roughness can be estimated by fitting the data as a function of the 2Θ and the resulting plot used to find the materials thickness and density. The reflected intensity drops off as Q^4 for 2Θ so longer sampling times are needed for higher 2Θ.

For X-rays the angle at which total reflection occurs, the critical angle Θ_c, is much smaller than for visible light, meaning low grazing angles are needed. Θ_c is dependent on the materials electronic density at the surface, the larger the

critical angle the deeper the x ray will penetrate into the film.

4.7.2 Equipment Description

XRR was performed at the ISIS Materials Characterisation Laboratory using a Rigaku SmartLab 1. All XRR measurements are at 0 to 8 2Θ at room temperature with a wavelength of 0.154 nm.

4.7.3 GenX

The GenX software package provides a simulation and fitting suite for XRR. GenX utilises the differential evolution algorithm to fit both XRR data and neutron reflectometry data. GenX requires an input model to fit to and provides a Figure Of Merit (FOM) output to assess the model. To build the input model layers are added and defined with a range and as the evolution progresses GenX attempts to minimise a difference between the models results and the loaded measurements. For all measurements, the Chi^2 FOM, a figure of merit comparing the simulated to observed results, option is compared for analysis, Scattering Length Density (SLD) measurements are also produced and analysed.

4.8 XRD

4.8.1 Operational Theory

X-Ray Diffraction (XRD) is a technique used to identify crystalline phases and orientations in a sample. It is a non-destructive technique that utilises the interference pattern caused by the crystalline structure.
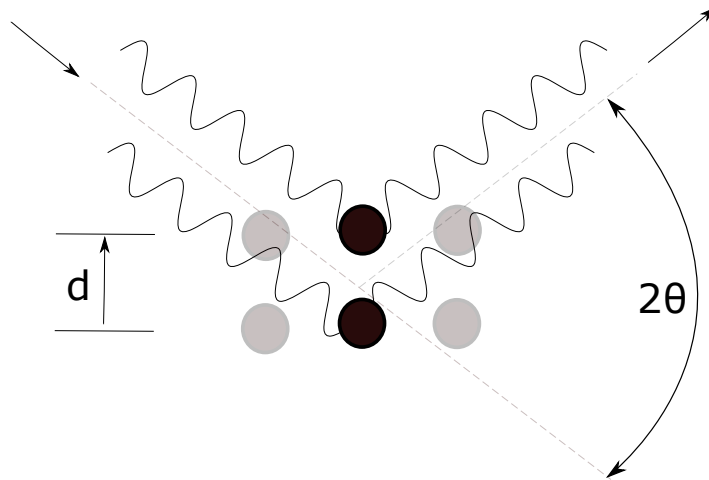
Figure 4.11: *Interaction of incident X rays creating outgoing, in phase rays. where d is the grating constant and Θ the glancing angle.*

Electrons around an atom will oscillate at the same frequency of an incident x-ray. In a disordered system this will create destructive interference in all directions but because of the periodic nature of crystalline structures an X-ray source will cause constructive interference at specific angles, figure 4.11, that satisfy Bragg's law. This is due to the crystalline ordered structure creating waves in phase with one another at specific angles that can be found with the Bragg relationship equation 4.3

$$n\lambda = 2dsin\Theta \tag{4.3}$$

Where n is the diffraction order (a positive integer contained in the set $\mathbb{N}_1$), λ is the wavelength and should be on the order of atomic spacing within the sample, d the grating constant and Θ the glancing angle. Here, Θ is measured from the incident ray, not the surface as with Snell's Law.

This pattern will correspond to the crystal structure and form defined X-ray

beams at given angles, by rotating the sample and the detector and measuring the intensity of the diffracted rays a plot of 2Θ vs counts can be generated. Converting these plots into d-spacing allows for identification as each structure will have a unique set of d-spacings. Powder Diffraction Files (PDF) are available from the Crystallography Open Database (COD) site for comparison.

4.8.2 Equipment Description

The same Rigaku SmartLab 1 described for XRR was used for the XRD measurements. All measurements are in a range of temperatures from 200 K to 350 K. All scans were taken from 5 degrees to 100 2Θ, with a step size of 0.01 degrees and a scan speed of 3.12 steps/min.

4.8.3 PDXL

The PDXL powder diffraction analysis software suite provided post-processing. The suite was capable of automated phase identification, quantitative analysis, lattice constants refinement, Rietveld analysis, ab initio structure determination and had access to the Crystallography Open Database for comparison.

4.9 PNR

4.9.1 Operational Theory

Polarised Neutron Reflectometry (PNR) is a technique similar to XRR but reflected neutrons, not X-rays, provide the structural information. PNR provides depth resolved measurements down to 2Å, giving a laterally averaged magnetic structure measurement.

Similar to XRR, the technique requires a source of collimated neutrons shone onto a thin film sample and measuring the reflection count as a function of angle.

Polarising the neutrons differently will provide additional magnetic data when measuring a magnetic sample or if the sample is in a magnetic field.

The neutron interaction occurs with the nucleus of the atoms, whereas X-ray reflectometry is an interaction with electrons. Due to the different atomic form factors, the technique is sensitive to other elements present, especially lighter elements, and is even capable of differentiation between isotopes of the same material. Coupled with XRR measurements, PNR offers a detailed description of thin film materials magnetically and structurally. PNR allows for the study of interfaces and surfaces at an atomic scale. The incident neutrons also have a spin, providing magnetic information on a layer by layer basis.

4.9.2 Equipment Description

All PNR measurements were taken at the POLREF line at ISIS. The ISIS neutron source uses a Tungsten-Tantalum spallation source to produce the neutrons from a synchrotron accelerator, which uses hydrogen ions to produce protons for the accelerator. The beamline then uses a beam-bender and a series of collimators and polarisers before the source hits the sample as shown in figure 4.12.
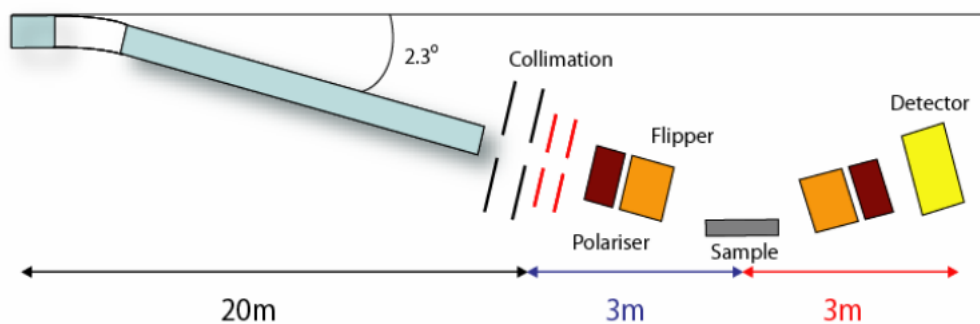
Figure 4.12: *Layout diagram of POLREF, reproduced from [6].*

The outgoing neutrons are then measured by the moving detector that swings out on an arch to get the count as a function of angle. Wavelengths of 1 - 15 Åare

available with sample fields of up to 10 T and a cryostat environment capable of $< 2\ K$.

GenX, described in the previous XRR section, is also used for the PNR analysis. Following a similar process, data is uploaded and layers defined, but multiple sets of data can be uploaded and used to define different polarisations and different probe variables.

4.10 Summary

In this chapter, the basics and techniques for the simulation, preparation and characterisation of thin-film magnetocalorics are laid out. PLD is used to create thin films of GdSiGe and LaFeSi of $\sim 100 \ nm$ thickness in various chamber conditions and substrate temperatures. AFM and MFM are used to measure the thickness and granularity of the samples in preparation for magnetic measurements; X-rays, Polarised neutrons and fitting software provide an understanding of the structure and density of the deposited material. VSM and SQUID are used to understand the materials bulk magnetism response. An Ising model is also used to investigate the GdSiGe material further, to give an understanding of the phase transition on a more theoretical level.

<div align="right">5</div>

Phase changes in a $Gd_5(Si_xGe_{1-x})_4$ Ising model

5.1 Introduction

This chapter will describe the application of Ising models to a FOPT system with a crystallographic phase change at the critical temperature, T_c. $Gd_5(Si_xGe_{1-x})_4$ experiences both a SOPT and FOPT transition dependent upon the value of x as described in chapter 3. The Ising simulations described in this chapter have a particular focus on the FOPT regime by comparing the total energy of a monoclinic and orthorhombic phase as a function of an external field, temperature

and an introduced variable that described the bonding energy difference arising from x.

DFT simulations from Samolyuk et al. describe a similar comparison between the two dominant phases of $Gd_5(Si_xGe_{1-x})_4$. Showing that the free energy of the two phases approaches each other in value, as a function of temperature, and at a point, become indistinguishable. Samolyuk et al. describe this point as the $Gd_5(Si_xGe_{1-x})_4$ systems T_c [94].

Choe et al. also describe both the breaking of the super-exchange during the transition, leading to latent heat and thermal hysteresis, and the altering of the exchange interaction $J(R)$ driven by the RKKY interaction in the rare earth Gd dominant system, figure 5.1 [7].
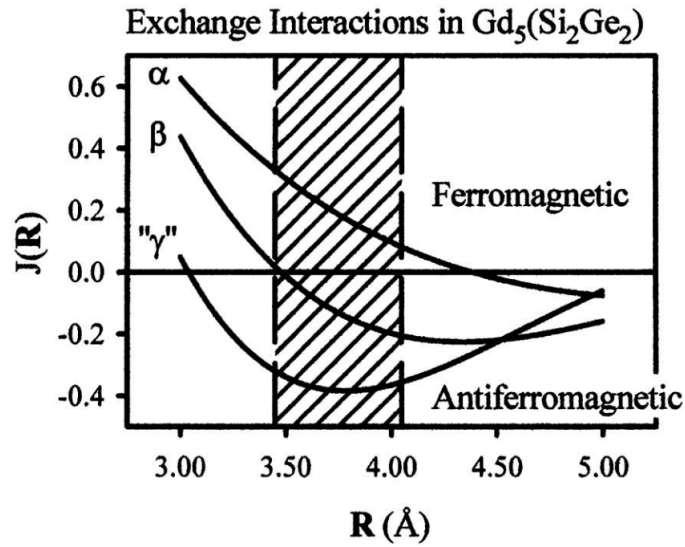
Figure 5.1: *Reproduced from Choe et al.[7], describes the exchange interaction for the orthorhombic and monoclinic phases here named α and β respectively as a function of Gd-Gd site separation.*

The traditional Ising model is a set of rigid sites in an n-dimensional system, each with an associated spin value. In our implementation of the Ising model we have chosen the following Hamiltonian for the system

$$H = -J(R_{ij}) \sum_{<i,j>} S_i S_j - D \sum_i S_i - E_{ext} \sum_i S_i - \Delta E_{bond} \qquad (5.1)$$

where the exchange constant J is calculated using the RKKY model

$$J(R_{ij}) = 9\pi \left(\frac{j^2}{E_f}\right)\left[\frac{2k_f R_{ij} cos(k_f R_{ij}) - sin(k_f R_{ij})}{2k_f R_{ij}^4}\right] \qquad (5.2)$$

The first term in equation 5.1 is the nearest neighbour Ising interaction. The second term is the single-ion anisotropy arising from the crystal field interaction. The third term is the Zeeman effect from an applied external field. The fourth is a constant term introduced to represent a bond energy present in the orthorhombic phase but not in the monoclinic phase. The exchange constant $J(R_{ij})$ quantifies the strength of the coupling between magnetic ions, calculated using equation 5.2. S_i is the spin of site i, N is the number of sites, D is the single-ion anisotropy coefficient, here held as a constant 1 to simplify simulations, and E_{ext} an energy term explaining the effective external field. In equation 5.2, E_f is the Fermi energy, k_f is the Fermi wave vector, and R_{ij} is the distance between sites i and j.

From equation 5.2 through the Fermi energy and wave vector components it can be seen that the main driving factors for the value of $J(R_{ij})$ are the density of carriers and the distance between sites, which are both different in the orthorhombic and monoclinic phases. In addition to modifying the Si/Ge ratio, doping to change the free electron density and straining the crystal structure are two viable options for tuning the Curie temperature.

The average magnetization of the sites is calculated using

$$< M >= \frac{1}{N} \sum_i S_i \qquad (5.3)$$

The magnetic susceptibility, χ, and specific heat, C_ν, are calculated using the equations 5.4 and 5.5

78

$$\chi = \frac{1}{T}[< M^2 > - < M >^2] \tag{5.4}$$

$$C_\nu = \frac{1}{T^2}[< H^2 > - < H >^2] \tag{5.5}$$

Where M is the magnetisation and H the total Energy of a given configuration. Relative Cooling Power (RCP) is a figure of merit for magnetocaloric materials and is calculated using the following equation

$$RCP = \Delta S_{max}.\Delta T_{\frac{1}{2}} \tag{5.6}$$

Where ΔS_{max} is the maximum entropy change value, and $\Delta T_{\frac{1}{2}}$ is the full width half maximum value of the peak in entropy change as a function of temperature. There are several definitions of RCP in the literature. The chosen definition does not account for material with wide $\Delta T_{\frac{1}{2}}$ being unable to fully access this temperature range in an reasonable cycle, but is used in this work to compare simulation to simulation, not to experimental results.

The purpose of this chapter is to investigate the changing site distance, corresponding coupling, and its associated energy. We have simulated a series of three-dimensional arrays of $75 \times 75 \times 75$ sites, in a temperature range of 0 K-400 K and field range of $0\ T$ to $5\ T$. Strain and sample defects are also investigated by changing the site distance in a given dimension strain in that corresponding axis is simulated. Introducing randomly distributed, magnetically null sites at previously Gd sites also simulated a form of defect or site substitution by a non-magnetic material.

All simulation data shown are of a $75 \times 75 \times 75$ sites simulation using $75 \times 75 \times 75 \times N_{MCSteps}$ Monte Carlo steps. A point of convergence for the value of $N_{MCSteps}$ was determined to be optimal at 200, figure 5.2. Figure 5.2 (Right) shows the decreasing phase change temperature point for different values of $N_{MCSteps}$ up to 200 and above, where the phase change no longer decreases in temperature. For

79

this reason, to optimise simulation run time $N_{MCSteps}$ was chosen to be 200 for all simulations.
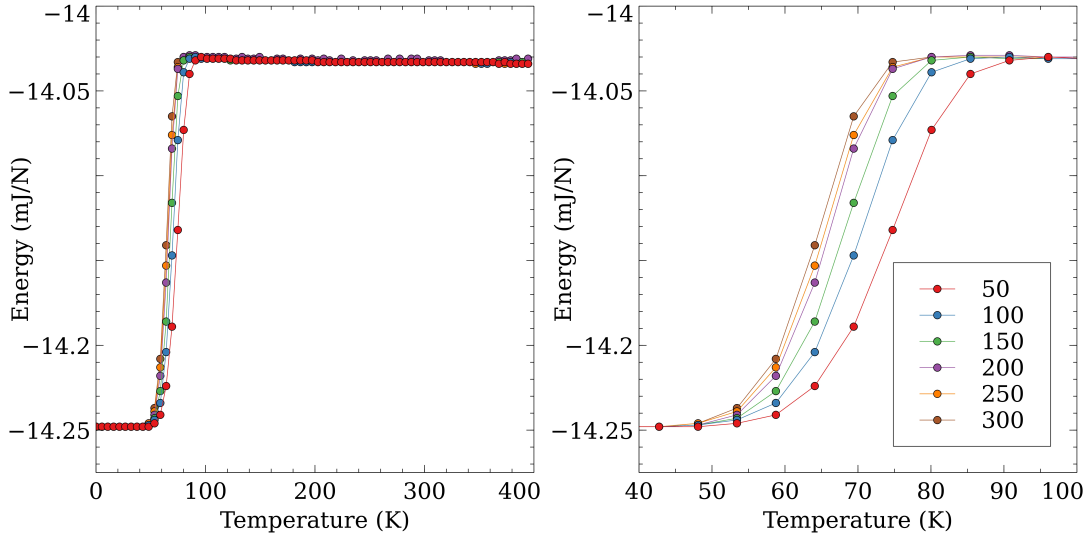
Figure 5.2: *(Left) Multiple Ising simulations energy vs Temperature plots for different values of $N_{MCSteps}$, (Right) The same plot with a focus on the phase change temperature range.*

The simulation produces magnetisation, energy, magnetic susceptibility and coercivity data for both temperature and magnetic field points. After which, indirect measurements techniques and partition functions described in chapter 2 are used to find entropy change data.

5.2 Energy

The orthorhombic and monoclinic phases are simulated concurrently. The lowest H, calculated from equation 5.1, of either phase is considered the favoured. If the two phases are indistinguishable, the monoclinic phase is favoured, and the thermodynamic variables of the non-favoured phase are discarded.

The nature of the simulation changes with $E_{bond} > 3.5$. In this regime, the orthorhombic phase is not indistinguishable from the monoclinic phase. This point

can be taken to be the second-order, high-temperature regime seen experimentally [111] where there is a magnetic SOPT where $Si/Ge > 0.5$.
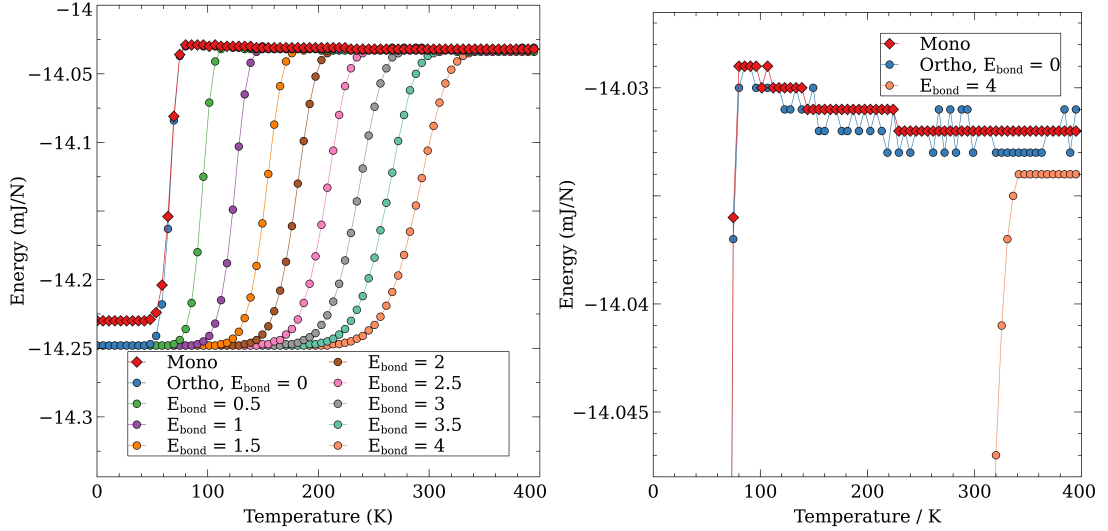
Figure 5.3: *(Left)Energy vs temperature for the monoclinic phase and orthorhombic for $\Delta E_{bond} = 0$ to $\Delta E_{bond} = 4$ in the orthorhombic phase, (Right) Energy vs temperature for the monoclinic phase and orthorhombic at just $\Delta E_{bond} = 0$ and $\Delta E_{bond} = 4$.*

As E_{bond} increases, the average energy per Gd site of the orthorhombic and monoclinic phases become indistinguishable at increasing temperatures, see figure 5.3(Left). From our simulations, the temperature at which the monoclinic phase is energetically favourable (i.e. the phase transition) varies from a temperature of 84 K to 308 K as E_{bond} is increased. Experiments by Pecharsky et al. [111, 112] determined that for Ge-rich samples the phase transition occurs at 125 K, whereas for Si-rich samples the transition occurred at much higher temperatures, close to 310 K, in good agreement with our simulations.

E_{bond} is an S independent term that proportionally affects the phase transition. As the energy of the inter-slab bonds is dependent on the ratio of Si to Ge in $Gd_5(Si_xGe_{1-x})_4$, the temperature at which the phase transition from

81

orthorhombic to monoclinic occurs will increase with increasing x, as observed experimentally [111]. Therefore E_{bond} is proportional to x.
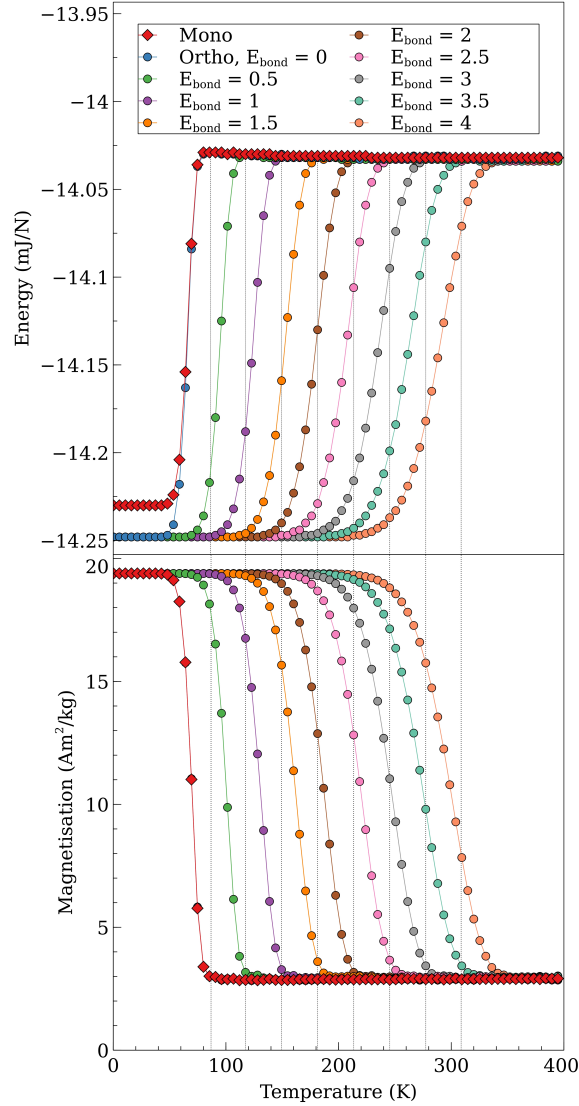
Figure 5.4: *(Top) Bond energy as a function of temperature and (Bottom) the magnetic response of the same system. Horizontal lines indicate the temperatures at which the energy of the phases intersect/become indistinguishable.*

The point at which the energy of the two phases becomes indistinguishable is noted as being towards the end of the magnetic transition in each case, which is

in agreement with the findings of Samolyuk et al. [94]. This Indicates the high temperature monoclinic phase is only preferable when a significant quantity of the crystal is already in a paramagnetic state and the magnetic transition is near its end. This further indicates that the Orthorhombic phase is the dominant phase for the majority of the transition region and that the structural and magnetic transitions are connected but do not occur concurrently, with a delayed structural change occurring after the system is majority paramagnetic with an increasing temperature.

Also notable during the transition region is the decreasing gradient in both the magnetic and energy plots for an increasing E_{bond}. This shows a tendency towards a larger ΔT and more SOPT like system for both orthorhombic and monoclinic systems as E_{bond} is increased were the structural systems to be remain constant.

5.3 Magnetism

Figure 5.4 shows both the magnetism and energy relationships with temperature. Horizontal lines have been drawn to show the point at which the energy of the two systems is indistinguishable. Where $0 \leq E_{bond} \leq 3$, the energy of the two phases become indistinguishable at temperatures below the paramagnetic state. As the structural phase transition occurs mid-magnetic transition, the simulation has an abrupt magnetic change which experimentally drives the phase transition to be FOPT.

The magnetic moment vs field plot in figure 5.4 bottom shows the decrease in moment and change from a ferro- to para-magnetic state as the temperature increases. Experimentally the monoclinic phase is only found in a paramagnetic state [111], indicating values of $E_{bond} < 0$ are non-physical, as this would cause a structural phase transition from ferromagnetic orthorhombic to ferromagnetic monoclinic and a second magnetic transition, at a higher temperature, from fer-

romanetic to paramagnetic monoclinic phase. If $E_{bond} \geq 0$, a monoclinic system always magnetically transitions before the orthorhombic. By comparison to reported results [111] $E_{bond} = 0$ represents a bonding energy equivalent to $x = 0.24$ and $E_{bond} \geq 3.5$ represents a bonding energy equivalent to $x \geq 0.5$.

The lower limit is therefore $E_{bond} = 0$, along with an upper limit found at $E_{bond} = 3.5$; for the FOPT region of $Gd_5(Si_xGe_{1-x})_4$.

Figure 5.5 shows the magnetic data from the monoclinic phase at low temperatures and orthorhombic at high temperatures, where the data source is changed about the T_c determined from figure 5.4. Data shown is for $E_{bond} = 0.5$. Magnetic data, as a function of field, show a transition from ferromagnetic to paramagnetic, figure 5.5, with a noticeable gap at the transition temperature between 125 K and 133 K.

The experimentally observed hysteresis losses for GSG about the transition point are much larger than those observed in the simulation, with Provenzano et al. showing a gap of $\approx 0.5\ T$ [55], simulations show a gap of $\approx 0.1\ T$.
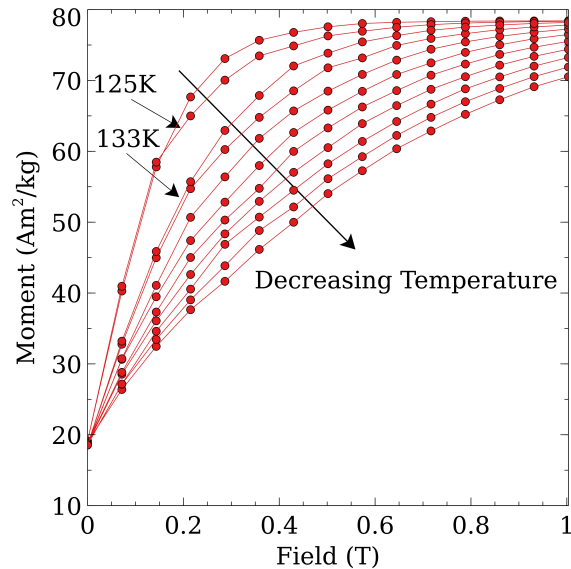
Figure 5.5: *Moment as a function of field for $E_{bond} = 0.5$, monoclinic and orthorhombic phase data is present.*

5.4   Entropy, Specific Heat and Susceptibility

In our simulations, we calculate the total energy and spin state of the monoclinic and orthorhombic structures at each temperature and field. We then select the spin state of the favoured energy structure to represent the magnetism at each temperature and field. Figure 5.6 shows the entropy change as a function of temperature calculated from equation 1 using values from 0 T to 5 T for external fields. There is a decrease in the peak entropy change as E_{bond} increases, indicating an increasing Si content in $Gd_5(Si_xGe_{1-x})_4$ will reduce its effectiveness as a cooling material; this is evident in experimental results [5]. The peaks also broaden in their temperature range. Figure 5.6 also shows the effect an increased external field has on the entropy change, with a higher magnetic field pushing the transition temperature to slightly lower temperatures and increasing the total entropy change, as expected from experimental results [5].

Figure 5.7 plots the specific heat as a function of temperature for different values in the orthorhombic and monoclinic phases. For a theoretical FOPT, the change in specific heat as a function of temperature would be expected to be a δ function at the critical temperature [113]. Lower values have a peak in the specific heat at lower temperatures, but also show a narrower peak. This indicates at low temperatures our model predicts a FOPT, at higher temperatures it predicts FOPT with a broadening ΔT until $E_{bond} = 4$ at which point it is firmly within the SOPT regime. The specific heat as a function of temperature (Figure 5.7) indicates a gradual change from FOPT to SOPT as E bond is increased, figure 5.7 (Right) indicates a change from FOPT to SOPT at $E_{bond} > 3.5$ with a peak broadening from lower to higher temperatures.
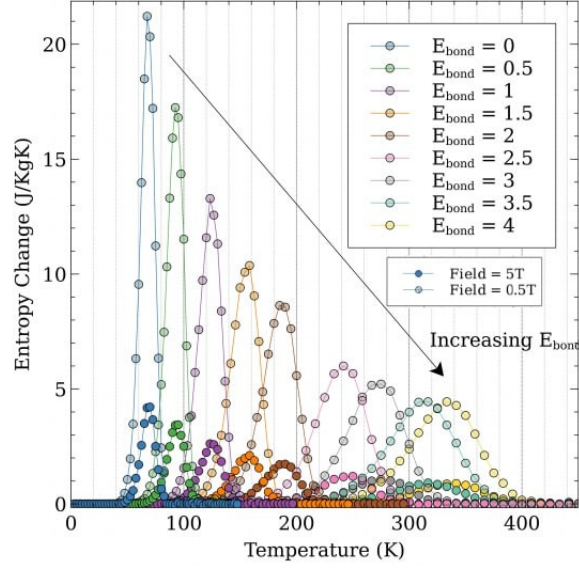
Figure 5.6: *Entropy change for various E_{bond} values up to 0.5 T and 5 T, closed and open points respectively.*

Following the method described by W. Janke [44], the critical exponent ν and γ can be found using the critical exponent relationships described in equations 5.7 and 5.8

$$\frac{|T - T_c|}{T_c} \approx \zeta^{\frac{1}{\nu}} \tag{5.7}$$

$$\frac{|T - T_c|}{T_c} \approx \chi^{\frac{1}{\gamma}} \tag{5.8}$$

Where ζ is the relaxation length. Then using the Josephsons [114, 115] and Rushbrookes [116] laws described in equations 5.9 and 5.10 respectively further values for α and exponents can be found

$$D\nu = 2 - \alpha \tag{5.9}$$

$$2\beta + \gamma = 2 - \alpha \tag{5.10}$$

Where D is the dimensionality of the model. For the model described in this chapter the critical exponents for $E_{bond} = 0$ were found to be; $\nu = 0.71 \pm 0.12$, $\alpha = 0.13 \pm 0.36$, $= 0.34 \pm 0.41$ and $\gamma = 1.19 \pm 0.2$. The critical exponents can be further expressed in terms of the local operators $\sigma, \epsilon, \epsilon'$ scaling dimensions by using the relationships described in equations 5.11 and 5.12

$$\nu = 1/(D - \Delta_\epsilon) \tag{5.11}$$

$$\gamma = \frac{D - 2\Delta_\sigma}{D - \Delta_\epsilon} \tag{5.12}$$

Using the above critical exponents Δ_ϵ and Δ_σ were found to be 1.59 ± 0.20 and 0.66105 ± 0.12 respectively. Comparing the results to those of Kos et al. [117], who found the Δ_ϵ and Δ_σ would be 1.412625 and 0.5181489 respectively for a 3-dimensional model, shows good agreement with our findings. A 2-dimensional models Δ_ϵ and Δ_σ can be found to be 1 and 1/8 exactly, and a 4-dimensional models Δ_ϵ and Δ_σ can be found to be 2 and 1 exactly for comparison.

RCP is calculated using equation 5.6, and results shown in figure 5.8. A decrease in the cooling power of the system as it approaches a higher critical temperature regime can be seen. This decrease indicates that the Si ratio is inversely related to the cooling efficiency of the $Gd_5(Si_xGe_{1-x})_4$ structure.

Figure 5.7 (right) shows the susceptibility as a function of the temperature of the same systems. Again, a narrowing peak appears as E_{bond} decreases. However, in this case the peak also increases.
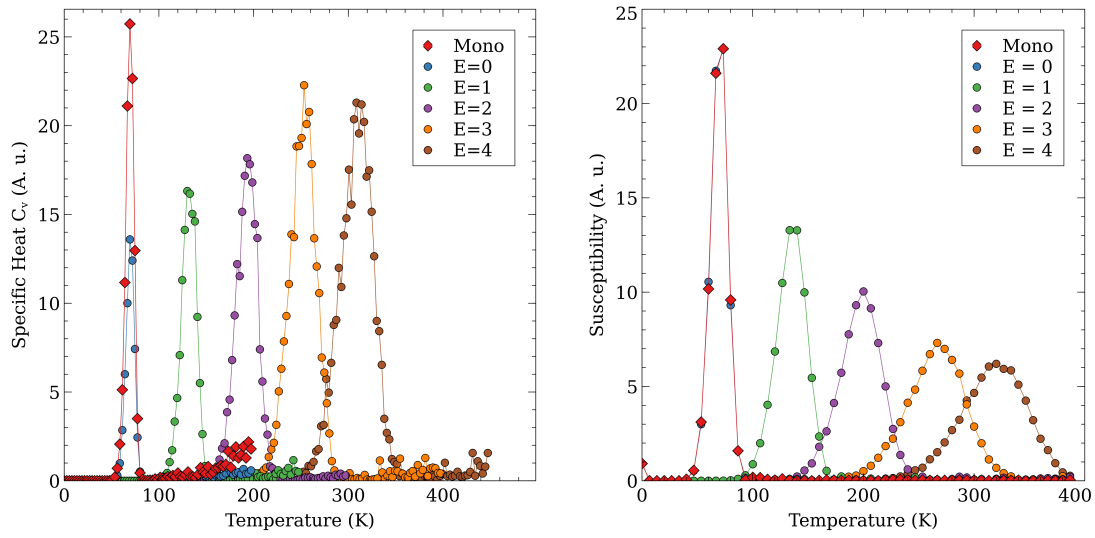
Figure 5.7: *Specific Heat (Left) and Susceptibility (Right) at 0 T for increasing E_{bond} values.*
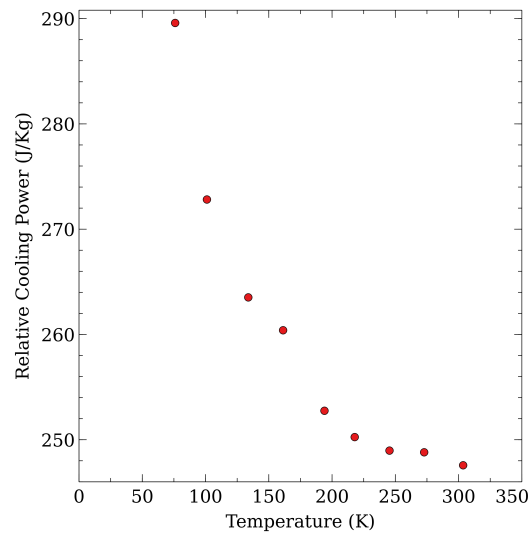
Figure 5.8: *RCP calculated for various values of E_{bond} and plotted against the peak temperature position.*

5.5 Stress/Strain Effects

As with many MC materials, $Gd_5(Si_xGe_{1-x})_4$ experiences a change in its MCE when under applied pressure. Stress and strain have been introduced by increasing or decreasing the distance between magnetic sites in $Gd_5(Si_xGe_{1-x})_4$.

As strain can be induced in multiple directions, the simulations focus on each axis individually. Figure 3.3 shows the $Gd_5(Si_xGe_{1-x})_4$ structure, where the a-axis runs horizontally, the b axis vertically and the c axis in the plane of the image. Figure 5.9 shows the effects of stress and strain on both the orthorhombic and monoclinic phases for the a, b and c axis. For both phases, the effects are far more pronounced in the ferromagnetic, low-temperature regime, with the orthorhombic simulations having a more significant change in total energy compared to the monoclinic phase.

The critical temperature is also changed with strain with a -10% strain causing an increase of up to 13 K in the a-axis, 10 K in the b-axis and 7 K in the c-axis. Similar but reduced increases are also seen for -5%, -2% and -1% and an opposite negative relationship of T_c for positive strains. This suggests that the choice of strain level and axis can be used to alter the T_c as well as the Si/Ge ratio. This agrees with bulk studies, showing a change in T_c when a strain is applied [118, 119, 120]. A change in R of -10% in the a axis is equivalent to a 6.3% change in E_f in the monoclinic phase but a 7.4% in the orthorhombic phase. This difference of change in E_f between the phases also increases the point at which the two phases become indistinguishable. This indicates the strain relationship in $Gd_5(Si_xGe_{1-x})_4$ with the MCE is partly driven by the change in RKKY exchange coupling $J(R)$. The gradient across the transition region is also altered during straining, with a negative strain increasing the T_c but decreasing the gradient. This shows that even with the increase in T_c being attributed to strain and not the Si/Ge ratio, the tendency towards a SOPT like transition at increasing temperatures is still maintained.
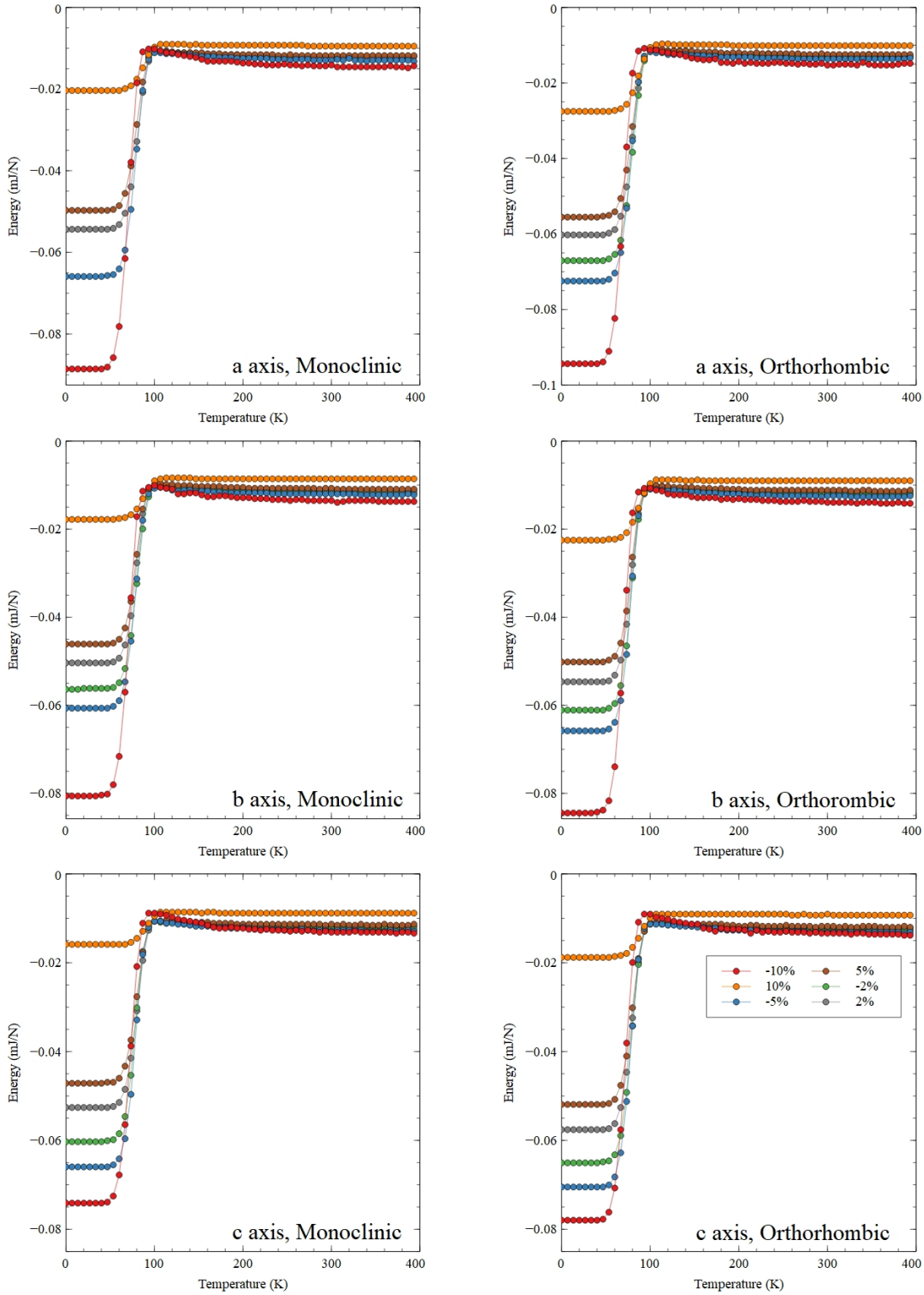
Figure 5.9: *Stress and strain calculations for the a, b and c axis of the $Gd_5(Si_xGe_{1-x})_4$ system for both orthorhombic and monoclinic phases.*

90

5.6 Purity Effects

Simulations presented so far have a 100% purity, meaning the Gd and Si/Ge sites are 100% populated by Gd and Si or Ge respectively. This is rarely the case for real MC samples, with most having imperfections and some site replacement present that can alter the structure, magnetism or stress/strain within the material. To investigate these effects simulations have been run with Gd sites, the magnetic component of $Gd_5(Si_xGe_{1-x})_4$, being replaced randomly.
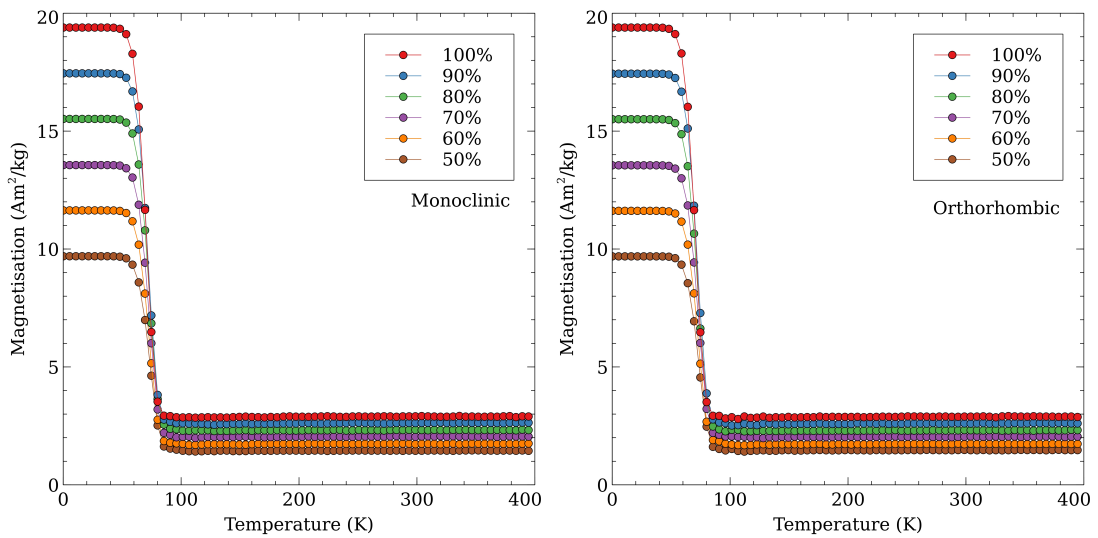
Figure 5.10: *Purity measurements for $E_{bond} = 0$ for both monoclinic and orthorhombic phases as a function of temperature.*

Replacing the Gd sites for the Ising simulations, much like the strain investigations has little effect on the T_c. It does, however, decrease the magnetisation of the sample at temperatures both above and below the T_c. This decrease in magnetisation also causes a decrease in the MCE, which is a detriment to the usefulness of the sample as an MC material.

5.7 Summary

An Ising model combined with the RKKY coupling mechanism has been employed to determine a phase change temperature range for a $Gd_5(Si_xGe_{1-x})_4$ structure. This model shows the applicability of Ising like models for energy comparison in first-order phase transitions of rare-earth-based magnetocaloric materials when comparing the total energy of several phases. The model also shows the effects of stress/strain and purity within the sample, with neither affecting the T_c, but having an effect on the total energy in the system and magnetisation.

This model has wide-ranging applicability and is not just for materials where the RKKY is the dominant exchange mechanism. It is possible to investigate simulations beyond rare-earth-based FOPT materials with this energy comparison method, given an appropriate coupling mechanism choice.

5.7.1 Future Potential

The comparison of multiple phases during a Monte Carlo simulation has been deployed here to investigate $Gd_5(Si_xGe_{1-x})_4$. However, the method can be used for other rare earth, and non-rare earth materials provided the MCE is not driven or mainly driven by itinerant electrons. The price of rare earth materials and the necessary quantities needed to produce bulk MC materials makes the phase comparison method appealing for investigating new compounds and materials before having to commit to purchasing materials.

The simulations used had uniform material throughout, with a random distribution of magnetically null sites for purity investigations. Future investigations could look into a non-random distribution of magnetic sites or non-uniform distribution of the value of E_{bond}. As the FOPT of $Gd_5(Si_xGe_{1-x})_4$ is known to display a breaking in a super-exchange between slabs in the material, further investigation could also include analysis of this super-exchange and its effect.

<div style="text-align: right">6</div>

Magnetocaloric Thin Film $Gd_5Si_2Ge_2$

6.1 Introduction

This chapter will describe the preparation and characterisation of magnetocaloric $Gd_5Si_2Ge_2$ thin films. All films are grown from the same $Gd_5Si_2Ge_2$ target using PLD on both AlN and Si/SiO_2 substrates. Magnetometry is performed using a mixture of SQUID and VSM. Both isothermal and isofield measurements are conducted to determine magnetic phase transitions and associated thermodynamic properties. The topography is investigated using an AFM with a particular interest in the grain sizes, surface roughness and film thickness. The structural investigation is performed using XRR, XRD and PNR, to investigate the inter-

ference of the sample structure on its magnetic properties caused by the substrate, film and interface.

6.2 $Gd_5Si_2Ge_2$ description

$Gd_5(Si_xGe_{1-x})_4$ was chosen as a material to investigate as a thin film for multiple reasons; it is widely studied already as a bulk and powder material, it has a room temperature phase transition and has previously been successfully grown using PLD to a thickness of $\approx 1\mu$m, starting with a homogeneous target and deposition temperatures close to 673K [121].
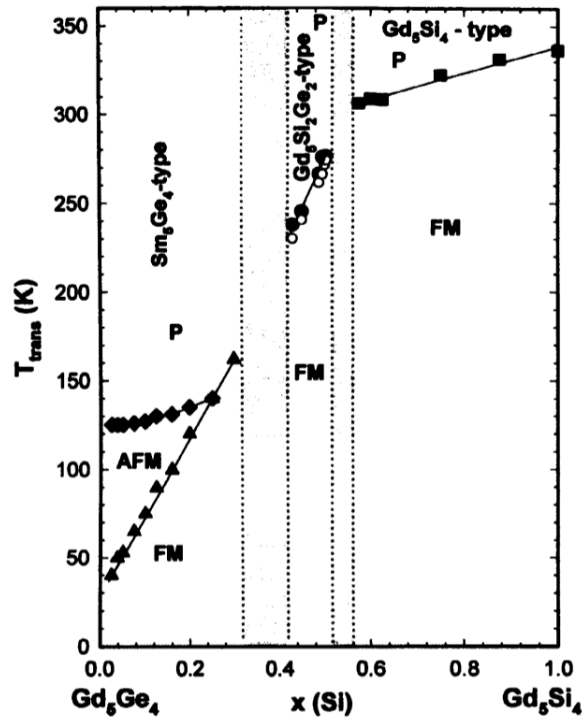
Figure 6.1: *Phase diagram of GdSiGe, the central region contains the first order regime [8].*

The phase diagram of $Gd_5(Si_xGe_{1-x})_4$, figure 6.1, shows an operating temperature of $\sim 125\ K$ to $\sim 310\ K$ for a FOPT. The upper end of this range, $x = 0.5$,

is where a target was chosen with a constituency of $Gd_5Si_2Ge_2$ and produced by American Elements PLC.

6.3 Growth

When growing thin-film materials via PLD, there are many growth parameters to consider; substrate choice, substrate temperature, laser fluence, laser frequency, chamber pressure, chamber gas constituents, target material and condition or duration. Any of these can have drastic effects on the final sample.

Bulk $Gd_5Si_2Ge_2$ phase and crystal structure are highly dependent on the purity of the starting materials, growth temperatures and post-growth heat treatment, where high purity ($>$ 99.5%) materials vastly improve performance as does post growth annealing that can be on the time scale of days [3]. As the target material used is already of high purity (99.95%), the temperature treatment of the deposited film will be the main concern for investigation. Also shown is an investigation into chamber pressure, substrate choice and laser fluence.

Figure 6.2 describes the ratio of orthorhombic phase in $Gd_5Si_2Ge_2$ as a function of heating and cooling of bulk $Gd_5Si_2Ge_2$. As the monoclinic phase is found exclusively in the FOPT regime, ensuring its presence during deposition is crucial. The levels of monoclinic present increases up to 573 K, and at 593 K it drastically reduces to $<$ 90% and completely disappears at higher temperatures. Samples were therefore deposit in a range of 293 K to 723 K with the majority of samples in the range 523 K to 573 K.
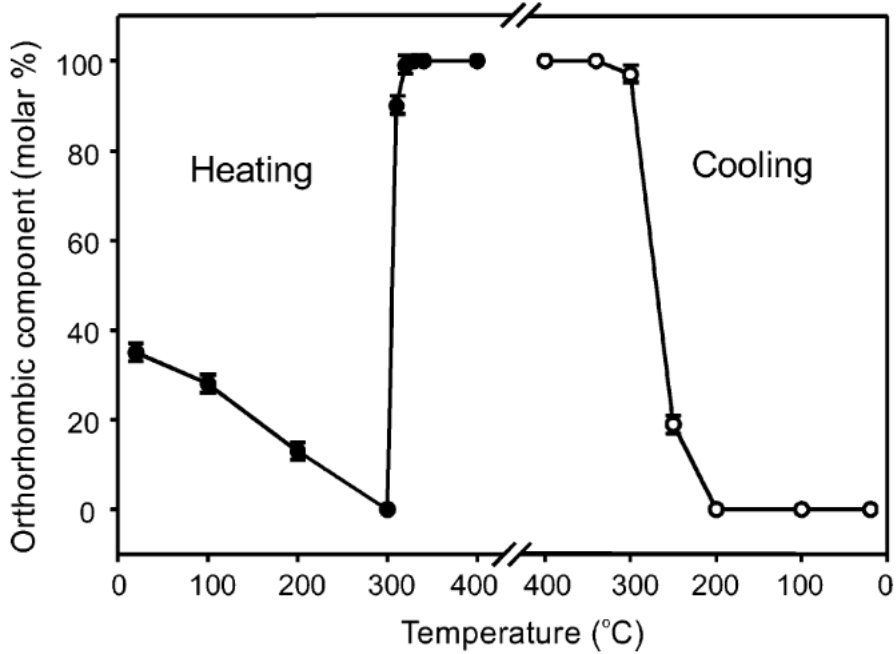
Figure 6.2: *Proportion of orthorhombic phase as a function of temperature during heating and cooling of bulk $Gd_5Si_2Ge_2$ [9].*

PLD relies upon the absorption of the laser by the target and breaking of the structure to successfully form a material plume. $Gd_5Si_2Ge_2$ has metallic-like properties, reflecting a lot of the incoming laser energy, the material, therefore requires a high level of energy to form plumes. Laser fluences of 8 J/cm^2 to 12.73 J/cm^2 are possible, however fluences below 9.55 J/cm^2 result in no plume forming, so results for fluences of 9.55 J/cm^2 and above are shown from here on. A laser frequency of 18Hz is chosen for all depositions.

Several chamber pressures are used for the deposition; $\sim 7 \ \mu Torr$, the lowest possible in this PLD system with laser on and material ablating, up to 20 mTorr, maximum allowed in PLD chamber while depositing. For all depositions the chamber is first evacuated and allowed to reach a minimum of $\sim 7 \ \mu Torr$ for 1 hour, before Ar gas is used to reach the desired pressure. All samples are allowed to cool back to room temperature for 1 hour before being removed from

the chamber. All depositions are for 1 hour unless otherwise stated.

Si/SiO_2 was chosen to provide a diffusion barrier between the deposited material and the Si substrate. Sambandan et al. showed that deposited $Gd_5(Si_xGe_{1-x})_4$ on Si and Si_3N_4 substrate created a diffusion layer with small amount of $Gd_5(Si_x Ge_{1-x})_4$ but also containing $GdSi_2$ [104]. Sambandan et al. suggest a Si/SiO_2 as an alternative. AlN substrate is also used due to its high thermal conductivity, a desirable property for industrial applications.

6.4   Surface

The PLD process causes plumes of material to accumulate on the substrate as described previously 4.3. The nature of this deposition technique can produce a differing material surface, from extremely flat to highly granular, dependant upon many variables [102].

In this section, the roughness and grain-size are used to investigate the deposition of $Gd_5(Si_xGe_{1-x})_4$ with varying chamber parameters and compare them to magnetic data.

6.4.1   Roughness

Roughness is calculated using the root mean square method

$$R = \sqrt{\frac{1}{n} \sum_{i=j=1}^{n} y_{i,j}^2} \tag{6.1}$$

Where R is the root mean square roughness, n the number of points in image, i, j are the ith and j^{th} index in the image and $y_{i,j}$ the height at index i, j.

Grain-size is calculated using the average area of the grains visible at the surface from AFM images, see figure 6.3 (left). A program has been written to analyse the surface images to produce the average grain-size and images similar

to that in figure 6.3 (right). The edges of the grains are defined using a change in gradient and can be described as

$$
G(x,y) = \begin{cases} true, & where \quad \pm\,\Delta(x,y) \cdot \pm\Delta(x-1,y) = \mp A \\ true, & where \quad \pm\,\Delta(x,y) \cdot \pm\Delta(x,y-1) = \mp A \\ false, & where \quad \pm\,\Delta(x,y) \cdot \pm\Delta(x,y-1) = \pm A \end{cases} \tag{6.2}
$$

Where G is a binary value on an x, y grid of the same length and width as the image, $\Delta(x,y)$ is the gradient at point (x,y), $\Delta(x-1,y)$ and $\Delta(x,y-1)$ are the gradients of neighbouring points to (x,y) and A is the product of neighbouring gradients.

Equation 6.2 therefore uses the change in sign of a gradient to decide where one grain ends and another begins in an (x,y) plane.
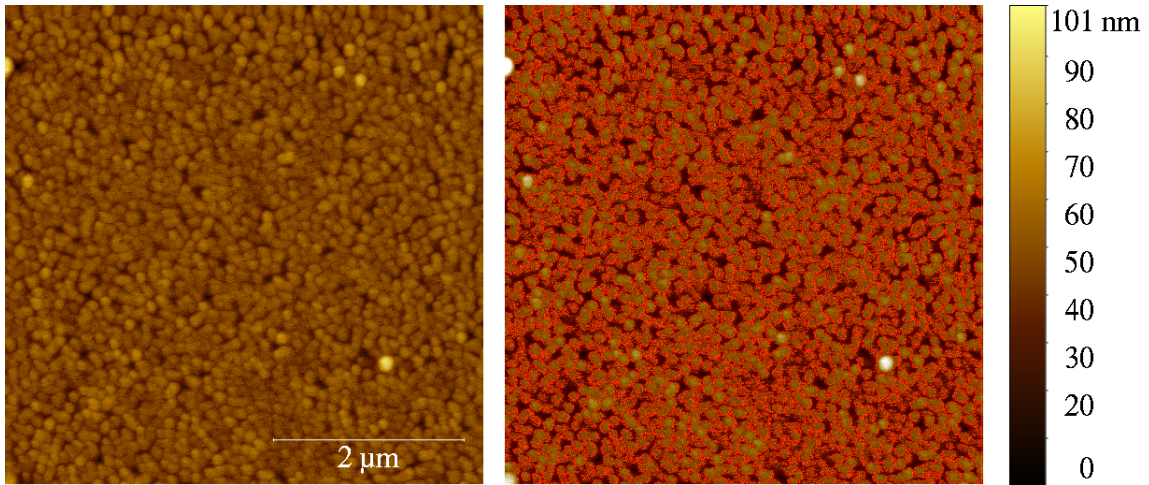
Figure 6.3: *(Left) Corrected data of a 5×5 μm area GdSiGe thin film surface. (Right) The same surface with grains highlighted.*

There is a significant difference in roughness found for samples grown on AlN and Si/SiO_2 substrates. Figure 6.3 (left) shows an order of magnitude increase in roughness for AlN substrate samples over Si/SiO_2 samples. Figure

6.3(right) is the roughness measurements of Si/SiO_2 substrates only as a function of deposition temperature.

Measurements of both substrate materials before deposition show this same order of magnitude difference, with the Si/SiO_2 substrate roughness at 2.93 $nm \pm$ 0.3 nm and the AlN roughness at 302 $nm \pm 20$ nm. This order difference would account for the difference seen post-deposition. Despite the high roughness of AlN it is still a viable material, as will be discussed in section 6.5.
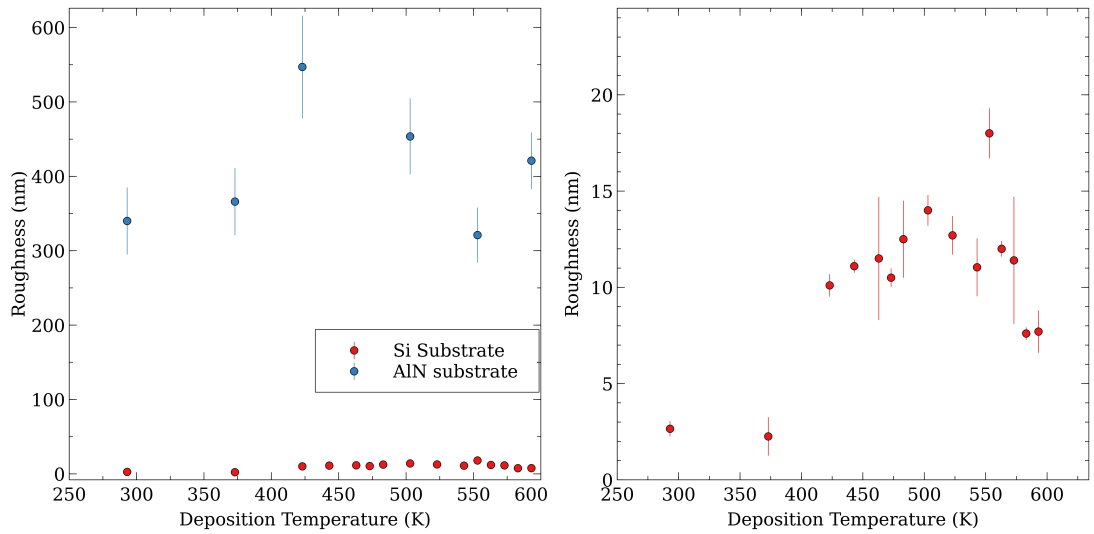
Figure 6.4: *(left) Roughness measurements of GdSiGe thin films as a function of their deposition temperature, (right) Roughness measurements of GdSiGe thin film on Si/SiO_2 only.*

Figure 6.4 (right) is a plot of just the Si substrate samples roughness against deposition temperature; this plot shows an increase in the roughness with the deposition temperature up to a temperature point. There is then a change in the roughness relationship with the temperature close to the temperature at which the orthorhombic phase comes to dominate as described in figure 6.2.

There is an increase from 2.6 $nm \pm 0.4$ nm to 17.9 $nm \pm 1.3$ nm in the roughness with increasing deposition temperature from 293 K up to 553 K for

Si/SiO_2 substrate samples, where the roughness sharply decreases above $553\ K$. The ratio of orthorhombic to monoclinic, figure 6.2, has a similar relationship with temperature up to $573\ K$ with an abrupt change at temperatures above. The surface roughness measurements would suggest that even though decreased levels of the orthorhombic phase during deposition are theoretically advantageous for the magnetocaloric effect, it will also increase the surface roughness of the samples.

6.4.2   Grain Size

The average grain size of the Si substrate samples show a similar change with the deposition temperature relationship to those in figure 6.4 (right). The average grain size of the $Gd_5Si_2Ge_2$ samples have a linear decrease from $293\ K$ to $553\ K$. At temperatures higher than the temperature at which the orthorhombic phase comes to dominate as described in figure 6.2 of $Gd_5Si_2Ge_2$, the roughness and grain size sharply drops with deposition temperature, figure 6.5.

Deposition of $Gd_5Si_2Ge_2$ on Si_SiO_2 substrates at temperatures close to but below the temperature at which the orthorhombic phase comes to dominate as described in figure 6.2, therefore, form rougher surfaces with smaller grains. The sudden change in the surface above the T_c is likely related to the lack of the magnetocaloric effect above $573\ K$ discussed in section 6.5.

AlN substrates do not have the same relationship with deposition temperature that Si/SiO_2 does. Despite this, the magnetocaloric effect is still present below $573\ K$ and no longer appears above. The rough nature of the AlN substrates pre-deposition may be obfuscating the temperature relationship, however.

The distinct roughness/grain-size regimes in figure 6.6 indicate the roughness and grain size of PLD deposited $Gd_5Si_2Ge_2$ is predominantly driven by choice of substrate. The deposition temperature also has an effect that is unfavourable close to the T_c.

Si/SiO_2 substrate samples deposited close to the temperature at which the orthorhombic phase comes to dominate as described in figure 6.2, 553 K, have a grain-size $\sim 120\ nm^2$ and roughness $\sim 12\ nm$.
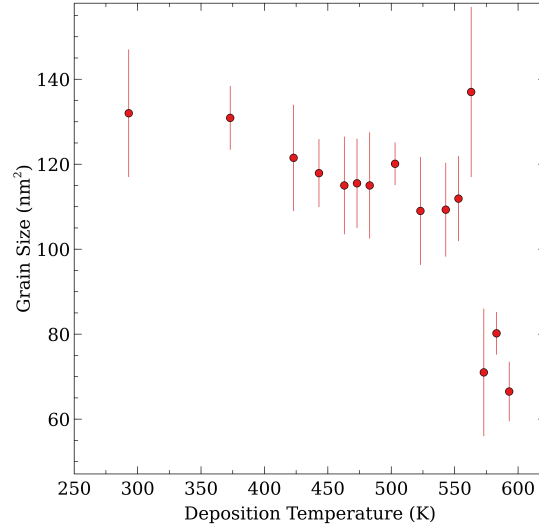
Figure 6.5: *Grain Size measurements of $Gd_5Si_2Ge_2$ on $Si_{si}O_2$ thin films as a function of their deposition temperature.*
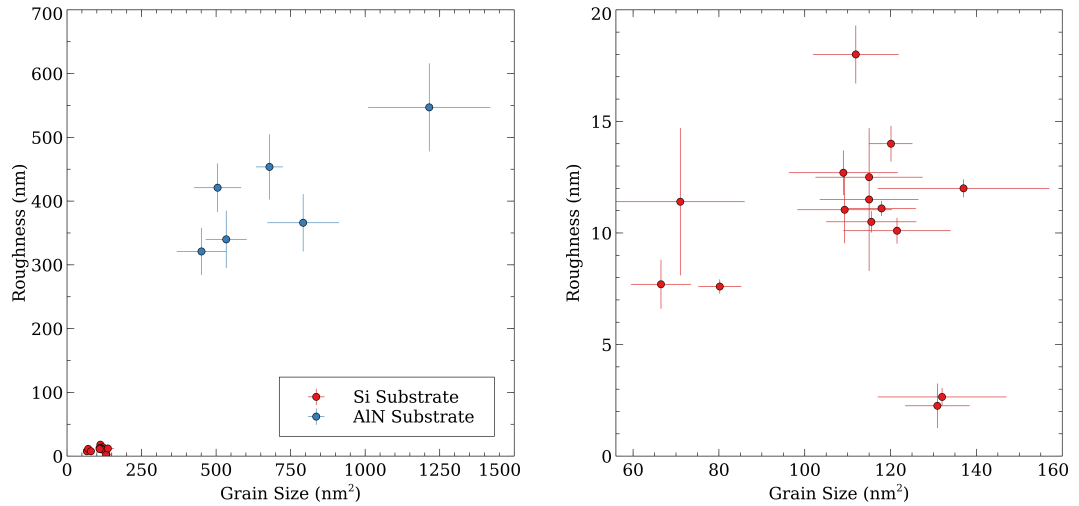
Figure 6.6: *(left) Grain Size measurements of GdSiGe thin films as a function of their surface roughness, (right) Grain Size measurements of GdSiGe thin films as a function of their surface roughness on Si/SiO_2 only.*

6.4.3 Thickness
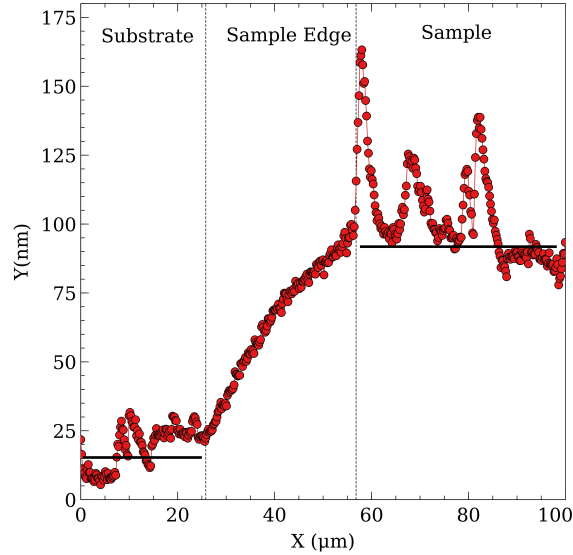
Figure 6.7: *Thickness profile, measured using AFM, of a GdSiGe thin film sample deposited at 293 K on Si/SiO$_2$.*

There is little change in thickness with deposition temperature or substrate material of $Gd_5Si_2Ge_2$, with all samples being in the thickness range of 80 nm to 110 nm for deposition chamber pressures of 20 mTorr Ar. All samples were grown for 1 hour using a laser frequency of 18 Hz for consistency. For samples grown at the lowest possible chamber pressure capable in the PLD, the thickness does increase to the range of 120 nm to 150 nm. A square mask is used during deposition to give an edge to the samples and leave some substrate exposed for thickness measurements. These edges are not sharp however, figure 6.7 shows one of the thinner samples grown at 293 K with a slope on the edge that extends ~ 30 μm labelled Sample Edge. Figure 6.7 is a profile image measured using an AFM over the sample edge. All errors are calculated using several points along the edge of the sample and the substrate is assumed to be flat for corrections during data analysis.

6.5 Magnetism

Magnetic measurements were performed using a mixture of 3 SQUID magnetometers and a VSM system. As described in chapter 4 of the 3 SQUID magnetometers, 2 are the same model described in chapter 4 while the third is from the same manufacturer but is only capable of fields up to 5 T. Both M vs H loops with a virgin magnetic curve and M vs T sweeps are performed to identify and quantify the magnetic phase changes in our samples. Direct isothermal magnetic measurements are then used to indirectly calculate the magnetic entropy change ΔS of the system.

6.5.1 Isofield

Due to the different response to an external magnetic field for different magnetic phases, measuring a magnetic moment as a function of temperature while under a small field is an effective means to identify the critical temperature of a magnetic phase transition.

A plot of magnetisation vs temperature is shown in figure 6.8 (left) showing a characteristic gradient change indicative of a magnetic phase transition from a low-temperature ferromagnetic state to a high-temperature paramagnetic state. Given the previously stated thickness and density of $Gd_5Si_2Ge_2$ as 7700 kgm^{-3}, from Gscheider et al. [26], the magnetisation can be shown in units of Am^2kg^{-1}. When compared to bulk material, the magnetisation above the transition point is an order of magnitude smaller, at 0.8 $Am^2kg^{-1} \pm 0.05$ Am^2kg^{-1} vs 53 Am^2kg^{-1} [8].
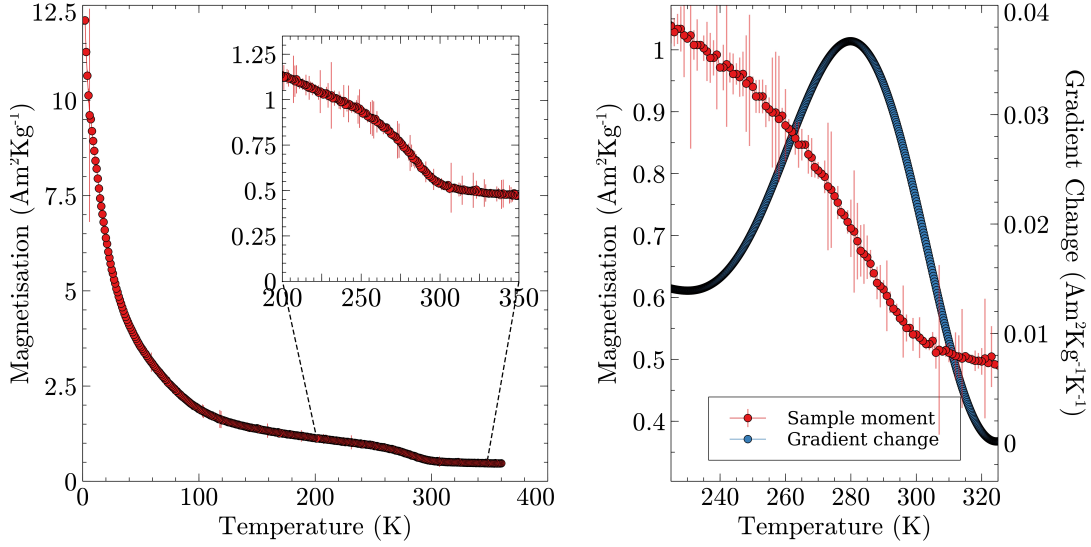
Figure 6.8: *(left) Isofield measurement of a Si/SiO_2 sample grown at 423 K, isofield measurements are taken in a constant field of 200 mT with inset of temperature range of interest, (right) The same temperature range of interest showing magnetisation, M, and gradient change dM/dT.*

Figure 6.8 (Right) includes a plot of the gradient change over the magnetic transition, indicating a peak at 280 K, $\sim 7\ K$ higher than the transition point of the target used for growth and expected T_c of the sample. Hadimani et al. found a similar result for 800 nm thick samples of $Gd_5Si_{1.3}Ge_{2.7}$, where a $\sim 13\ K$ increase in the T_c compared to the bulk was caused primarily by the substrate strain-induced sample pressure increase [5]. Further pressure is introduced from the size of the grains forming the sample, with most samples having a grain diameter of $\sim 120\ nm \pm 20\ nm$ on Si which will introduce a surface pressure of $\sim 30\ KPa \pm 5\ KPa$ [122].

From Pecharsky et al. [8] the magnetisation of $Gd_5Si_2Ge_2$ in the high-temperature paramagnetic state, while under a 200 mT field is 0.3 $\mu Am^2kg \pm$ 0.05 μAm^2kg. The excess magnetisation seen in figure 6.8 (Right) for a sample in 200 mT would suggest that there are other magnetic sources, including secondary

phases. The divergence seen at low temperatures is due to the sample substrate. The high energy nature of PLD deposition may cause other compositions and crystallographic phases to exist that lead to this additional source of magnetism and is further discussed in section 6.6.

The gradient change peak width of $\sim 50K$ can be taken as an intermediate region where neither the high or low-temperature magnetic phases completely dominate. Instead, both magnetic phases coexist, transitioning from one to another through the transition at small domains within the samples. Pecharsky et al. show a smaller but similar scale temperature region for the intermediate-range for $Gd_5Si_{0.45}Ge_{0.55}$ at $\sim 35\ K$ from $\sim 230\ K$ to $\sim 265\ K$, concluding it is a FOPT type transition with a T_c of 240 K [8].

The increase in T_c for thin-film $Gd_5Si_2Ge_2$ can be seen in samples deposited in the temp range 293 K to 553 K, the lowest possible using the PLD system and the upper limit determined previously respectively. For temperatures above 553 K there is no gradient change seen. Figure 6.9 shows samples grown at 293 K and 553 K, the lowest possible and determined upper limit as well as two other intermediate depositions.

The previously mentioned sample internal pressure-grain diameter dependence may be affecting the level of increase in the T_c for the thin film $Gd_5Si_2Ge_2$ samples. The sample grown at 293 K has an average grain size of 132 $\pm 15\ nm$ and the highest T_c of 286.3 K. The sample grown at 553 K has an average grain size of $111.9 \pm 10\ nm$ and a T_c of 281.9 K. The relationship is also seen with samples grown on AlN substrates, with the AlN sample grown at 293 K having an average grain size of $534 \pm 79\ nm$ and the sample grown at 553 K having an average grain size of $499 \pm 83\ nm$.
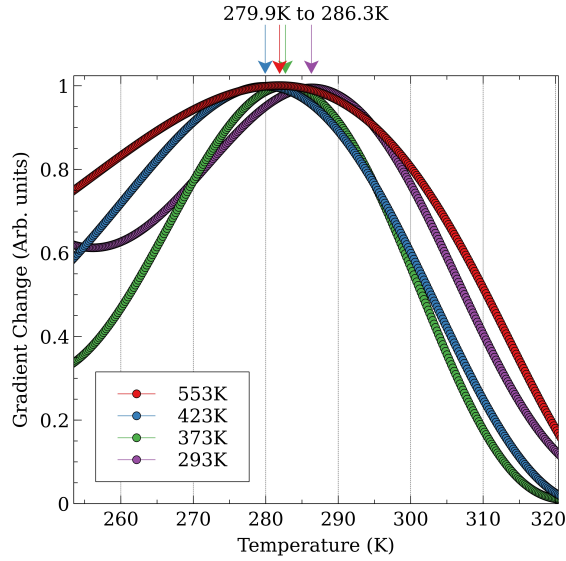
Figure 6.9: *Gradient change of several samples, normalised for comparison and indicating the peak position for a given deposition temperature at the top.*

Pecharsky et al. showed a linear relationship with pressure for $Gd_5Si_2Ge_2$ and T_c [123]. Vollath however, shows an inverse relationship between the grain diameter and the internal pressure [122]. This would disagree with the grain size to T_c relationship shown above, which does not appear to be inverse. If our thin films did follow Vollaths conclusion, a higher T_c would be expected for the sample grown at 553 K, not the sample grown at 293 K. This is assuming the grain diameter is the only source of pressure within the sample however, further pressure could be induced through the substrate and requires further investigation.

6.5.2 Isothermal

After identifying the gradient change region, several temperature points are chosen for isothermal MvsH loops with a particular interest in the virgin curve. To ensure correct analysis of the MCE, the process laid out by Lyubina et al. is used [32], where after each isothermal measurement is taken the sample is heated

106

or cooled well above or below the T_c for decreasing or increasing temperature measurements. Isothermal measurements are not taken uniformly. Figure 6.10 shows a standard choice of temperature points chosen for measurement about the T_c. There are also sparse measurements at lower temperatures down to 2 K.
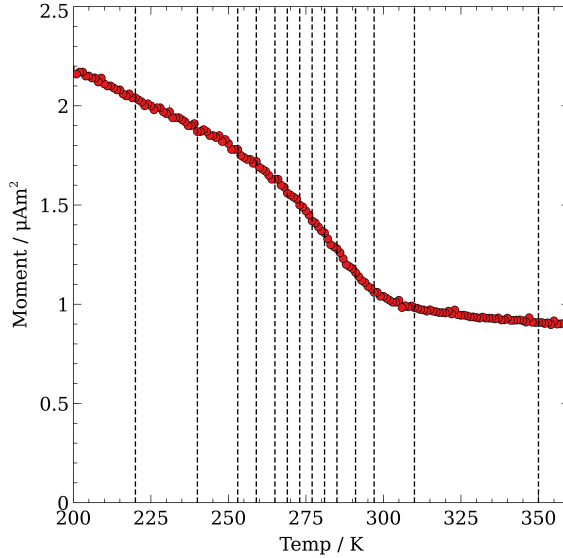
Figure 6.10: *Example temperatures chosen for isothermal measurements. Isofield data is shown and vertical dashed lines used to indicate the temperatures at which isothermal measurements are taken.*

As the thin film $Gd_5Si_2Ge_2$ cannot be separated from the substrate, the raw SQUID data shown in figure 6.11 (left) contains the magnetic moment for both the thin film sample and the substrate. To correct for this, blank Si of a known size has been measured, figure 6.12, and is removed from the sample data. The Si wafer density is quoted as 2330 kgm^{-3}. The data is then further corrected to make the moment at fields greater than saturation flat by multiplying by a constant gradient. This raw data at first appears to be in a paramagnetic state, but correcting the data shows a ferromagnetic state with saturation at $\sim 2\ T$ for low temperatures $<\ 25\ K$, figure 6.11 (right).
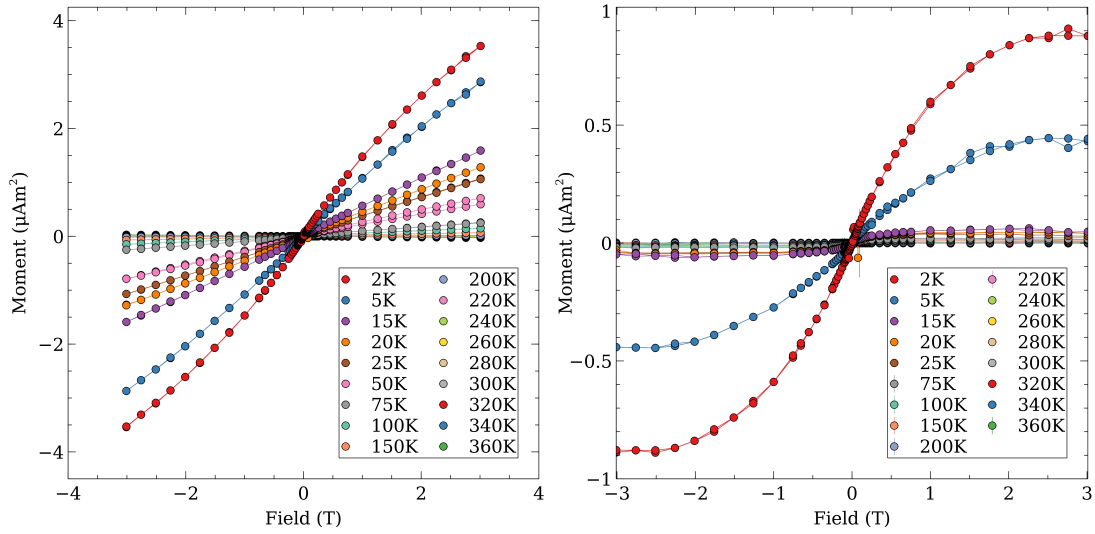
Figure 6.11: *(left) Isotherm measurement of a $Gd_5Si_2Ge_2$ sample a Si/SiO_2 substrate sample at temperatures from 2 K up to 360 K, (right) The same data post correction.*

The standard deviation of the SQUID measurements are taken as the error for the magnetic component, which are an order of magnitude smaller than the measurement. The major source of error is from the measurement of the physical size of samples and estimate thickness's from AFM measurements. Multiple AFM thickness measurements are taken for each sample to attain an error, the same is done for sample and wafer size measurements. Each Si wafer is cut down to a 10 mm square and a .5 mm error is also added to the measurement to account for irregular edges.

The saturation region where moment is unchanged vs field is much higher than that reported by Hadimani et al. and Pecharsky et al. for both thin film and bulk samples at higher temperatures [22, 53]. However, figure 6.13 shows the higher temperature measurements where the saturation is $> 1\ T$ is in good agreement with both the previously measured thin film and bulk studies.
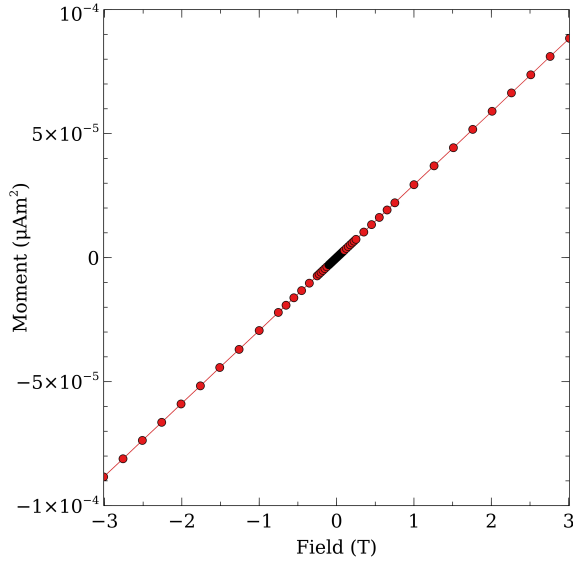
Figure 6.12: *Blank Si/SiO_2 substrate measurement, sample was $10 \times 10 \times 0.6$ mm.*
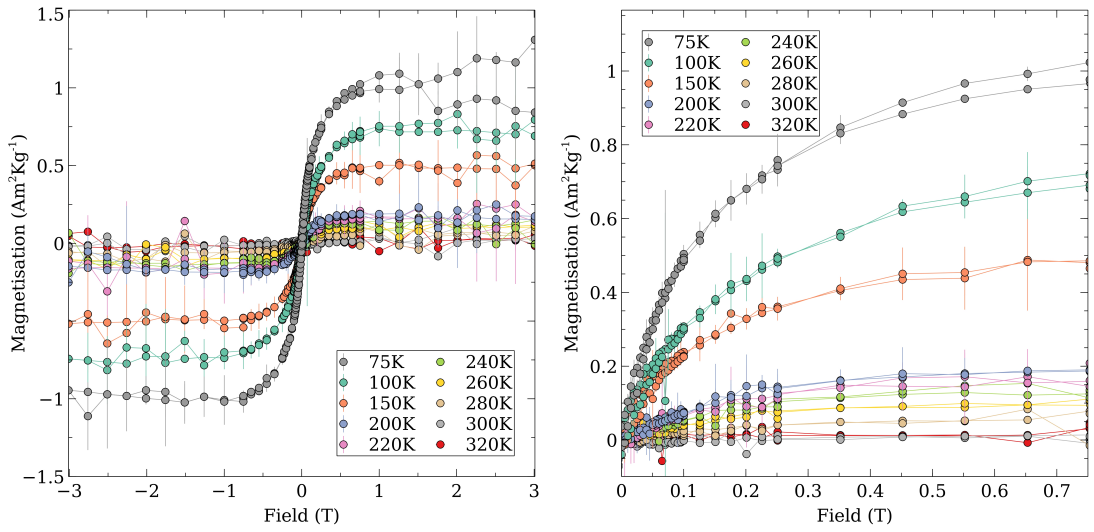
Figure 6.13: *(left) Isotherm measurement of a $Gd_5Si_2Ge_2$ sample on Si/SiO_2 substrate at temperatures from 75 K up to 320 K corrected to remove the Si/SiO_2 substrate background and correct for the mass of the sample, (right) The same data in the first quadrant.*

Despite the decrease in the absolute magnetisation seen in figure 6.8, measurements at temperatures well above the previously found T_c from the temperature

sweeps still show a ferromagnetic like state for all samples. This high-temperature ferromagnetic response, along with the findings in the previous section, 6.5.1, suggest the sample does not consist of $Gd_5Si_2Ge_2$ monoclinic phases alone at temperatures above T_c.

6.5.3   Magnetic Coercivity

The magnetic coercivity in both the high temperature ($>$ 273 K) and low temperature ($<$ 273 K) phase is measured at temperatures from 200 K up to 350 K, with increasing points close to the phase transition via MvsH loops. Both AlN and Si/SiO_2 substrate based samples show an increased coercivity with increased deposition temperature.
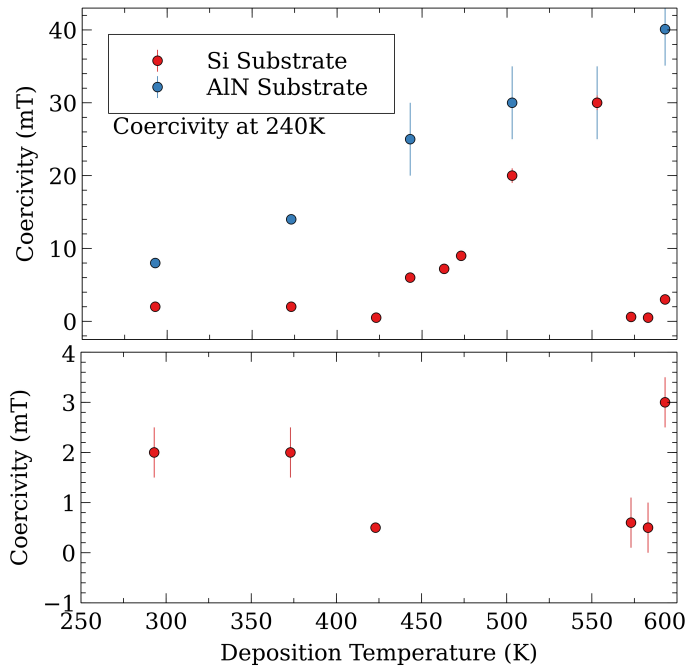
Figure 6.14: *magnetic coercivity measurements of GdSiGe thin films as a function of their deposition temperature. Coercivity measurements are taken at 240 K for each sample.*

Si/SiO_2 substrate based samples show an increased coercivity from 2 mT $\pm$

0.45 mT at 293 K up to 30.3 mT ± 4.4 mT at 553 K. AlN substrate based samples have a similar increase from 8 mT ± 0.4 mT at 293 K up to 30.3 mT ± 4.4 mT at 553 K. Above 553 K, AlN and Si/SiO_2 substrate based samples diverge, with Si/SiO_2 decreasing to 0 coercivity and AlN continuing to increase up to 40.1 mT ± 6.1 mT at 613 K, figure 6.14.

Again, the nature of the samples on Si/SiO_2 substrates change at the T_c of bulk $Gd_5Si_2Ge_2$ but the AlN substrates do not, based upon the AFM measurements in section 6.4. The coercivity to deposition temperature relationship shows a new means to manipulate the magnetic coercivity without the use of doping materials as previously reported [54, 56].
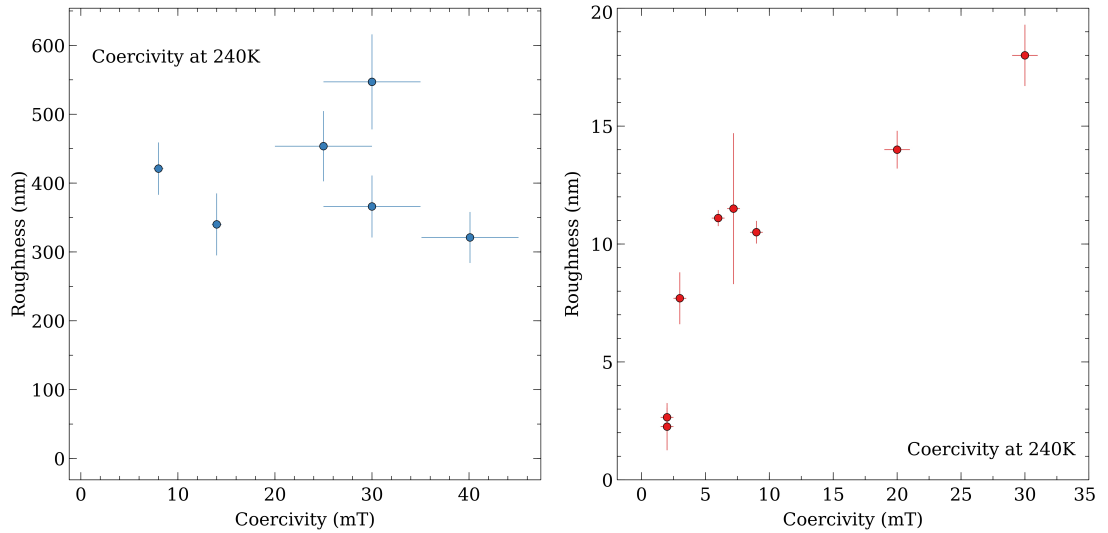
Figure 6.15: *(left) Grain Size measurements of GdSiGe thin films as a function of their deposition temperature, (right) Grain Size measurements of GdSiGe thin films as a function of their deposition temperature on Si/SiO_2 only.*

For the Si/SiO_2 substrate samples, the magnetic coercivity increases with roughness when in the ferromagnetic phase. The AlN substrate samples, figure 6.15 (left) exhibit no apparent relationship between roughness and magnetic coercivity, but the Si/SiO_2 substrate samples, figure 6.15 (right) appears to have

two separate regimes about $\sim 10\ mT$, both with positive linear relationships but with a change in the gradient. The lower regime exists between 0 and 10 mT and the upper regime exists between 10 and 30 mT.

The linear relationship above $\sim 10\ mT$ coincides with the three highest deposition temperatures up to $553\ K$, where there is $< 20\%$ orthorhombic phase during deposition according to figure 6.2. The other regime, $<\ 100\ Oe$, contains samples deposited below $473\ K$ or above $573\ K$, where there is $>\ 20\%$ orthorhombic in the former and $\sim\ 100\%$ in the latter.

The theorised optimal deposition temperature determined from figure 6.2 for $Gd_5Si_2Ge_2$ is close to but not exceeding $\sim\ 573\ K$, for maximising the MCE. However, the surface investigation would suggest that depositing $Gd_5Si_2Ge_2$ at the unfavourable temperatures of $473\ K$ to $20\ K$ would lead to a favourable surface structure (reduced roughness) and magnetic coercivity with little change in the grain-size.

Future depositions should therefore consider whether further material layers are to be deposited on top of the $Gd_5Si_2Ge_2$ and take the surface roughness into account when deciding a deposition temperature, whether an increased surface area due to roughness is desirable or not. The magnetic coercivity of single-crystal $Gd_5Si_{1.8}Ge_{2.2}$ reported by Hadimani et al. is $10.5\ mT$ [121]. So again, thin-film deposition of $Gd_5Si_2Ge_2$ appears to be a trade-off between the MCE performance and another physical or magnetic property, in this case, the magnetic coercivity.

6.5.4 Entropy Change

Both the entropy change, ΔS, and temperature change, ΔT, are fundamental thermodynamic properties used to present a MC material when in bulk form. Due to the nano-scale of our samples, and being attached to a large thermal reservoir (substrates), temperature change data is not shown. Instead, we focus on the entropy change data to analyse the effectiveness of our samples.
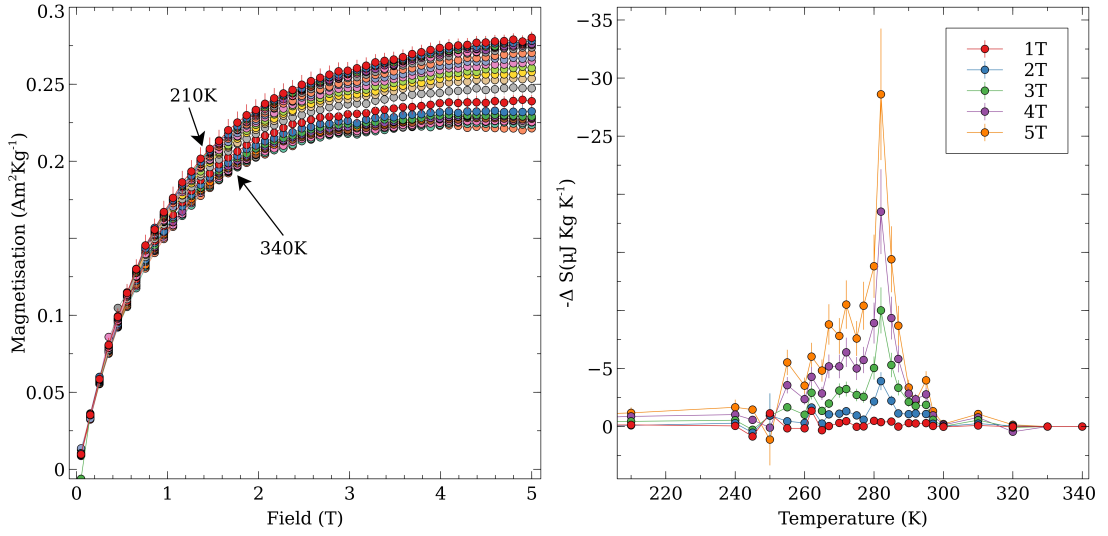
Figure 6.16: *(left) is the virgin curve measurements for a sample grown at 293 K, (right) is the entropy change up to 5 T for the same sample, The key shows the maximum field from 0 T.*

Figure 6.16 (left) shows the initial magnetisation curve of the sample grown at the lowest temperature of 293K in an external field of $0 - 5$ T. Over a temperature range of 210 K to 340 K there is a decrease in magnetisation, with the most significant decrease being between 287 K and 292 K. These temperatures and decrease in magnetisation are higher than the T_c and phase nature of $Gd_5Si_2Ge_2$, a change from a low-temperature orthorhombic ferromagnet to a high-temperature monoclinic paramagnet.

Figure 6.16 (left) does also differ at temperatures above the estimated T_c from what is expected where T_c is determined from the peak moment change, as a paramagnetic response is expected from bulk measurements. We observe a ferromagnetic response with a reduced moment at saturation. This response suggests that our sample consists of more than just $Gd_5Si_2Ge_2$, with secondary ferromagnetic materials screening the paramagnetic response at high temperatures. The reduction does indicate a magnetic phase transition however.

113
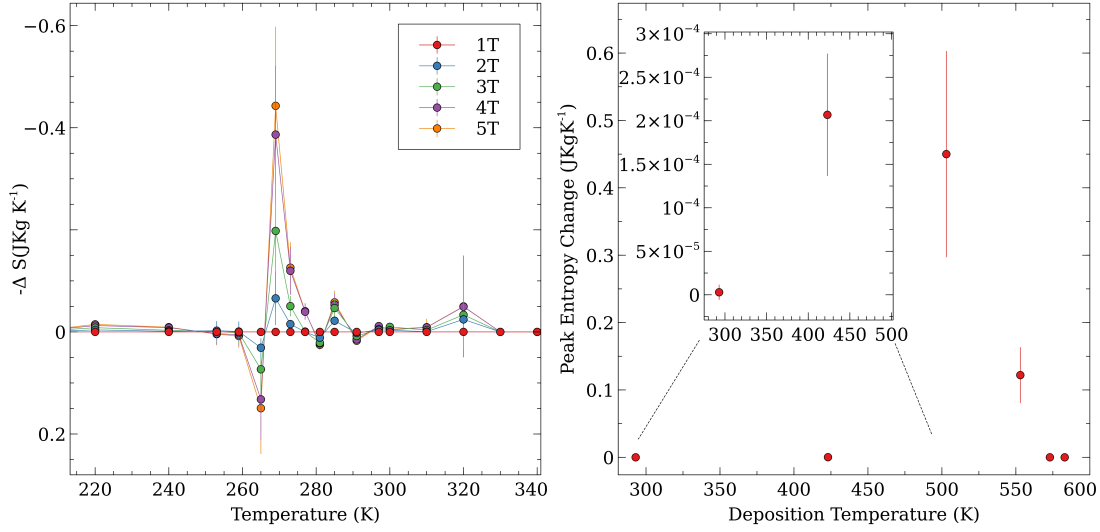
Figure 6.17: *(left) Entropy change measurement from a sample grown at 503 K, (right) the peak entropy change seen for samples grown at varying deposition temperatures.*

The nature of these secondary materials will be discussed further in section 6.6. An entropy change can be determined for the measurement shown in figure 6.16 (left) and is shown in figure 6.16 (right). Grown at 293K, this sample is expected to have a low entropy change response due to the low level of monoclinic phase during deposition determined from figure 6.2. A peak entropy change of $29.2\ \mu JkgK^{-1} \pm 5.7\ \mu JkgK^{-1}$ for a field change of 5T is seen which is extremely small when compared to that published by Pecharsky et al. at $18.5\ JkgK^{-1}$ for a field change of 5 T [3]. This suggests thin film deposition may have a detrimental effect on the entropy change and the aim to increase it.

The largest entropy change recorded for $Gd_5Si_2Ge_2$ samples grown is shown in figure 6.17 (left). This sample was grown at 503 K and has an entropy change of $0.45\ JkgK^{-1}\ pm\ 0.14\ JkgK^{-1}$ for 5 T, a value much larger than the previously discussed sample but still smaller than reported by Pecharsky et al. [3].

Being deposited at 503 K, the sample data shown in figure 6.17 (left) was not expected to have the largest entropy change. A sample grown at 553 K and

114

visible in figure 6.17 (right) alongside other samples grown was expected to be the highest performing, with the most significant percentage of monoclinic phase during deposition. Figure 6.17 (right) would indicate that without significant levels of monoclinic phase during deposition, the entropy change becomes negligible. When depositing above 553 K the phase change disappears and the associated entropy change with it.

These results, coupled with those found in the surface study indicate a deposition temperature below the theorised optimal temperature would be the most appropriate for furthering thin-film $Gd_5Si_2Ge_2$, due to the increased entropy change, decreased surface roughness and decreased coercivity. The deposition parameters for PLD deposition of these samples are; Ar atmosphere of 7 μTorr or 20 mTorr, laser frequency of 18 Hz, fluence of 9.55 to 12.73 J/cm^2, and chamber temperatures below 553 K.

The model results presented in chapter 5 along with the literature review also show an increased quantity of Ge relative to Si would have an increased entropy change. This, coupled with the higher T_c of the thin films, means the correct choice of bulk material from ablation could result in a sample with the same T_c as $Gd_5Si_2Ge_2$ with an increased ΔS.

6.5.5 Hysteresis; Thermal and Magnetic

Magnetic hysteresis is present within $Gd_5Si_2Ge_2$ while in its lower temperature orthorhombic phase and forms one of the main characteristics of a ferromagnet. FOPT materials such as $Gd_5Si_2Ge_2$ also have an associated latent heat with their phase transition, leading to the discontinuity seen in the energy-temperature relationship. This leads to a measurable thermal hysteresis within the material about the T_c. The change in crystal phase that associated with the latent heat also causes structural changes that can lead to cracks and damage to samples.
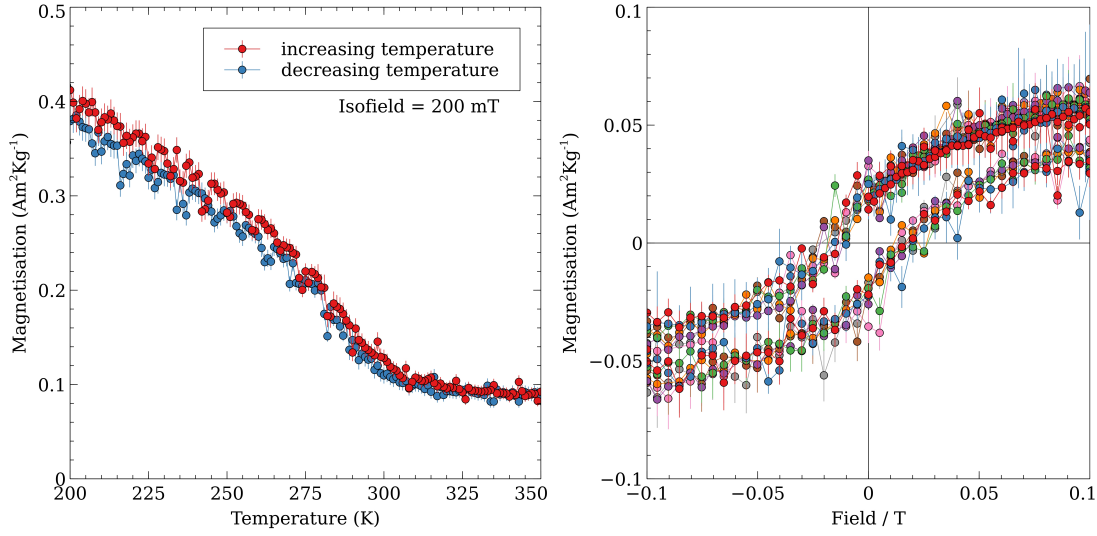
Figure 6.18: *(left) isofield measurements for both an increasing and decreasing temperature regime, (right) Magnetic isothermal loops at several temperatures between 240 K and 330 K.*

Figure 6.18 (left) and (right) show measurements of thermal and magnetic hysteresis within thin-film $Gd_5Si_2Ge_2$ respectively. The isofield measurements in figure 6.18 (left) are for the sample grown at 503 K, showing the largest entropy change. Unlike thin film samples reported by Hadimani et al. [22, 5] there is little to no thermal hysteresis visible. There is a large difference in our sample thickness' and those reported by Hadimani (150 $\pm$ 20 nm vs 616 nm [22]) however, so layered structural understanding of both samples sets is required to further understand the origin of the difference. A lack of thermal hysteresis could again open a new avenue of research for $Gd_5Si_2Ge_2$ as it could potentially allow for its industrial introduction without the need for doping to achieve similar results [54, 56]. The lack of thermal hysteresis is more likely to point towards the FOPT not being preserved during the thin film growth and that samples grown are showing a SOPT like transition. The large decrease in ΔS when compared to bulk in the previous section would also point towards this. As a SOPT transition is still present and the T_c has slightly increased, this would suggest either an

116

increase in the Si/Ge ratio during deposition. Pushing the samples into the higher temperature SOPT regime as seen in figure 6.1 or some secondary effect caused by the thin film growth or dimensions.

Figure 6.18 (right) shows the coercivity in several isothermal measurements from 240K to 330K. There is little change in the coercivity over the temperature range, but as previously described there is evidence of secondary phases within the sample that will contribute to, and given the paramagnetic state of $Gd_5Si_2Ge_2$ at high temperatures likely dominate, the coercivity.

6.6   Structure

Structural analysis is performed using XRD, XRR and PNR as described in chapter 4. XRD is used to identify the material and phases present within the thin film samples as a function of temperature. XRD and PNR are used to identify layer structures, densities and magnetic properties.

6.6.1   XRD

Thin-film $Gd_5Si_2Ge_2$ is measured using XRD in the 2Θ range of $0°$ to $60°$, shown in figure 6.19 (left). Data is shown for temperatures ranging from 219 K to 310 K. Figure 6.19 (right) shows the same data in the range $9°$ to $27°$ and has arrows to indicate the change in count and movement in diffraction angle as measurement temperature decreases.

The large peak visible at $6.4°$ is attributed to the Si substrate, while the three prominent peaks with visible movement in figure 6.19 (right) can be attributed to orthorhombic $Gd_5Si_2Ge_2$, shown in Figure 6.19 (right). After fitting further materials are also found indicating that there is a level of oxidation during or post-deposition, with the most significant percentage found being $Gd_2Ge_2O_7$.

117
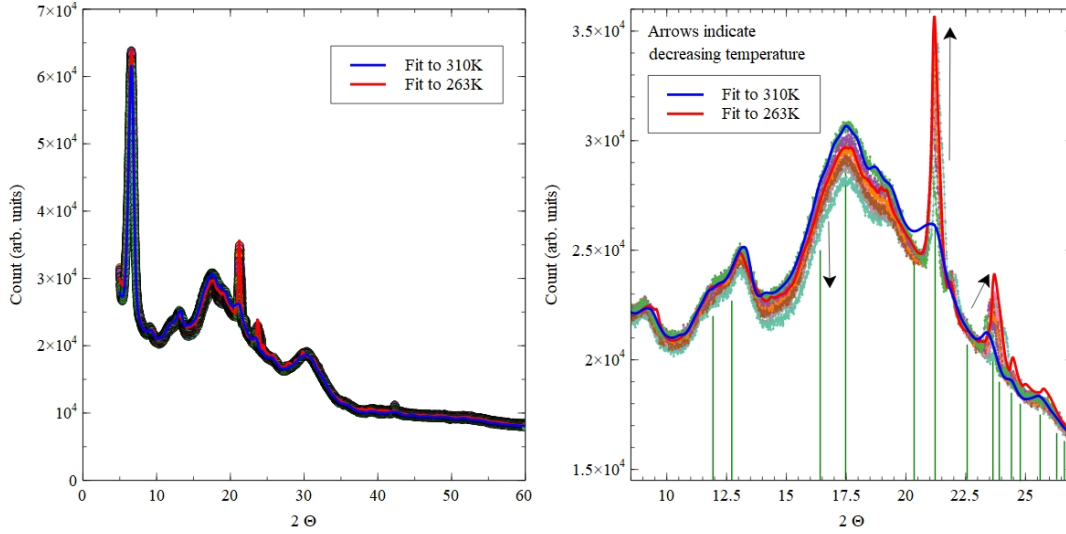
Figure 6.19: *(left) XRD data of the full 2 Θ range used to study $Gd_5Si_2Ge_2$, (right) focus on the 2 Θ range of interest, arrows are used to indicate the change in both angle and count over a decreasing temperature. Green lines indicate expected Bragg peaks for the $Gd_5Si_2Ge_2$ Orthorhombic phase.*

Whole Powder Pattern Fitting (WPPF) gives a high of 42% Orthorhombic phase below the T_c, while giving a low of 0.4% when above. Fitting also gives $Gd_2Ge_2O_7$ and $Gd_2Si_2O_7$ as being present with a FOM χ^2 of $\sim$ 1% across the temperature range.

Figure 6.19 (right) indicates the peak positions for the substrate SiO_2, $Gd_2Ge_2O_7$ and $Gd_2Si_2O_7$. Fitting to plots gives a content estimation for the four largest phases found, $Gd_5Si_2Ge_2$ (orthorhombic), SiO_2, $Gd_2Ge_2O_7$ and $Gd_2Si_2O_7$. At the lowest temperature of 263 K there is an estimated 42(18)% of $Gd_5Si_2Ge_2$, 43(12)% of SiO_2 (assumed to be mainly substrate), 14(24)% of $Gd_2Ge_2O_7$ and 1(30)% of $Gd_2Si_2O_7$. The parameters for each phase are tabled in the appendix.

The percentage of $Gd_5Si_2Ge_2$ (orthorhombic) largely decreases as the temperature increases down to 0.4(11)% at 293 K and remains low up to 310 K. Interestingly, as the temperature increases, the $Gd_2Ge_2O_7$ and $Gd_2Si_2O_7$ also go through a large content percentage change, with $Gd_2Ge_2O_7$ decreasing to 9(28)%

at 293K and $Gd_2Si_2O_7$ increasing to 25(22)%. SiO_2 content although changing (43(12)% to 56(71)%) shows no relationship with temperature and is likely due to changes in beam/sample positioning between measurements. Fitting to $Gd_5Si_2Ge_2$ (monoclinic) was attempted but the percentage content was a maximum of 10(10)% at 310K and had a large FOM of 13%.
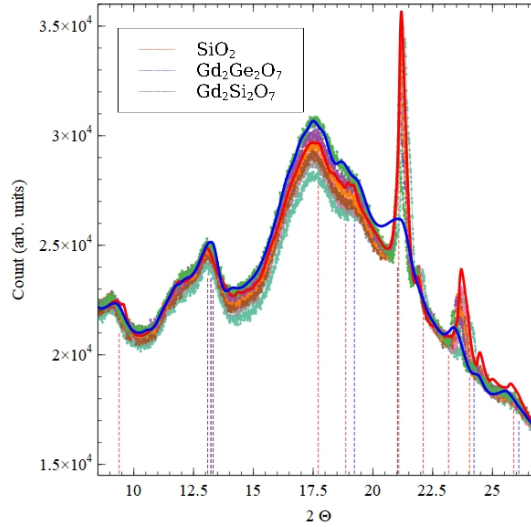
Figure 6.20: *focus on the 2 Θ range of interest, vertical lines indicate peak positions for secondary phases detected.*

6.6.2 Reflectometry; X-ray and Neutron

Both XRR and PNR are performed on $Gd_5Si_2Ge_2$ thin films, figure 6.21 (left) and (right) show XRR and PNR results at room temperature respectively. GenX is used for fitting both data sets.

Both XRR and PNR fitting indicate a bilayer system for the $Gd_5Si_2Ge_2$ thin film with amorphous materials, with the layer in contact with the substrate being denser than the layer above at the surface, at $0.00423 \ at.\mathring{A}^{-1}$ vs $0.004 \ at.\mathring{A}^{-1}$. Co-fitting both XRD and PNR show a thickness of $152.1 \ nm$ for a $Gd_5Si_2Ge_2$ sample on the SiO_2 substrate, where AFM thickness measurements put this sample at $130nm \pm 24 \ nm$. Given the large length scales for the AFM measurement, this

difference is not unreasonable. Fitting to surface roughness gives a value of 7.04 $Å$, AFM measurements give a roughness of 10.1 ± 4.8 $Å$. Fitting also estimates the SiO_2 thickness for XRR and PNR to be 273 $nm \pm 10$ nm compared to the manufacturer quote of 300 nm of SiO_2.
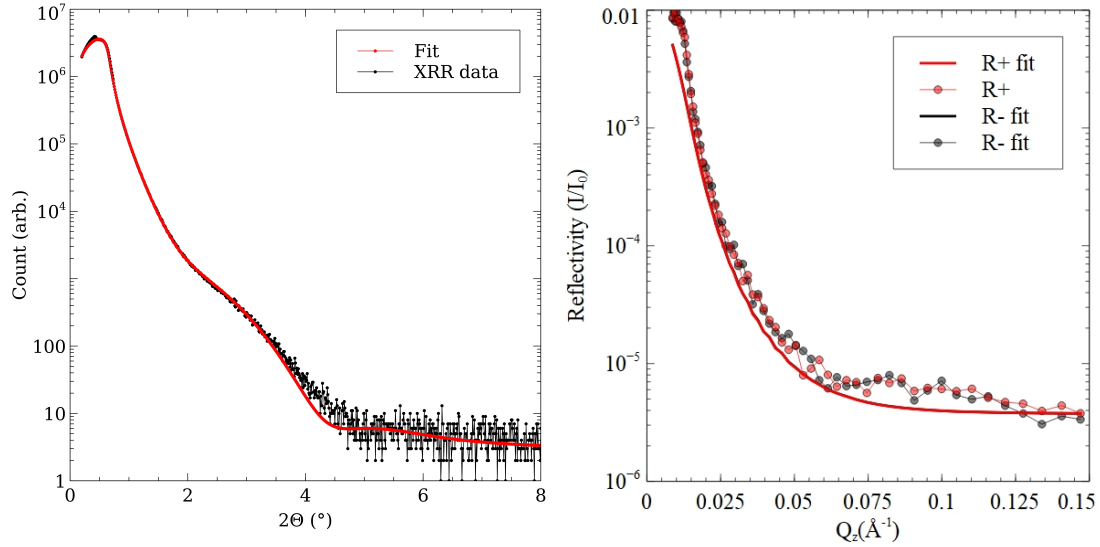
Figure 6.21: *(left) XRR of thin film $Gd_5Si_2Ge_2$, (right) PNR of the same $Gd_5Si_2Ge_2$ measurement, in a 200mT field.*

SLD (Scattering Length Density) data and tabulated results are shown in figure 6.22 and table 6.1. The high magnetic moment fitted for the $Gd_5Si_2Ge_2$ layer at the substrate interface, figure 6.22 (right) at room temperature, ferromagnetic nature identified in figure 6.8 and wide peaks visible in figure 6.19 would suggest a semi-amorphous ferromagnetic material is present. XRD fitting in figure 6.20 also finds $Gd_2Ge_2O_7$ and $Gd_2Si_2O_7$ phases with amorphous wide peaks. As the PNR measurement was performed at room temperature, the thin film sample will be above the T_c, and the $Gd_5Si_2Ge_2$ will be in a paramagnetic state, indicating the interface layer will contain the majority of the $Gd_2Ge_2O_7$ amorphous, ferromagnetic material present in the XRD analysis and that it is not randomly distributed as initially presumed, but in higher concentration towards the substrate.
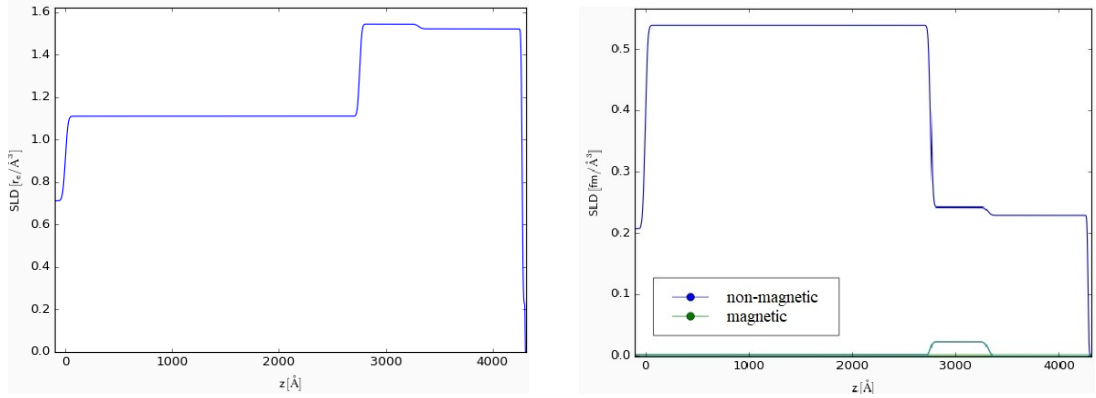
Figure 6.22: *(left) SLD for XRR data on the $Gd_5Si_2Ge_2$ sample, (right) SLD for PNR data on the $Gd_5Si_2Ge_2$ sample, in a 200 mT field.*

For the fitting parameters it is assumed that the stoichiometry of the GSG layers is $Gd_5Si_2Ge_2$. Parameters for the X-ray and Neutron beam are those given by the ISIS facility and allowed a 5% margin. Fitting is also performed with a $Gd_2Ge_2O_7$ or $Gd_2Si_2O_7$ layer at the substrate interface, surface and middle of the $Gd_5Si_2Ge_2$ layer, but all provide a FOM an order of magnitude higher than when omitted. Therefore the secondary phases found via XRD are assumed to not be a cohesive layer but to be randomly distributed within the $Gd_5Si_2Ge_2$ interface layer close to the substrate.

Table 6.1: Fitted values for XRR and PNR data of a $Gd_5Si_2Ge_2$ sample on SiO_2.

Layer	Parameter	Fitting Result
Amb	$\rho/at.\mathring{A}^{-1}$	
	R / $\mathring{A}$	
GSG Surface	D / $\mathring{A}$	968 ± 52
	$\rho/at.\mathring{A}^{-1}$	$4 \times 10^{-3} \pm 0.2 \times 10^{-3}$
	R / $\mathring{A}$	7.04 ± 0.4
	$M/\mu_B FU^{-1}$	$8.81 \times 10^{-2} \pm 0.9 \times 10^{-2}$
GSG Interface	D / $\mathring{A}$	553 ± 12
	$\rho/at.\mathring{A}^{-1}$	$4.23 \times 10^{-3} \pm 0.21 \times 10^{-3}$
	R / $\mathring{A}$	25.01 ± 1.09
	$M/\mu_B FU^{-1}$	$1.98 \times 10^{-2} \pm 0.55 \times 10^{-2}$
SiO_2	D / $\mathring{A}$	273 ± 10
	$\rho/at.\mathring{A}^{-1}$	$3.42 \times 10^{-3} \pm 0.15 \times 10^{-3}$
	R / $\mathring{A}$	16.04 ± 5.1
	$M/\mu_B FU^{-1}$	0
Si	$\rho/at.\mathring{A}^{-1}$	
	R / $\mathring{A}$	

6.7 Summary

Thin Film $Gd_5Si_2Ge_2$ have been grown via PLD on SiO_2 and AlN substrates. AFM thickness and roughness measurements show the films are 80 ± 10 nm to 150 ± 20 nm and describe an optimum temperature range to minimise roughness, magnetic coercivity and grain sizes.

Magnetic measurements identify a gradient change close to room temperature and a peak change at temperatures higher than the bulk counterpart. Magnetic measurements also show a higher than expected magnetic moment above the T_c, indicating the presence of other magnetic phases.

Maximising the monoclinic phase during deposition is theorised to increase the maximum entropy change. Calculated entropy change for thin films shows this is not the case and that lower temperatures may be optimal for both maximum entropy change and lowering coercivity and surface roughness.

Structural measurements show the presence of amorphous material and secondary phases, mainly $Gd_2Ge_2O_7$ and $Gd_2Si_2O_7$. A bi-layer structure is also shown with the secondary phases predominantly in the lower layer interfacing the substrate.

When compared to bulk studies, thin film $Gd_5Si_2Ge_2$ on the order of ~ 80 nm to 150 nm appears to have a significantly reduced thermal hysteresis, ≈ 0 vs 6 K without doping. This can be attributed to the SOPT like transition seen for the thin film samples.

The reduction in thermal hysteresis and entropy change point towards the loss of the FOPT like transition, with the PLD deposition leading to SOPT like samples containing secondary phases.

6.7.1 Future Potential

Further investigation was planned to study the effect of strain on the samples. Piezoelectric PZT or BTO substrates pose an opportunity to investigate the magnetisation as a function of substrate strain. Also planned was a study of multiple depositions on the same substrate of differing temperature, Si/Ge ratios or other MCE materials which may introduce a cascading phase change effect within the sample by depositing materials with gradually increasing T_c atop one another. This could lead to an increased operating temperature range.

Further study into the working life cycle of thin-film $Gd_5Si_2Ge_2$ could provide a path to improving the longevity of the MCE. Investigating repeated phase changes as a function of time would be a useful next step.

Ultimately, the aim of researching thin-film MC materials is to embed them into the silicon chip industry, so deposition onto working silicon-based circuits could provide the next step to real-world industrial applications.

Thin Film $La_1Fe_{1.895}Co_{0.91}Si_{1.105}$ Growth and Magnetocaloric properties

This chapter will describe the preparation and characterisation of magnetocaloric $La_1Fe_{1.895}Co_{0.91}Si_{1.105}$ thin films. All films are grown from the same $La_1Fe_{1.895}$ $Co_{0.91}Si_{1.105}$ target using PLD on both AlN and Si/SiO_2 substrates. This stoichiometry is chosen as it has a T_c near room temperature and is readily available from Vacuumschmelze. Magnetometry is performed using a mixture of SQUID and VSM. Both isothermal and isofield measurements are conducted to determine magnetic phase transitions and associated thermodynamic properties. The topography is investigated using an AFM with a particular interest in the grain sizes,

surface roughness and film thickness. The structural investigation is performed using XRR and PNR, the interference caused by the substrate/film interface and surface are detailed.

7.1 Material Introduction

Rare earth, intermetallic compounds are among those of increased recent research due to many exhibiting near room temperature first and second-order phase transitions (FOPT SOPT). Of the intermetallics with a 3d transition metal and cubic $NaZn_{13}$ structure, only $LaCo_{13}$ is stable, but with the addition of Si, $LaFe_{13}$ can stabilise and provide a relatively high Curie temperature. Further introduction of Co or H will allow for manipulation of the Curie temperature in the range that is required for a working magnetocaloric refrigerator. Bulk studies have received the most interest in the magnetocaloric field, with some prototype refrigerators already being made. Nanoparticles are also seeing a surge in research, but thin-film magnetocalorics are still less represented in the literature. There are no known thin-film studies of the LaFeSi based group of materials. In this chapter, the growth and characterisation of thin-film LaFeCoSi samples are presented, where the magnetocaloric effect close to room temperature persists despite the high energy deposition technique used.

7.2 Growth

Unlike $Gd_5Si_2Ge_2$, to date it has not been reported that $La_1Fe_{1.895}Co_{0.91}Si_{1.105}$ has been grown as a thin film via PLD.

$La_1Fe_{1.895}Co_{0.91}Si_{1.105}$ like $Gd_5Si_2Ge_2$ has metallic-like properties, meaning a lot of the incoming laser energy is reflected, and the material requires a high level of energy to form plumes. Laser fluences up to 12.73 J/cm^2 are used, fluences below 11.46 J/cm^2 result in no plume forming, however, so results for fluences of

$11.46 \ J/cm^2$ and above are shown from here onwards. A laser frequency of 18Hz is chosen for all depositions.

7.3 Surface

In this section, the roughness and grain-size are used to investigate the deposition of $La_1Fe_{1.895}Co_{0.91}Si_{1.105}$ with varying chamber parameters and compared to magnetic data.

7.3.1 Roughness

The same process described in chapter 6 will be used here to calculate the surface roughness. Figure 7.1 shows two AFM surface plots of $La_1Fe_{1.895}Co_{0.91}Si_{1.105}$ on Si/SiO_2 substrates at different scales; the granular structure is due to the plume deposition nature of PLD and visually appears similar to the results seen in chapter 6. Island and layer structures that can be produced via PLD [102] are not directly observed for LFS thin films, but may still be present or contributing to the observed structure.
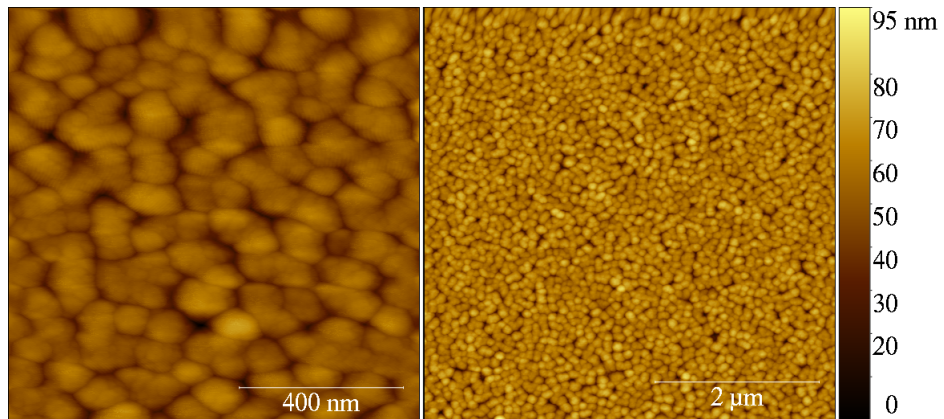
Figure 7.1: *AFM images of LFS samples grown at 293K.*

Unlike the $Gd_5Si_2Ge_2$ thin film samples, those deposited on AlN do not have a significant change in roughness compared to Si/SiO_2 substrate samples as

shown in figure 7.2 (left). Interestingly, $La_1Fe_{1.895}Co_{0.91}Si_{1.105}$ thin film roughness is affected by the deposition pressure, With samples deposited in a vacuum showing far more significant and more varied roughness over the full deposition temperature used. 7 μTorr deposited substrate samples show a steep increase in roughness over the 293 K to 423 K range from 67.45 nm $\pm$ 2.5 nm to $476nm \pm 30nm$, where the roughness then plateaus and steeply decreases above 623 K to 131.5 nm $\pm$ 10.1 nm. These 7 μTorr deposited samples have a far greater roughness than those at 20 mTorr. Samples deposited in 20 mTorr Ar however, have a steady decline from 12.2 nm $\pm$ 2.8 nm to 4.2 nm $\pm$ 0.9 nm over the same temperature range. An increase in chamber pressure with an inert gas has been shown to decrease roughness by Eason [102].
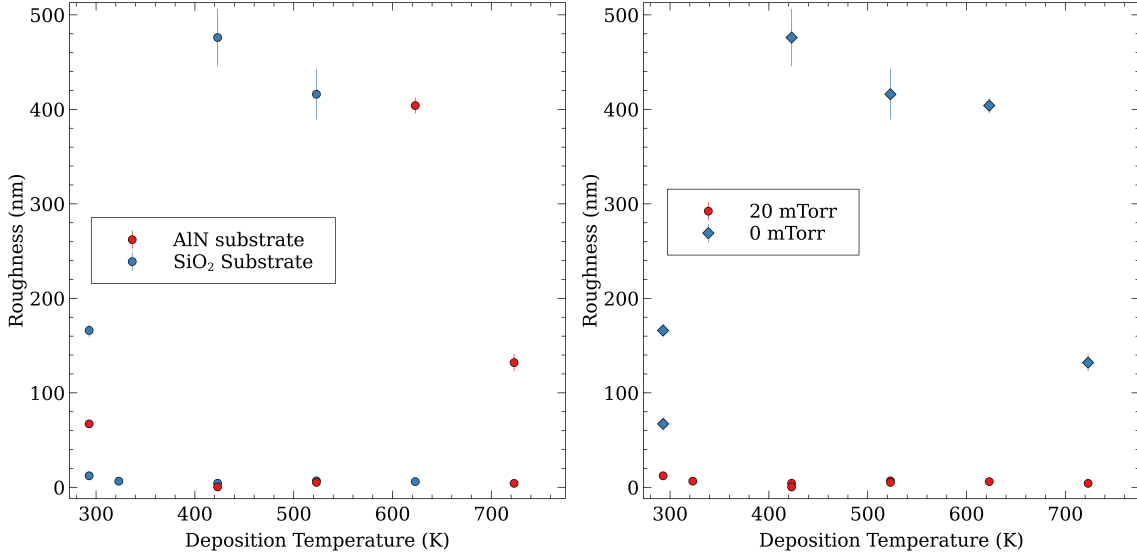
Figure 7.2: *(Left)Roughness against deposition temperature for both AlN and SiO_2 substrate samples,(Right) Roughness against deposition temperature for samples grown in 20 mTorr Ar and 7 μTorr.*
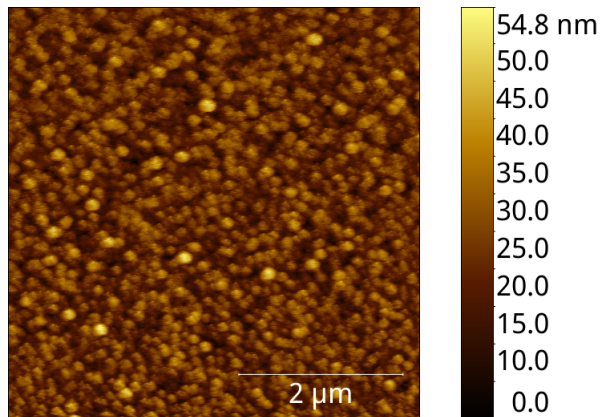
8

Thin Film $La_1Fe_{1.895}Co_{0.91}Si_{1.105}$ Growth and Magnetocaloric properties

This chapter will describe the preparation and characterisation of magnetocaloric $La_1Fe_{1.895}Co_{0.91}Si_{1.105}$ thin films. All films are grown from the same $La_1Fe_{1.895}$ $Co_{0.91}Si_{1.105}$ target using PLD on both AlN and Si/SiO_2 substrates. This stoichiometry is chosen as it has a T_c near room temperature and is readily available from Vacuumschmelze. Magnetometry is performed using a mixture of SQUID and VSM. Both isothermal and isofield measurements are conducted to determine

8.6.2 Grain Size

Figure 7.4 shows the average size of the grains as a function of deposition temperature. There is a small decrease in average grain size at higher deposition temperatures as well as two Si substrate samples that seem to show a steep increase at 423 K and 523 K. Despite this relationship, there seems to be no relationship in the average sample thickness with temperature, or a relationship between the sample roughness and grain size. All samples were grown for 1 hour to control growth. Figure 7.4 also shows vacuum deposited samples with a similar grain size to that of 20 mTorr Ar deposited samples.

The surface roughness of the $La_1Fe_{1.895}Co_{0.91}Si_{1.105}$ thin films appear to have a stronger dependence on the deposition chamber pressure and temperature than either the substrate choice or resulting grain size, as seen in figures 7.2 and 7.5 (left).
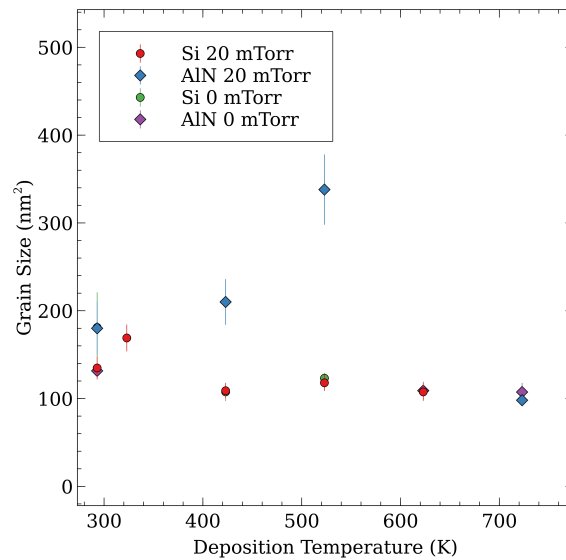
Figure 8.22: *Average grain size against deposition temperature for both Si/SiO_2 and AlN substrate samples at 20 mTorr Ar and 7 μTorr during deposition.*
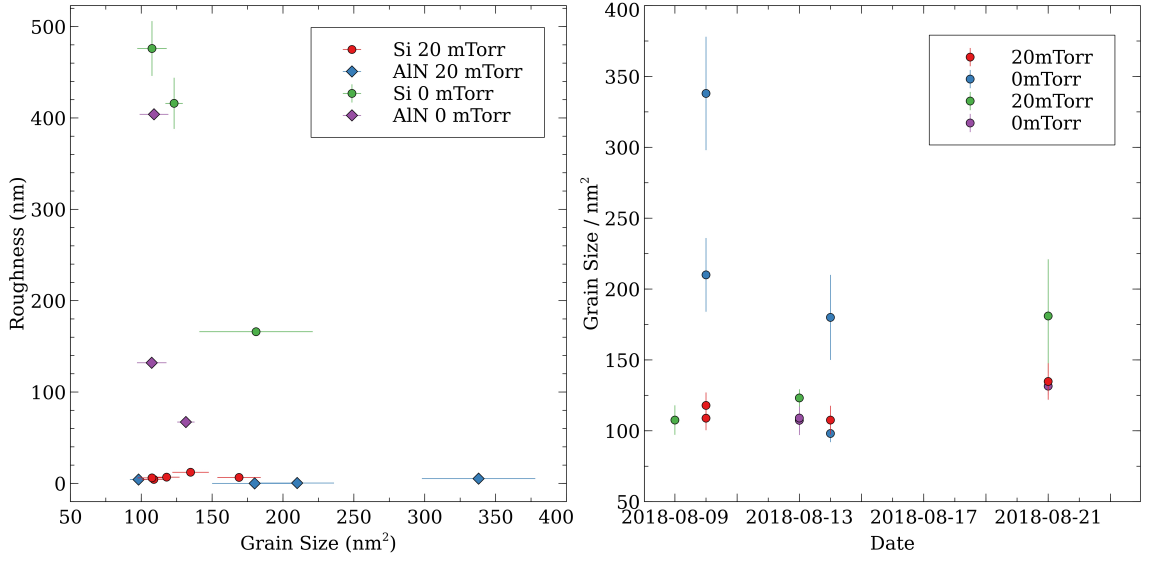
Figure 8.23: *(Left) Roughness against grain size for both Si/SiO_2 and AlN substrate samples, (Right) Grain Size against the deposition date for both Si/SiO_2 and AlN substrate.*

There is no apparent relationship between the grain size and surface roughness for $La_1Fe_{1.895}Co_{0.91}Si_{1.105}$ thin films, unlike the $Gd_5Si_2Ge_2$ thin film samples shown previously. The deposition pressure affects the final results by separating them into 2 regimes, the first deposited at 7 μTorr have a large variation in roughness but not grain size, the second deposited at 20 mTorr has the reverse.

Those samples deposited in 7 μTorr have the highest roughness at temperatures between 423 K and 623 K. There is also no increase in the grain size with deposition date, suggesting no degradation in the target.

8.6.3 Thickness

Thickness measurements are taken from the edge of the deposited $La_1Fe_{1.895}$ $Co_{0.91}Si_{1.105}$ to the SiO_2 substrate. All samples have a thickness range of 35-80 nm for a 60-minute deposition, with the thickest sample being deposited in the

lowest pressure possible in the PLD. Samples deposited on AlN have a similar thickness to their SiO_2 counterpart but have a larger error due to the increased roughness of the substrate.

The same process to that described in chapter 6 is used to create an edge to measure from and a similarly wide edge profile is seen in the $La_1Fe_{1.895}Co_{0.91}Si_{1.105}$ samples.

The sample shown in figure 7.6 is a profile measurement taken from an AFM and has a thickness of 35 nm $\pm$ 10 nm and an edge slope of $\sim$ 20 μm. Droplets are visible on top of the sample as three distinct spikes.
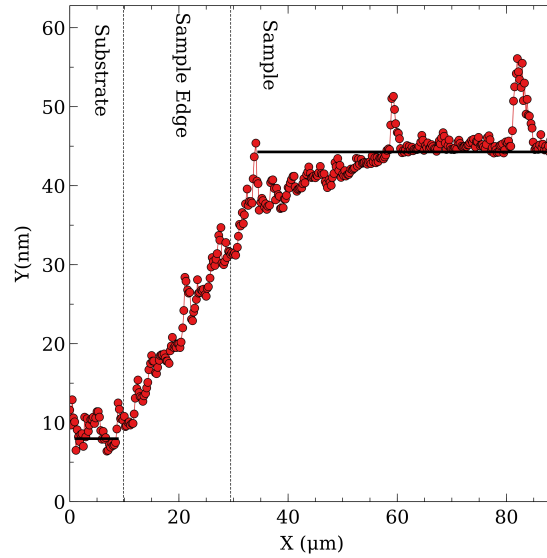
Figure 8.24: *AFM thickness measurement of a $La_1Fe_{1.895}Co_{0.91}Si_{1.105}$ thin film on Si/SiO_2 substrate.*

8.7   Magnetism

Both isofield and isothermal measurements are performed on the $La_1Fe_{1.895}Co_{0.91}$ $Si_{1.105}$ thin films using a SQUID magnetometer described in chapter 4. Mass calculations use the density of LaFeCoSi, 7143 kgm^{-3} determined by Bjork et al. [124] and the measured thickness and dimensions of the film samples.

8.7.1 Isofield

All ablated samples of $La_1Fe_{1.895}Co_{0.91}Si_{1.105}$ were deposited with a substrate temperature ranging from 293 K to 723 K. Samples deposited below 623 K show a significant decrease in the magnetic moment vs temperature for an increasing temperature, this magnetic transition is no longer present when deposited at 623 K. A small change does appear greatly diminished at 723 K however, figure 7.7.

The data sets shown in figure 7.7, deposited at 293 K to 723 K, show a change in moment gradient, indicating a magnetic phase change. Growth techniques for LaFeCoSi [32] require a long period of heat treatment at temperatures above 1223 K so that the required phase becomes dominant. The magnetocaloric $NaZn_{13}$ phase is stable at room temperature but will decompose more readily at higher temperatures [125]. The PLD's high energy deposition technique coupled with the high-temperature is therefore theorised to be the cause of the decreased and or missing magnetocaloric effect at 623 K. Reducing substrate temperature leads to increased moment change and therefore, magnetocaloric response.
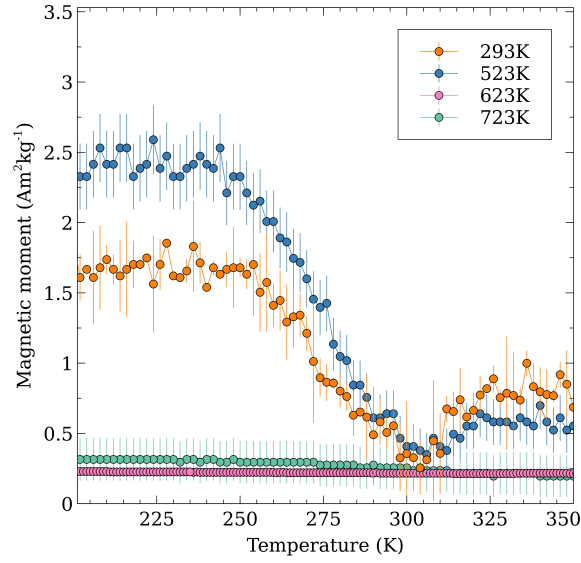
Figure 8.25: *Magnetic moment against temperature for $La_1Fe_{1.895}Co_{0.91}Si_{1.105}$ thin film on Si/SiO_2 substrates, samples from multiple deposition temperatures are shown.*

All isofield measurement data below 623 K also show a positive gradient, resulting in a slight increase in the magnetic moment above 300 K. This increase is present in all samples deposited in the substrate temperature range of 293 K-523 K regardless of the samples deposition chamber pressure. Samples grown at 623 K and above no longer show a positive gradient.
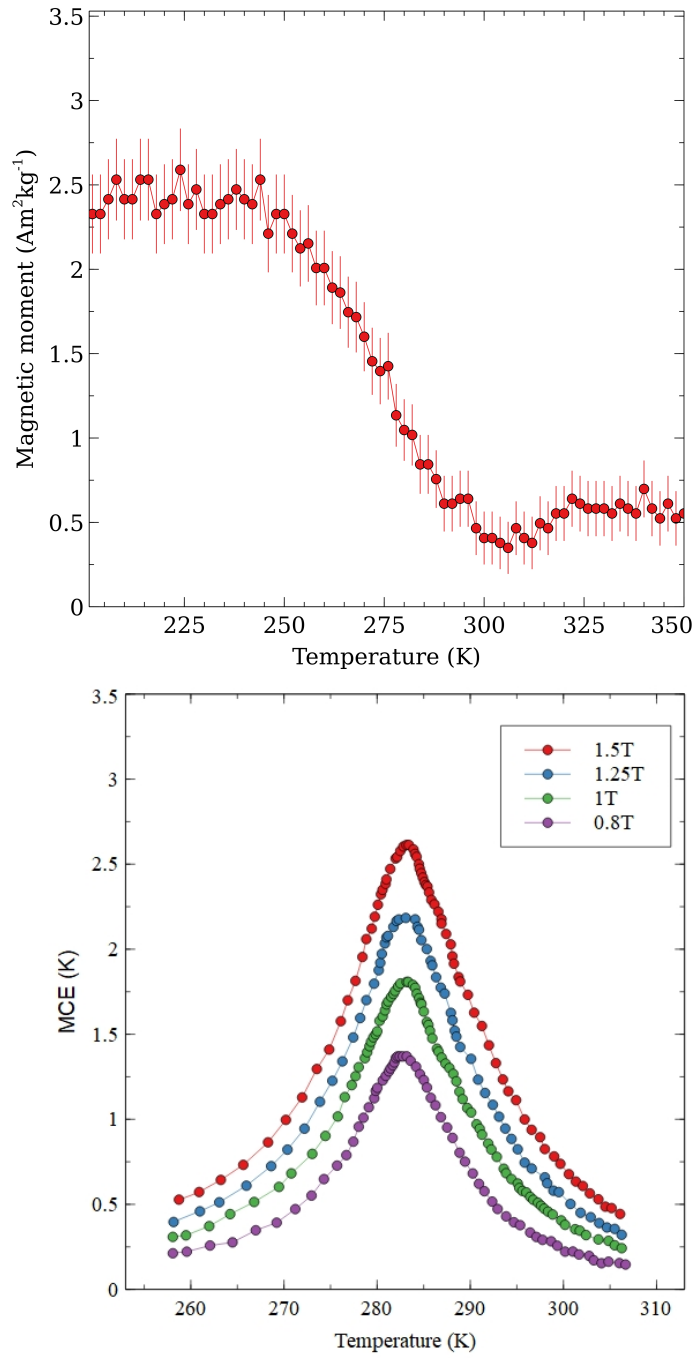
Figure 8.26: *(Top)Magnetic moment against temperature at a constant field of 200 mT for a $La_1Fe_{1.895}Co_{0.91}Si_{1.105}$ thin film grown at 523 K,(Bottom) Temperature change against temperature determined for the bulk target used for deposition, data provided by Vacuumschmelze GmbH.*

Unlike the $Gd_5Si_2Ge_2$ thin film, the paramagnetic state magnetisation of the $La_1Fe_{1.895}Co_{0.91}Si_{1.105}$ thin film is not greater than that found for bulk measurements. Lollobrigida et al. show a magnetisation of $\sim 2.5\ Am^{-2}Kg^{-1}$ for 200 mT, while thin-film samples show the lowest magnetisation of 0.3 $Am^{-2}Kg^{-1}$ $\pm$ 0.15 $Am^{-2}Kg^{-1}$ at 306 K while under a 200 mT constant field. At temperatures above 300 K, above the positive gradient, the magnetisation is still below that reported for bulk. This magnetisation decrease would indicate that there is a large non-magnetic component present within the film [126].

The T_c of the $La_1Fe_{1.895}Co_{0.91}Si_{1.105}$ thin film also appears to have reduced in temperature compared to the bulk counterpart used for deposition, with the bulk having a peak at 283 K but the thin film peak is appearing at 272 K.

Spin Glass Like Behaviour

Lower temperature measurements also reveal a spin glass like effect within the films. Field cooled (FC), and zero-field cooled (ZFC) measurements shown in figure 7.9 have a freezing temperature of 100 K for a sample grown at 293 K in a vacuum. Spin glass behaviour has been reported previously in LaFeSi compounds where Fe sites are partially replaced by either Mn or Al[127, 128]. There is no known reported spin glass behaviour in LaFeCoSi compounds, however it is not certain if the source of the spin glass within the thin films is from the compound material or the granular, non-single crystal nature of the films formed from the PLD process. Magnetisation vs time measurements over a large time period would be required to assess the nature of the spin glass like behaviour.

136
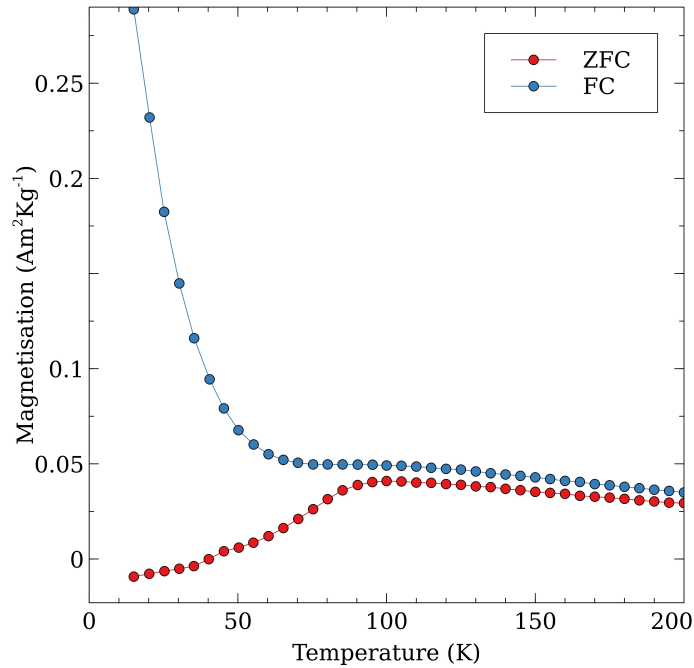
Figure 8.27: *ZFC and FC measurements of LFS, ZFC measurements are taken before the FC measurements.*

8.7.2 Isothermal

After identifying the gradient change region, several temperature points are chosen for isothermal MvsH loops with a particular interest in the virgin curve. The process laid out by Lyubina et al. is used [32], where after each isothermal measurement is taken the sample is heated or cooled well above or below the T_c for decreasing or increasing temperature measurements. This is used to ensure correct analysis of the MCE.

Isothermal measurements are not taken uniformly, figure 7.10 shows a standard choice of temperature points chosen for measurement about the T_c. There will also be sparse measurements at much lower temperatures down to 2 K.
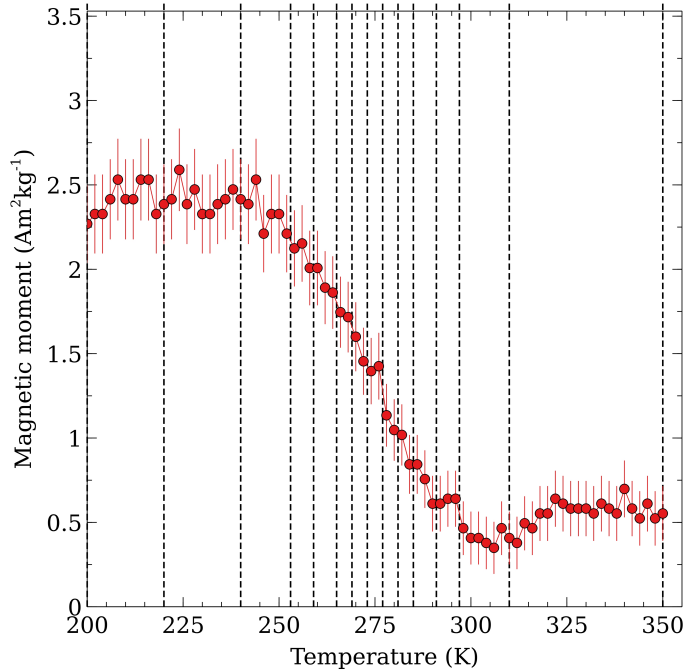
Figure 8.28: *Example temperatures chosen for isothermal measurements.*

SQUID isothermal measurements at increasing temperatures show the most suggestive evidence of a phase transition within the $La_1Fe_{1.895}Co_{0.91}Si_{1.105}$ thin films. A change in the gradient of the magnetic moment as a function of temperature, figure 7.8 (top) gives the first indication of a critical temperature for a sample grown at 523 K, close to that of the bulk target used, 283 K figure 7.8 (bottom). The decreasing magnetic moment at saturation for isothermal measurements gives the second indication, figure 7.11.

Magnetic hysteresis curves at increasing temperatures reveal a decrease in the magnetic moment. A decrease from the maximum magnetic moment at 3 T, 100 K of 2.396 Am^2Kg^{-1} $\pm$ 0.26 Am^2Kg^{-1} to the minimum at 3 T, 350 K of 1.859 Am^2Kg^{-1} $\pm$ 0.24 Am^2Kg^{-1} is seen. There are similar decreases across temperatures for all samples grown in the range 293 K to 523 K. Above 523 K there is no indication of a magnetic phase change. There is also variation in the saturation field for samples deposited in vacuum at different deposition

temperatures, figure 7.12.
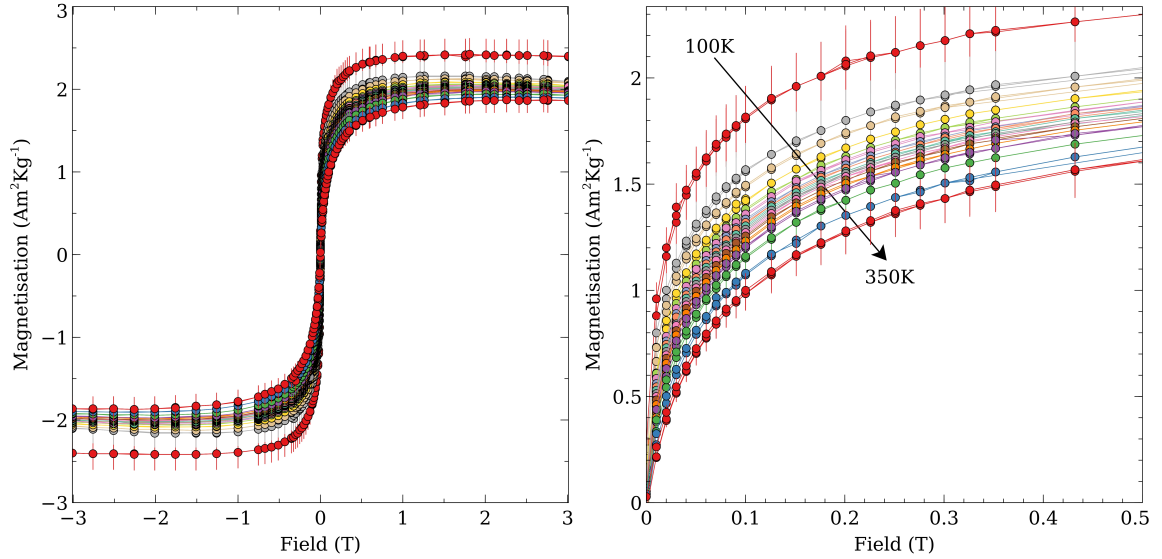
Figure 8.29: *(Left)isothermal measurements for a $La_1Fe_{1.895}Co_{0.91}Si_{1.105}$ thin film over a 100 K to 350 K range,(Right) isothermal measurements for a $La_1Fe_{1.895}Co_{0.91}Si_{1.105}$ thin film over a 100 K to 350 K range showing the virgin curve only.*

Samples deposited at both 293 K and 723 K have similar saturation fields, defined as the point at which an increase in the field does not increase the moment measured, for both 7 μTorr deposited, and 20 mTorr deposited samples. The samples grown in 20 mTorr have a linear relationship with the saturation field from 293 K to 723 K with a dip at 623 K, but the samples grown in a vacuum have a maximum saturation field point at 523 K before decreasing to the same point as vacuum grown at 723 K. Lollobrigida et al. show a saturation of $\sim 0.5\,T$ to $0.7\,T$ for $La(Fe_{0.9}Co_{0.015}Si_{0.085})_{13}$, meaning that all thin-film samples have an increased field required for saturation. Samples grown at 523 K under vacuum seemed promising for further research due to reduced coercivity, figure 7.13, however these samples also show the most significant increase in the saturation field, a

negative characteristic for real-world application.
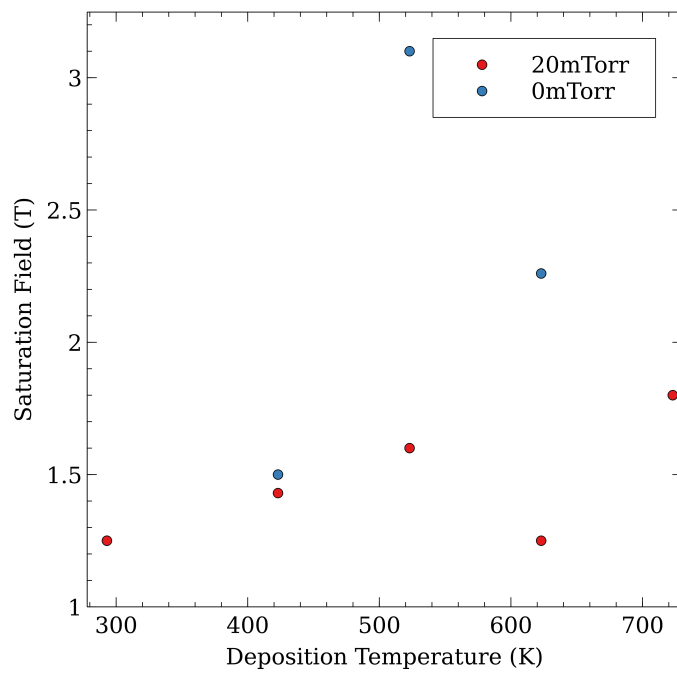
Figure 8.30: *Saturation field against deposition temperature for both 7 μTorr deposited and 20 mTorr Ar deposited samples. All saturation fields were for taken while in the low temperature ferromagnetic state.*

8.7.3 Magnetic Coercivity
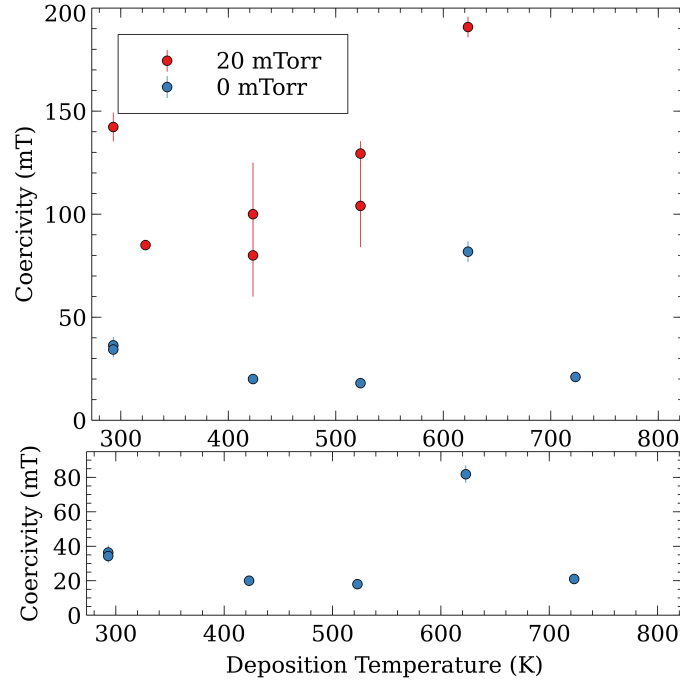
Figure 8.31: *(Top)Coercivity of $La_1Fe_{1.895}Co_{0.91}Si_{1.105}$ thin films against the deposition temperature used for both Vacuum and 20 mTorr Ar samples, (Bottom) Coercivity against deposition temperature for just the Vacuum grown samples.*

Despite the increased roughness seen for the $La_1Fe_{1.895}Co_{0.91}Si_{1.105}$ thin films grown in a 7 μTorr atmosphere, there is a significantly reduced coercivity for the entire deposition temperature used when compared to those grown in 20 mTorr Ar, figure 7.13. Samples deposited in both chamber pressures have a dip in the coercivity at deposition temperatures above room temperature, but the minimum in each doesn't coincide. Samples deposited at 20 mTorr have the lowest magnetic coercivity of 80 mT $\pm$ 21 mT when deposited at 423 K, whereas the samples deposited in a 7 μTorr atmosphere have a minimum at a higher temperature of 523 K and coercivity of 18 mT $\pm$ 1 mT.

141
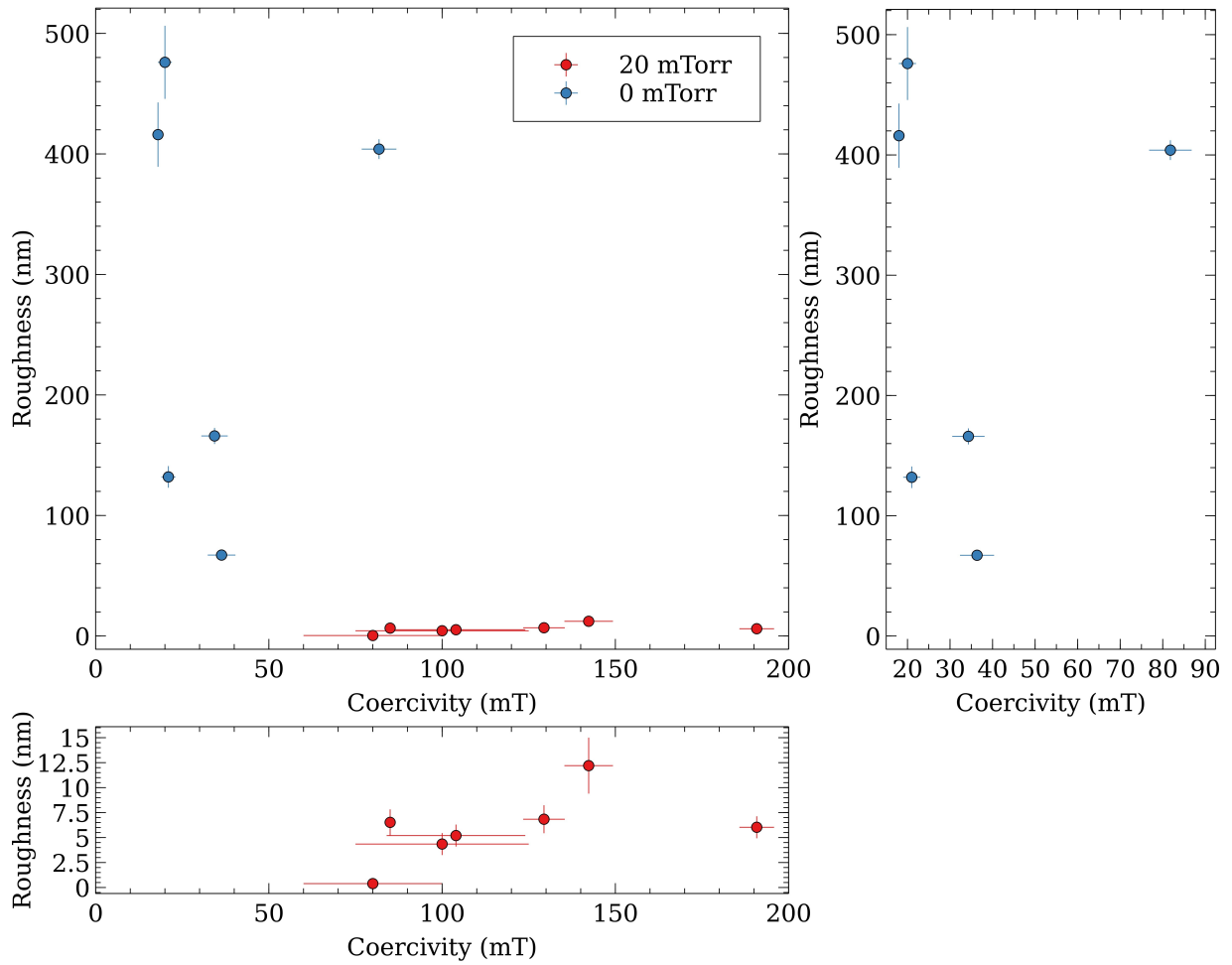
Figure 8.32: *(Left) Coercivity of $La_1Fe_{1.895}Co_{0.91}Si_{1.105}$ thin films against roughness for both Vacuum and 20 mTorr Ar samples, (Right) scaled down coercivity plot for just the Vacuum grown samples, (Bottom) scaled down roughness plot of just the 20 mTorr grown samples.*

Figures 7.14 and 7.15 show the coercivity relationship with surface roughness and grain size for both vacuum and 20 mTorr Ar grown samples. Unlike the surface roughness that correlates with the deposition temperature, the coercivity shows a stronger correlation with the deposition chamber pressure. This correlation would suggest that to optimise the $La_1Fe_{1.895}Co_{0.91}Si_{1.105}$ thin film growth (minimise both magnetic coercivity and surface roughness) an optimum temper-

ature and chamber pressure are needed. The optimum deposition temperature for reducing surface roughness is above the optimum temperature for reducing magnetic coercivity, however. Higher pressure also reduces the roughness but increases the coercivity. So there must be a trade-off considered for future growth.
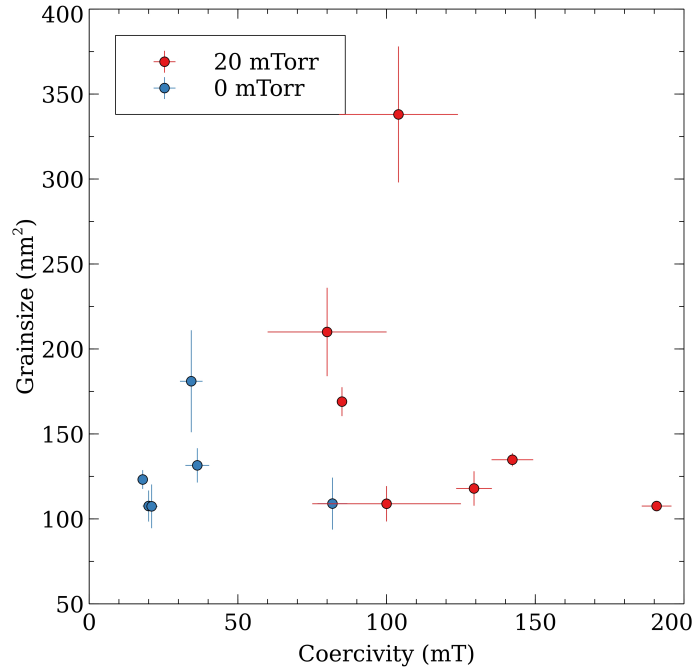
Figure 8.33: *Coercivity of $La_1Fe_{1.895}Co_{0.91}Si_{1.105}$ thin films against grain size for both Vacuum and 20 mTorr Ar samples.*

The bulk magnetic coercivity of LaFeCoSi while in the ferromagnetic state has been reported to be in the 10 mT [125] range. Thin-film samples appear to have a strong correlation between the deposition chamber pressure and the magnetic coercivity, with those deposited in a vacuum showing much lower coercivities in the 18mT to 37 mT range. While those deposited at a higher pressure show a significant coercivity increase, both 7 μTorr and 20mTorr deposited samples have coercivities higher than the bulk counterpart, making further thin film $La_1Fe_{1.895}Co_{0.91}Si_{1.105}$ studies less attractive. Despite this, as the first reported thin film $La_1Fe_{1.895}Co_{0.91}Si_{1.105}$, the scope for further research is still hugely

valid.

8.7.4 Entropy Change

Following the methods laid out previously for calculating the entropy change in a magnetocaloric material, our data shows a large peak in thin-film $La_1Fe_{1.895}Co_{0.91}$ $Si_{1.105}$ at 265 K, 18 K below the target used for deposition, figure 7.16. A smaller peak at 285 K is also visible but difficult to discern from the much larger at 265 K.
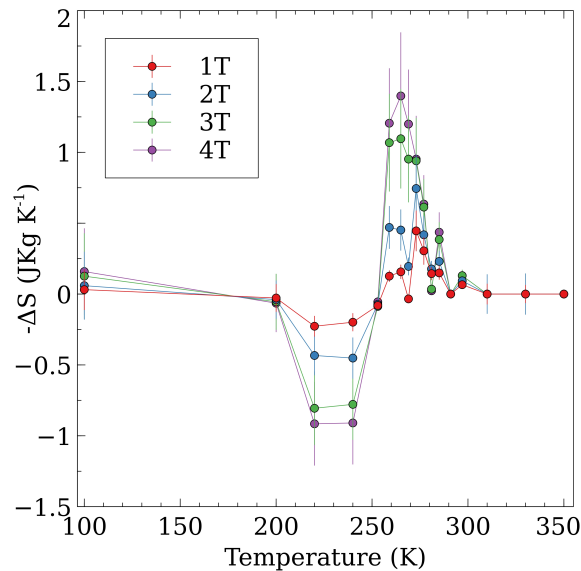
Figure 8.34: *Entropy Change as a function of temperature for a thin-film* $La_1Fe_{1.895}Co_{0.91}Si_{1.105}$ *sample grown at 523 K.*

Not present in the bulk target material is a negative entropy change in the thin film, present at temperatures 20 K to 40 K below the T_c. The origin of this negative entropy change is unknown, but with no reported counter part in bulk, it is likely from the physical size of the sample or the growth process. If the negative entropy change can be manipulated, similar to an inverse magnetocaloric effect, the process of growing thin film $La_1Fe_{11.06}Co_{0.86}Si_{1.08}$ could be used to further MCE materials in industrial applications and increase the operational

temperatures of $La_1Fe_{11.06}Co_{0.86}Si_{1.08}$. Bjørk et al. report a maximum entropy change for bulk $La_1Fe_{11.06}Co_{0.86}Si_{1.08}$ at 6.1 $JkgK^{-1}$ for a field change of 5 T. This value is significantly higher than found for thin films, $\sim \times 4$ higher after correcting for mass. As with the GdSiGe samples presented in chapter 6, This would point towards the destruction or diminishment of the FOPT like transition and the presence of a SOPT like instead.

Figure 7.16 shows the largest entropy change found for a thin film $La_1Fe_{11.06}$ $Co_{0.86}Si_{1.08}$ sample, figure 7.17 gives a comparison for a range of samples grown in 20 mTorr. There is a maximum entropy change when deposited at 523 K, with 20 mTorr at -1.394 $JkgK^{-1}$ $\pm$ 0.34 $JkgK^{-1}$ for a field change of 4 T. The negative entropy change is present in all samples grown. There is an increase in the entropy change with deposition temperature, despite the previously mentioned degradation expected for the higher temperature samples. Both 20 mTorr and vacuum deposited samples have minimal to no response when deposited above 523 K.
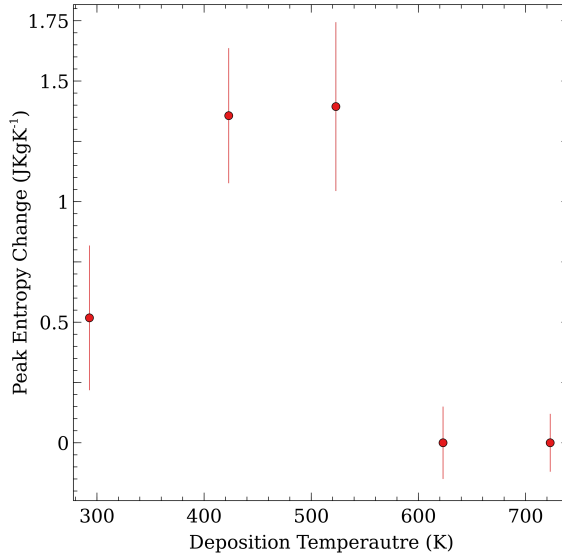
Figure 8.35: *Entropy change as a function of temperature for thin-film* $La_1Fe_{1.895}Co_{0.91}Si_{1.105}$.

8.7.5 Magnetic Hysteresis

For both 20 mTorr and 7 μTorr deposited samples on both Si/SiO_2 and AlN substrates, the coercivity measured below the transition is also present at higher temperatures above 300 K. Figure 7.18 shows the coercivity of two samples both on Si/SiO_2 and grown at 523 K but with different chamber pressures. Figure 7.18 datasets were both measured at 350 K, well above the transition point of $La_1Fe_{1.895}Co_{0.91}Si_{1.105}$.
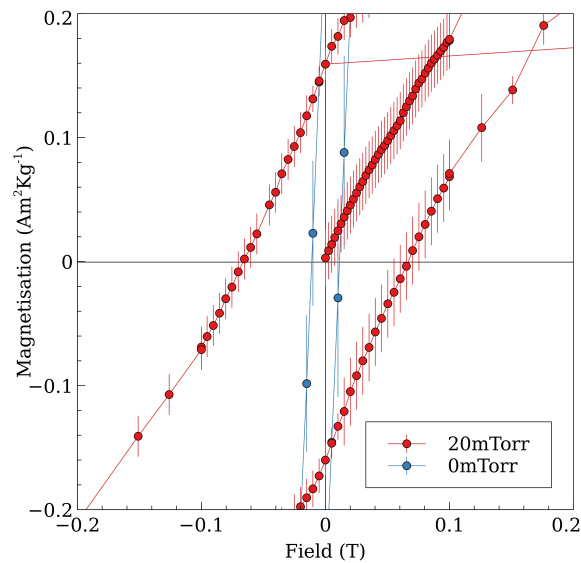
Figure 8.36: *Coercivity plots of two $La_1Fe_{1.895}Co_{0.91}Si_{1.105}$ samples both grown at 523 K in different chamber pressures.*

As $La_1Fe_{1.895}Co_{0.91}Si_{1.105}$ would be in its paramagnetic state above its T_c of 283 K, the ferromagnetic nature present in figure 7.18 would suggest there is secondary ferromagnetic phases present.

8.8 Structure

Structural analysis is performed using XRR and PNR as described in chapter 4. XRR and PNR are used to identify layer structures, densities and magnetic

properties.

8.8.1 Reflectometry; X-ray and Neutron

To investigate the roughness changes and surface/ interface effects X-Ray Reflectivity (XRR) measurements were taken and fitted using the GenX software. Fitting to XRR data, shown in figure 7.20 (left), describes a depth-dependent multi-layered system. Polarised neutron reflectometry (PNR) was also employed, figure 7.20 (right) to compare and gain an insight into the magnetism of the system. A table of the fitting results is given in table 7.1.

Fitting to both data sets of a $La_1Fe_{1.895}Co_{0.91}Si_{1.105}$ sample on SiO_2 substrate grown at 553 K gives a film of 50.3 nm with three distinct $La_1Fe_{1.895}Co_{0.91}Si_{1.105}$ layers. The surface layer being 10 nm thick is marginally less dense than the central layer, with a roughness of 0.659 and no magnetic moment. The second layer is the thickest at 30.3 nm. The third layer is 10.1 nm thick, and has a relatively high magnetic moment per atomic site. This system shows a thin film with multiple layers where most of the magnetic activity at room temperature seems to be focused in the layers closest to the interface and substrate while the surface region is relatively benign.

All depositions are performed in a single session with a constant laser, pressure and chamber gas used. This means that the multi-layered system has not formed from a conscious decision to create layers during deposition but rather has formed via some other unknown mechanism.

It should be noted that the top two layers are of a similar density, with the bottom two layers having a larger magnetic moment. The structure of the thin films is more likely to consist of several gradients between the layers as opposed to a hard interface system, with an increasing density and magnetic moment towards the substrate. This is likely due to inter-diffusion between the $La_1Fe_{1.895}Co_{0.91}Si_{1.105}$ material being deposited and the substrate, or alloying at

the substitute.
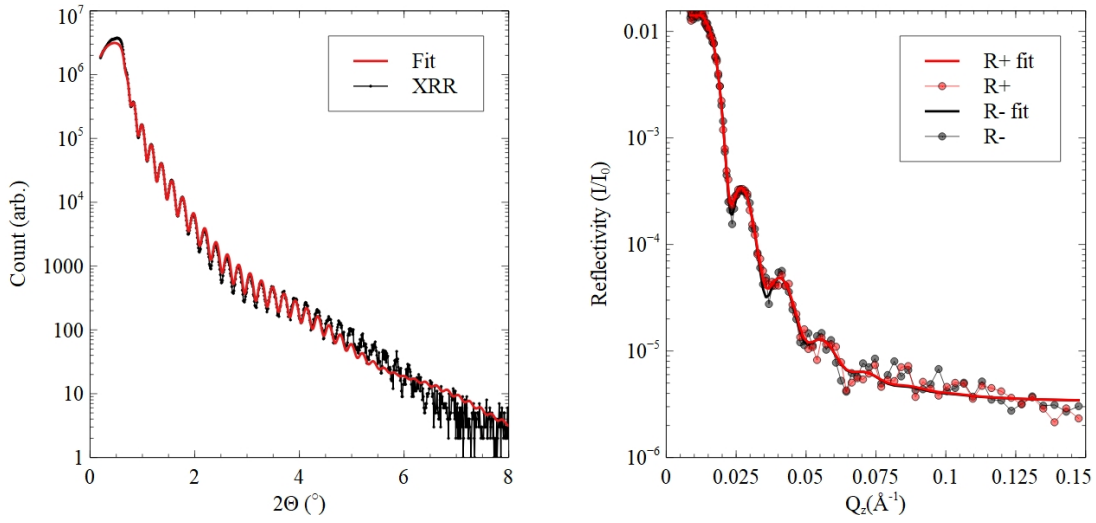
Figure 8.37: *(Left)XRR of thin film $La_1Fe_{1.895}Co_{0.91}Si_{1.105}$,(Right) PNR of the same $La_1Fe_{1.895}Co_{0.91}Si_{1.105}$ film.*

For the fitting parameters it is assumed that the stoichiometry of the LFS layers is $La_1Fe_{1.895}Co_{0.91}Si_{1.105}$. Fitting is also performed with a $LaFeSi(1:1:1)$ phase layer at the substrate interface and surface, but both provide a FOM an order of magnitude higher than when omitted.
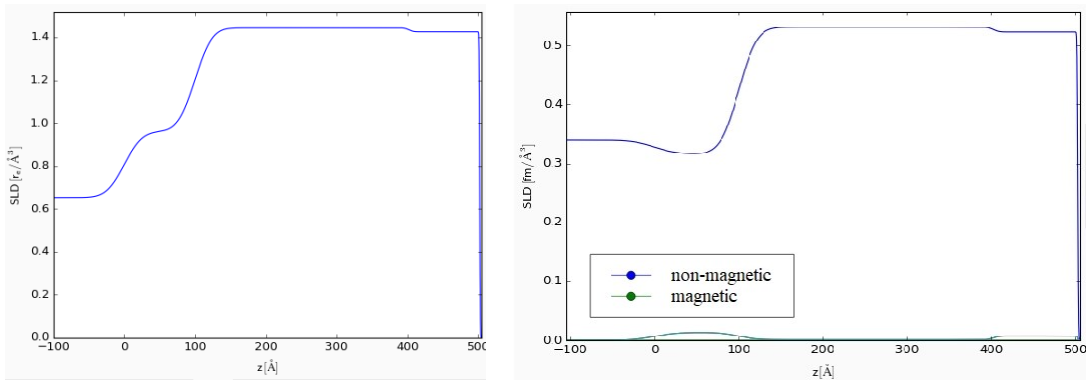
Figure 8.38: *(left) SLD for XRR data on the $La_1Fe_{1.895}Co_{0.91}Si_{1.105}$ sample, (right) SLD for PNR data on the $La_1Fe_{1.895}Co_{0.91}Si_{1.105}$ sample, in a 200 mT field.*

148

Table 8.2: Fitted values for XRR and PNR data of a $La_1Fe_{1.895}Co_{0.91}Si_{1.105}$ sample on SiO_2.

Layer	Parameter	Fitting Result
Amb	$\rho/at.\mathring{A}^{-1}$	
	R / $\mathring{A}$	
LFS Surface	D / $\mathring{A}$	100 ± 10.1
	$\rho/at.\mathring{A}^{-1}$	$4.1 \times 10^{-3} \pm 0.23 \times 10^{-3}$
	R / $\mathring{A}$	0.659 ± 0.1
	$M/\mu_B FU^{-1}$	0
LFS	D / $\mathring{A}$	303 ± 36.7
	$\rho/at.\mathring{A}^{-1}$	$4.16 \times 10^{-3} \pm 0.12 \times 10^{-3}$
	R / $\mathring{A}$	5 ± 0.15
	$M/\mu_B FU^{-1}$	$1.12 \times 10^{-2} \pm 0.21 \times 10^{-2}$
LFS Interface	D / $\mathring{A}$	101 ± 9.8
	$\rho/at.\mathring{A}^{-1}$	$2.47 \times 10^{-2} \pm 0.1 \times 10^{-2}$
	R / $\mathring{A}$	25.01 ± 0.98
	$M/\mu_B FU^{-1}$	$1.98 \times 10^{-2} \pm 0.23 \times 10^{-2}$
SiO_2	D / $\mathring{A}$	289 ± 12.1
	$\rho/at.\mathring{A}^{-1}$	$3.42 \times 10^{-3} \pm 0.21 \times 10^{-3}$
	R / $\mathring{A}$	16.04 ± 0.87
	$M/\mu_B FU^{-1}$	0
Si	$\rho/at.\mathring{A}^{-1}$	
	R / $\mathring{A}$	

8.9 Summary

Thin film $La_1Fe_{1.895}Co_{0.91}Si_{1.105}$ has been grown via PLD on SiO_2 and AlN substrates. AFM thickness and roughness measurements show the films are on the order of $\sim 35\ nm$ to $\sim 70\ nm$ and describe a relationship between the deposition chamber pressure, temperature coercivity, magnetic coercivity, and grain sizes.

Samples were deposited at 20mTorr Ar or in vacuum, in which the chamber reached pressures of 7 $\mu Torr$. Samples from both of these pressures show a distinct difference in their surface roughness, grain sizes and coercivity, with the lower pressure depositions having far lower coercivities. The difference in grain size from two different deposition pressures does not affect the samples roughness.

Magnetic measurements identify a gradient change close to room temperature and a peak change at temperatures lower than the bulk counterpart. Magnetic measurements also show a higher than expected magnetic moment above the T_c, where there is a slight increase in magnetisation above 300 K. Isofield measurements also show a spin glass-like effect at low temperature with a freezing point at $\sim 100\ K$.

Structural measurements show a complex change in the magnetisation as a function of depth for the thin films, with most of the magnetic activity at room temperature occurring near the interfaces and surfaces. There is little change in the density as a function of thickness.

When compared to bulk studies, thin film $La_1Fe_{1.895}Co_{0.91}Si_{1.105}$ shows an increased coercivity, which acts as a detriment for industrial applications. It also shows a negative entropy change not present in bulk samples at a lower temperature than the transition seen in equivalent bulk samples.

A significant reduction in the entropy change when compared to bulk also shows the destruction of the FOPT transition and the presence of a SOPT like transition in the same region.

8.9.1 Future Potential

Further investigation was planned to study the effect of strain on the samples. Piezoelectric PZT or BTO substrates pose an opportunity to investigate the magnetisation as a function of substrate strain. Multiple depositions on the same substrate of differing temperature, introducing Mn or Al-doped LaFeSi, different Fe/Co/Si ratios or other MCE materials was also planned and may introduce a cascading phase change effect within the sample. This could lead to an increased operating temperature range. As LaFeSi is an itinerant electron system there may prove to be an exciting interplay with other conductive systems and materials if deposited in contact with LaFeSi thin-films.

Further study into the working life cycle of thin-film $La_1Fe_{1.895}Co_{0.91}Si_{1.105}$ could provide a path to improving the longevity of the MCE. This indicates that investigating repeated phase changes as a function of time would be a useful next step.

As the first reported thin-film material from the LaFeSi family, there is much scope for further research in the thin film regime. More basic understanding of the structure and magnetism at this scale would be beneficial to future research.

<div align="right">

9

</div>

Conclusion

9.1 Summary of work

An Ising model using the RKKY interaction and a comparison between phases for a $Gd_5(Si_xGe_{1-x})_4$ structure has been developed to show the applicability to MCE materials. The model has shown success in the application to the FOPT material with rare-earth sites, predicting a similar T_c to that found experimentally. It also shows the effect of stress and strain on the T_c with stress inducing an increase in the T_c. Model sample purity has also been investigated, showing a further change in the T_c and the nature of the transition.

Thin film $Gd_5Si_2Ge_2$ has been grown via PLD on SiO_2 and AlN substrates

and maintains the MCE and phase transition. A gradient change in the magneti-sation against temperature is seen and has a peak close to room temperature and above that of bulk $Gd_5Si_2Ge_2$. Structural measurements also show the presence of secondary non-magnetocaloric magnetic phases. Further structural measurements of $Gd_5Si_2Ge_2$ show the presence of amorphous material and secondary phases, $Gd_2Ge_2O_7$ and $Gd_2Si_2O_7$. A bi-layer structure is also shown with the secondary phases mostly present in the lower layer.

The theorised optimal deposition temperature for $Gd_5Si_2Ge_2$ of 573 K, where the monoclinic phase is maximised, is shown to not be optimal experimentally, with a lower temperature at 503K being optimal for entropy change and lowering coercivity and surface roughness.

Thin film $La_1Fe_{1.895}Co_{0.91}Si_{1.105}$ has also been grown via PLD on SiO_2 and AlN substrates and also maintains the MCE and phase transition. AFM thickness and roughness measurements show the $La_1Fe_{1.895}Co_{0.91}Si_{1.105}$ films are on the order of $\sim 80nm$ and describe a relationship between the chamber pressure, temperature, grain size and coercivity. This means precise growth control and understanding is required to optimise the material. The chamber pressure is shown to have the most significant effect on the deposition of $La_1Fe_{1.895}Co_{0.91}$, but the temperature of the substrate has to be taken into account to optimise the film. The difference in grain size from deposition pressures does not have a significant effect on the samples magnetically, only the surface properties.

A gradient change in the magnetisation against temperature has a peak close to room temperature and below that of bulk $La_1Fe_{1.895}Co_{0.91}$. Measurements also show the presence of secondary non-magnetic phases. There also appears to be an increase in the magnetisation not present in bulk above 300 K. A spin glass like effect is also shown in the $La_1Fe_{1.895}Co_{0.91}$ samples with a freezing temperature at $\sim 100K$, a similar effect is not seen in the thin film $Gd_5Si_2Ge_2$.

XRR and PNR show the most magnetically active parts of the film are near the

153

interface and surface with little change in the density as a function of thickness.

9.2   Future work

The methods used in the simulations presented are focused on $Gd_5(Si_xGe_{1-x})_4$, but there is scope to investigate other rare earth and non-rare-earth based materials where the MCE is not driven by itinerant electrons. The methods used for simulation can be applied to other, yet to be investigated materials, reducing the already very high price of investigation in rare-earth based MC materials. The super-exchange interaction present in the bulk material could also be investigated using the simulation methods described.

For the $Gd_5Si_2Ge_2$ and $La_1Fe_{1.895}Co_{0.91}Si_{1.105}$ samples further investigation was planned to look at strain effects and compare to the simulation working using BTO and PZT substrates.

For the $Gd_5Si_2Ge_2$ and $La_1Fe_{1.895}Co_{0.91}Si_{1.105}$ samples further investigation could look at multiple layers with different materials or chamber conditions, to look at a cascading effect in thin films. Further simulations could also pre-emptively look into layering the values of E_{bond} to simulate multiple layers of $Gd_5(Si_xGe_{1-x})_4$ with varying values of x.

As FOPT materials experiencing a crystallographic phase change, there is a level of degradation with repeated cycles through the T_c that could also be investigated for thin films on both materials. As the MCE has a complex relationship with the itinerant electrons in $La_1Fe_{1.895}Co_{0.91}Si_{1.105}$, investigating the effect of deposition onto a conductive material could prove interesting in affecting the MC response.

References

[1] J.-D. Zou, "Magnetocaloric and barocaloric effects in a Gd 5 Si 2 Ge 2 compound Magnetocaloric and barocaloric effects in a Gd 5 Si 2 Ge 2 compound *," *Chinese Phys. B Phys. B1Q*, vol. 21, no. 3, 2012. [Online]. Available: http://iopscience.iop.org/1674-1056/21/3/037503

[2] S. Kobe, B. Podmilj, P. J. Mcguiness, and M. Komelj, *CMAs as Magnetocaloric Materials.* Wiley-VCH, 2011.

[3] V. K. Pecharsky and K. A. Gschneidner, Jr., "Giant Magnetocaloric Effect in Gd5Si2Ge2," *Physical Review Letters*, vol. 78, no. 23, pp. 4494–4497, 1997. [Online]. Available: http://journals.aps.org/prl/pdf/10.1103/PhysRevLett.78.4494http://link.aps.org/doi/10.1103/PhysRevLett.78.4494

[4] V. Franco, J. Blázquez, B. Ingale, and A. Conde, "The Magnetocaloric Effect and Magnetic Refrigeration Near Room Temperature: Materials and Models," *Annual Review of Materials Research*, vol. 42, no. 1, pp. 305–342, 2012.

[5] R. L. Hadimani, J. H. B. Silva, A. M. Pereira, D. L. Schlagel, T. A. Lograsso, Y. Ren, X. Zhang, D. C. Jiles, J. P. Araújo, and J. P. Araujo, "Gd5(Si,Ge)4 thin film displaying large magnetocaloric and strain effects

155

due to magnetostructural transition," *Applied Physics Letters*, vol. 106, no. 3, 2015.

[6] "POLREF." [Online]. Available: https://www.isis.stfc.ac.uk/Pages/polref. aspx

[7] W. Choe, V. K. Pecharsky, A. O. Pecharsky, K. A. Gschneidner, V. G. Young, and G. J. Miller, "Making and breaking covalent bonds across the magnetic transition in the giant magnetocaloric material Gd5(Si2Ge2)," *Physical Review Letters*, vol. 84, no. 20, pp. 4617–4620, 2000.

[8] V. Pecharsky and K. Gschneidner, "Phase relationships and crystallography in the pseudobinary system Gd5Si4Gd5Ge4," *Journal of Alloys and Compounds*, vol. 260, no. 1, pp. 98–106, 1997. [Online]. Available: http://www.sciencedirect.com/science/article/pii/S0925838897001436

[9] Y. Mozharivskyj, A. O. Pecharsky, V. K. Pecharsky, and G. J. Miller, "On the High-Temperature Phase Transition of Gd5Si2Ge2 On the High-Temperature Phase Transition of Gd 5 Si 2 Ge 2," *J. AM. CHEM. SOC.*, vol. 127, pp. 317–324, 2005. [Online]. Available: http://lib.dr.iastate.edu/chem_pubshttp://lib.dr.iastate.edu/

[10] J. Lyubina, "Magnetocaloric materials," *Springer Series in Materials Science*, vol. 231, pp. 115–186, 2016.

[11] T. Gottschall, A. Gràcia-Condal, M. Fries, A. Taubel, L. Pfeuffer, L. Mañosa, A. Planes, K. P. Skokov, and O. Gutfleisch, "A multicaloric cooling cycle that exploits thermal hysteresis," *Nature Materials*, vol. 17, no. 10, pp. 929–934, 2018. [Online]. Available: http://dx.doi.org/10.1038/ s41563-018-0166-6http://www.nature.com/articles/s41563-018-0166-6

[12] Y. Liu, L. C. Phillips, R. Mattana, M. Bibes, A. Barthélémy, and B. Dkhil, "Large reversible caloric effect in FeRh thin films via a dual-

stimulus multicaloric cycle," *Nature Communications*, vol. 7, p. 11614, 2016. [Online]. Available: https://www.nature.com/articles/ncomms11614. pdfhttp://www.nature.com/doifinder/10.1038/ncomms11614

[13] E. Warburg, "Magnetische Untersuchungen," *Annalen der Physik*, vol. 249, no. 5, pp. 141–164, 1881. [Online]. Available: http://doi.wiley.com/10.1002/andp.18812490510

[14] P. Debye, "Einige Bemerkungen zur Magnetisierung bei tiefer Temperatur," *Annalen der Physik*, vol. 386, no. 25, pp. 1154–1160, 1926. [Online]. Available: http://doi.wiley.com/10.1002/andp.19263862517

[15] W. F. Giauque and C. W. Clark, "The conditions for producing temperatures below 1 absolute by demagnetization of Gd2(SO4)32O. Temperature-magnetic field isentropics," *The Journal of the American Chemical Society*, vol. 54, no. 8, pp. 3135–3150, 1932.

[16] G. V. Brown, "Magnetic heat pumping near room temperature Tunable magnetic regenerator alloys with a giant magnetocaloric effect for magnetic refrigeration from 20 to 290 K Magnetic heat pumping near room temperature," *Journal of Applied Physics*, vol. 471, no. 10, 1976. [Online]. Available: http://dx.doi.org/10.1063/1.323176

[17] L.-W. Li, "Review of magnetic properties and magnetocaloric effect in the intermetallic compounds of rare earth with low boiling point metals," *Chinese Physics B*, vol. 25, no. 3, p. 037502, mar 2016. [Online]. Available: http://stacks.iop.org/1674-1056/25/i=3/a=037502?key=crossref.86339e3aa4295d7ab0b8b1bc6a9520df

[18] S. Jacobs, J. Auringer, A. Boeder, J. Chell, L. Komorowski, J. Leonard, S. Russek, and C. Zimm, "The performance of a large-scale rotary magnetic

refrigerator," in *International Journal of Refrigeration*, vol. 37, no. 1, 2014, pp. 84–91.

[19] J. Y. Law, V. Franco, P. Keblinski, and R. V. Ramanujan, "Active transient cooling by magnetocaloric materials," *Applied Thermal Engineering*, vol. 52, no. 1, pp. 17–23, 2013.

[20] A. Noume, M. Risser, and C. Vasile, "Modeling of a Magnetocaloric System for Electric Vehicles," in *2013 COMSOL Conference in Rotterdam*, 1998, pp. 1–6.

[21] E. Palacios, J. A. Rodríguez-Velamazán, G. F. Wang, R. Burriel, G. Cuello, and J. Rodríguez-Carvajal, "Magnetic structure of Gd5Si2Ge2 and Gd5Si2Ge1.9M0.1 (M = Ga, Cu)." *Journal of physics. Condensed matter : an Institute of Physics journal*, vol. 22, no. 44, p. 446003, oct 2010. [Online]. Available: http://stacks.iop.org/0953-8984/22/i=44/a=446003?key=crossref.5fb82e67e5a48e49e73be7af23964977http://www.ncbi.nlm.nih.gov/pubmed/21403359

[22] R. L. Hadimani, I. C. Nlebedim, Y. Melikhov, and D. C. Jiles, "Growth and characterisation of Gd5(SixGe 1-x)4 thin film," *Journal of Applied Physics*, vol. 113, no. 17, 2013.

[23] Z. X. Zhang Hehe, Qian Mingfang, "Magnetocaloric effect of Ni-Fe-Mn-Sn microwires prepared by melt-extraction technique," *Materials Design*, vol. 10, no. 1016, 2016.

[24] V. F. Petrenko and R. W. Whitworth, *Physics of Ice.* Oxford, 1999.

[25] K. Morrison, J. D. Moore, K. G. Sandeman, A. D. Caplin, and L. F. Cohen, "Capturing first- and second-order behavior in magnetocaloric CoMnSi0.92 Ge0.08," *Physical Review B - Condensed Matter and Materials Physics*, vol. 79, no. 13, pp. 1–5, 2009.

[26] K. A. Gschneider Jr., V. K. Pecharsky, and A. O. Tsokol, "Recent developments in magnetocaloric materials," *Reports on Progress in Physics*, vol. 68, no. 6, pp. 1479–1539, 2005. [Online]. Available: http://magnetocaloric.web.ua.pt/files/rpp5_6_R04.pdf

[27] A. Smith, K. K. Nielsen, and C. R. H. Bahl, "Scaling and universality in magnetocaloric materials," *Physical Review B - Condensed Matter and Materials Physics*, vol. 90, no. 10, 2014.

[28] S. El-showk, M. F. Paulos, and D. Poland, "Solving the 3D Ising Model with the Conformal Bootstrap," *Physics*, no. March, 2012. [Online]. Available: https://arxiv.org/pdf/1203.6064.pdf

[29] N. Bohr, *II. The doctor's dissertation (Text and Translation)*. Elsevier, 1911, vol. 1, no. C.

[30] Y. T. Toru Moriya, "Itinerant Electron Magnetism 13," *Material Science Annual Review*, vol. 16, no. 14, pp. 1–25, 1984.

[31] S. Blundell, *Magnetism in Condensed Matter*, 1st ed. Oxford Press, 2001.

[32] J. Lyubina, "Magnetocaloric materials for energy efficient cooling," *Journal of Physics D: Applied Physics*, vol. 50, no. 5, p. 053002, 2017. [Online]. Available: http://stacks.iop.org/0022-3727/50/i=5/a=053002?key=crossref.dfb84d1b7d0ad20592a3a2082e3755f2

[33] L. T. Kuhn, N. Pryds, C. R. H. Bahl, and A. Smith, "Magnetic refrigeration at room temperature – from magnetocaloric materials to a prototype," *Journal of Physics: Conference Series*, vol. 303, no. 1, p. 12082, 2011. [Online]. Available: http://iopscience.iop.org/1742-6596/303/1/012082http://stacks.iop.org/1742-6596/303/i=1/a=012082

[34] P. W. Ma and S. L. Dudarev, "Dynamic magnetocaloric effect in bcc iron and hcp gadolinium," *Physical Review B - Condensed Matter and Materials Physics*, vol. 90, no. 2, 2014.

[35] M. Krautz, J. D. Moore, K. P. Skokov, J. Liu, and C. S. Teixeira, "Reversible solid-state hydrogen-pump driven by magnetostructural transformation in the prototype system La (Fe , Si) 13Hy Reversible solid-state hydrogen-pump driven by magnetostructural transformation in the prototype system La (Fe , Si) 13 H y," *Journal of Applied Physics*, vol. 083918, no. 083918, 2012. [Online]. Available: http://dx.doi.org/10.1063/1.4759438http://aip.scitation.org/toc/jap/112/8

[36] Y. Shao, J. Liu, M. Zhang, A. Yan, K. P. Skokov, D. Y. Karpenkov, and O. Gutfleisch, "High-performance solid-state cooling materials: Balancing magnetocaloric and non-magnetic properties in dual phase La-Fe-Si," *Acta Materialia*, vol. 125, pp. 506–512, 2017.

[37] K. G. Sandeman, "Magnetocaloric materials: The search for new systems," pp. 566–571, 2012.

[38] L. Caron, Z. Q. Ou, T. T. Nguyen, D. T. C. Thanh, O. Tegus, and E. B. Uck, "On the determination of the magnetic entropy change in materials with first-order transitions," *Journal of Magnetism and Magnetic Materials*, vol. 321, pp. 3559–3566, 2009.

[39] C. P. Bean and D. S. Rodbell, "Magnetic disorder as a first-order phase transformation," *Physical Review*, vol. 126, no. 1, pp. 104–115, 1962. [Online]. Available: http://journals.aps.org/pr/pdf/10.1103/PhysRev.126.104

[40] H. Kramers, "L'interaction Entre les Atomes Magnétogènes dans un Cristal Paramagnétique," *Physica*, vol. 1, pp. 1–6, 1934.

160

[41] C. Zener, "Interaction between the d-Shells in the Transition Metals. II. Ferromagnetic Compounds of Manganese with Perovskite Structure," *Phys. Rev.*, vol. 82, p. 403, 1951.

[42] S. Power and M. Ferreira, "Indirect Exchange and Ruderman–Kittel–Kasuya–Yosida (RKKY) Interactions in Magnetically-Doped Graphene," *Crystals*, vol. 3, no. 1, pp. 49–78, 2013. [Online]. Available: http://www.mdpi.com/2073-4352/3/1/49/

[43] N. Boccara, *Symétries brisées : théorie des transitions avec paramètre d'ordre*, 1974.

[44] W. Janke, *Monte Carlo Methods in Classical Statistical Physics*, 2008.

[45] N. Metropolis, A. W. Rosenbluth, M. N. Rosenbluth, A. H. Teller, and E. Teller, "Equation of state calculations by fast computing machines," *The Journal of Chemical Physics*, vol. 21, no. 6, pp. 1087–1092, 1953.

[46] Y. Yuksel, U. Akinci, and E. Vatansever, "Influence of modified surface effects on the magnetocaloric properties of ferromagnetic thin films," *Thin Solid Films*, 2017.

[47] K. Karlova, J. Strecka, and J. Richter, "Enhanced magnetocaloric effect in the proximity of magnetization steps and jumps of spin-1/2 XXZ Heisenberg regular polyhedra," *J. Phys.: Condens. Matter*, vol. 29, 2017. [Online]. Available: http://iopscience.iop.org/0953-8984/29/12/125802

[48] T. Lei, K. Engelbrecht, and K. K. Nielsen, "Spatially resolved modelling of inhomogeneous materials with a first order magnetic phase transition," *J. Phys. D: Appl. Phys*, vol. 50, no. 414002, 2017. [Online]. Available: http://iopscience.iop.org/article/10.1088/1361-6463/aa86e2/pdf

[49] V. V. Sokolovskiy, V. D. Buchelnikov, M. A. Zagrebin, A. Grnebohm, and P. Entel, "Predictions of a Large Magnetocaloric Effect in Co- and Cr-Substituted Heusler Alloys Using First-Principles and Monte Carlo Approaches," *Physics Procedia*, vol. 75, pp. 1381–1388, 2015.

[50] A. Malakis, P. Kalozoumis, and N. G. Fytas, "Continuous- and first-order phase transitions in ising antiferromagnets with next-nearest- neighbour interactions," *Rev. Adv. Mater. Sci.*, vol. 14, pp. 1–10, 2007. [Online]. Available: http://www.ipme.ru/e-journals/RAMS/no_11407/malakis.pdf

[51] A. Herrero, A. Oleaga, P. Manfrinetti, A. Provino, and A. Salazar, "Critical behavior of the ferromagnetic transition in GdSc(Si,Ge) intermetallic compounds," *Intermetallics*, vol. 101, no. May, pp. 64–71, 2018. [Online]. Available: https://doi.org/10.1016/j.intermet.2018.07.011

[52] J. Liu, "Optimizing and fabricating magnetocaloric materials," *Chinese Physics B*, vol. 23, no. 4, p. 047503, apr 2014. [Online]. Available: http://stacks.iop.org/1674-1056/23/i=4/a=047503?key=crossref.82b565c2b289c037265f80b89b5d9ee6

[53] A. O. V K Pecharsky and K. A. Gschneidner, "The giant magnetocaloric effect of optimally prepared Tunable magnetic regenerator alloys with a giant magnetocaloric effect for magnetic refrigeration from 20 to 290 K The giant magnetocaloric effect of optimally prepared Gd 5 Si 2 Ge 2," *Journal of Applied Physics Journal of Applied Physics*, vol. 93, no. 10, 2003. [Online]. Available: http://dx.doi.org/10.1063/1.1558210

[54] R. D. Shull, V. Provenzano, A. J. Shapiro, A. Fu, M. W. Lufaso, J. Karapetrova, G. Kletetschka, and V. Mikula, "The effects of small metal additions (Co, Cu, Ga, Mn, Al, Bi, Sn) on the magnetocaloric properties of the Gd5Ge2Si2 alloy," *J. Appl. Phys.*, vol. 99, no. 8, 2006.

162

[Online]. Available: http://digitalcommons.unf.edu/achm_facpubhttp://digitalcommons.unf.edu/achm_facpub/9

[55] R. S. V. Provenzano, A. Shapiro, "Reduction of hysteresis losses in the magnetic refrigerant Gd5Ge2Si2 by the addition of Iron," *Nature*, vol. 429, pp. 853–857, 2003.

[56] V. Provenzano, A. J. Shapiro, and R. D. Shull, "Reduction of hysteresis losses in the magnetic refrigerant Gd 5 Ge 2 Si 2 by the addition of iron," *Nature*, vol. 429, 2004.

[57] F.-x. Hu, B.-g. Shen, J.-r. Sun, Z.-h. Cheng, G.-h. Rao, and X.-x. Zhang, "Influence of negative lattice expansion and metamagnetic transition on magnetic entropy change in the compound LaFe 11 . 4 Si 1 . 6 Influence of negative lattice expansion and metamagnetic transition," *Applied Physics Letters*, vol. 3675, no. 2001, pp. 21–24, 2009.

[58] P. Company, O. Luboratorium, and R. Instituut, "Study of the Critical Behaviour of the Magnetization," *Journal of Magnetism and Magnetic Materials*, vol. 36, pp. 290–296, 1983.

[59] B. B. G. Shen, J. R. Sun, F. X. Hu, H. W. Zhang, and Z. H. Cheng, "Recent Progress in Exploring Magnetocaloric Materials," *Advanced Materials*, vol. 21, pp. 4545–4564, 2009.

[60] N. A. De Oliveira, P. J. Von Ranke, and A. Troper, "Magnetocaloric and barocaloric effects: Theoretical description and trends," in *International Journal of Refrigeration*, vol. 37, no. 1, 2014, pp. 237–248.

[61] F.-x. Hu, B.-g. Shen, J.-r. Sun, Z.-h. Zhang, and Cheng† and Xi-xiang, "Magnetic entropy change in La(Fe0.98Co0.02)11.7Al1.3," *J. Phys.: Condens. Matter*, vol. 12, 2000.

[62] K. Morrison, P. S.M., Y. V. Shcherbakova, A. Caplin, and L. Cohen, "Effect of Al substitution on the magnetocaloric properties of Ni-Co-Mn-Sn multifunctional alloys," *Intermetallics*, vol. 119, 2020.

[63] A. Yan, K. Müller, O. Gutfleisch, A. Yan, K. Müller, and O. Gutfleisch, "Structure and magnetic entropy change of melt-spun La Fe 11 . 57 Si 1 . 43 ribbons," *Journal of Applied Physics*, vol. 036102, no. 2005, pp. 2003–2006, 2010.

[64] X. B. Liu, X. D. Liu, and Z. Altounian, "Phase formation and magnetocaloric effect in rapidly quenched La (Fe 1 x Co x) 11 . 4 Si 1 . 6 Phase formation and magnetocaloric effect in rapidly quenched," *Journal of Applied Physics*, vol. 113904, no. 2005, pp. 10–14, 2010.

[65] J. Lyubina, O. Gutfleisch, M. D. Kuz, and M. Richter, "Journal of Magnetism and Magnetic Materials La (Fe , Si) 13 - based magnetic refrigerants obtained by novel processing routes ," *Journal of Magnetism and Magnetic Materials*, $vol.321, pp.3571 - -3577, 2009$.

[66] J. Lyubina, "magnetic cooling (invited) Recent advances in the microstructure design of materials for near room temperature magnetic cooling (invited)," *Journal of Applied Physics*, vol. 902, 2011.

[67] J. Lyubina, K. Nenkov, L. Schultz, and O. Gutfleisch, "Multiple metamagnetic transitions in the magnetic refrigerant La(Fe,Si)13Hx," *Physical Review Letters*, vol. 101, no. 17, 2008. [Online]. Available: http://journals.aps.org/prl/pdf/10.1103/PhysRevLett.101.177203

[68] B. Rosendahl, L. T. Kuhn, C. R. H. Bahl, M. Lundberg, C. Anconatorres, and M. Katter, "Journal of Magnetism and Magnetic Materials Properties of magnetocaloric La (Fe , Co , Si) 13 produced by

powder metallurgy," *Journal of Magnetism and Magnetic Materials*, vol. 322, no. 21, pp. 3447–3454, 2010. [Online]. Available: http://dx.doi.org/10.1016/j.jmmm.2010.06.043

[69] A. Barcza, M. Katter, V. Zellmann, S. Russek, S. Jacobs, C. Zimm, V. Gmbh, and C. Kg, "Stability and Magnetocaloric Properties of Sintered La(Fe, Mn, Si) H Alloys," *IEEE Transactions on Magnetics*, vol. 47, no. 10, pp. 3391–3394, 2011.

[70] K. Morrison, J. Lyubina, J. D. Moore, A. D. Caplin, K. G. Sandeman, O. Gutfleisch, and L. F. Cohen, "Erratum: Contributions to the entropy change in melt-spun LaFe 11.6Si 1.4 (Journal of Physics D: Applied Physics (2010) 43 (132001))," *Journal of Physics D: Applied Physics*, vol. 45, no. 17, 2012.

[71] J. Herrero-Albillos, D. Paudyal, F. Bartolomé, L. M. García, V. K. Pecharsky, K. A. Gschneidner, A. T. Young, N. Jaouen, and A. Rogalev, "Interplay between Er and Co magnetism in Interplay between Er and Co magnetism in ErCo 2," *Journal of Applied Physics*, vol. 103, pp. 7–146, 2008. [Online]. Available: http://dx.doi.org/10.1063/1.2836714http://aip.scitation.org/toc/jap/103/7

[72] N. K. Singh, K. G. Suresh, A. K. Nigam, S. K. Malik, A. A. Coelho, and S. Gama, "Itinerant electron metamagnetism and magnetocaloric effect in RCo2-based Laves phase compounds," pp. 68–79, 2007.

[73] M.-H. H. Phan and S.-C. C. Yu, "Review of the magnetocaloric effect in manganite materials," *Journal of Magnetism and Magnetic Materials*, vol. 308, no. 2, pp. 325–340, jan 2007.

[74] S. C. Paticopoulos, R. Caballero-Flores, V. Franco, J. S. Blázquez, A. Conde, K. E. Knipling, and M. A. Willard, "Enhancement of the magne-

tocaloric effect in composites: Experimental validation," *Solid State Communications*, vol. 152, no. 16, pp. 1590–1594, 2012.

[75] D. D. Belyea, T. S. Santos, and C. W. Miller, "Magnetocaloric effect in epitaxial La0.56Sr0.44MnO3 alloy and digital heterostructures," *Journal of Applied Physics*, vol. 111, no. 7, p. 07A935, 2012. [Online]. Available: http://scitation.aip.org/content/aip/journal/jap/111/7/10.1063/1.3677670

[76] C. W. Miller, D. V. Williams, N. S. Bingham, and H. Srikanth, "Magnetocaloric effect in Gd/W thin film heterostructures," in *Journal of Applied Physics*, vol. 107, no. 9, 2010, pp. 9–903.

[77] A. L. Pires, J. H. Belo, I. T. Gomes, A. M. L. Lopes, J. P. Araújo, A. M. Pereira, R. L. Hadimani, D. C. Jiles, R. L. Hadimani, D. L. Schlagel, T. A. Lograsso, D. C. Jiles, and T. A. Lograsso, "Suppression of magnetostructural transition on GdSiGe thin film after thermal cyclings," *Thin Solid Films*, vol. 621, pp. 247–252, 2017. [Online]. Available: http://dx.doi.org/10.1016/j.tsf.2016.09.013

[78] D. Doblas, L. M. Moreno-Ramírez, V. Franco, A. Conde, A. V. Svalov, and G. V. Kurlyandskaya, "Nanostructuring as a procedure to control the field dependence of the magnetocaloric effect," *Materials Design*, 2016.

[79] X. Hou, P. Lampen-kelley, Y. Xue, C. Liu, and H. Xu, "Formation mechanisms of NaZn 13 -type phase in giant magnetocaloric La e Fe e Si compounds during rapid solidi fi cation and annealing," *Journal of Alloys and Compounds*, vol. 646, pp. 503–511, 2015. [Online]. Available: http://dx.doi.org/10.1016/j.jallcom.2015.05.173

[80] D. T. Morelli, "Magnetocaloric properties of doped lanthanum manganite films," *Journal of Applied Physics*, vol. 79, p. 373, 1996.

[81] J. Debnath, J. H. Kim, and Y. Heo, "Correlation between structural parameters and the magnetocaloric effect in epitaxial La0.8Ca0.2MnO3/LaAlO3 thin film," *Journal of Applied Physics*, vol. 113, no. 063508, 2013.

[82] M. X, L. Hueso, and F. Maccherozzi, "Giant and reversible extrinsic magnetocaloric effects in La0.7Ca0.3MnO3 films due to strain," *Nature Materials*, vol. 12, pp. 52–58, 2012.

[83] N. R. Checca, W. S. Torres, M. A. V. Heringer, D. R. Sanchez, A. Rossi, M. S. Reis, and D. L. Rocco, "AC," *Journal of Alloys and Compounds*, 2019. [Online]. Available: https://doi.org/10.1016/j.jallcom.2019.06.238

[84] E. Ising, "Beitrag zur Theorie des Ferromagnetismus D." *Z. Phys.*, no. 4, pp. 253–258, 1924.

[85] W. Lenz, "Beitrag zum Verstandnis der magnetischen Erscheinunge in festen Korpern," *Phys. Z.*, vol. 21, pp. 613–615, 1920.

[86] L. Onsager, "Crystal Statistics. I. A Two-Dimensional Model with an Order-Disorder Transition," *Physical Review*, vol. 65, no. 3, pp. 117–149, 1943.

[87] W. L. Bragg and W. J. Williams, "The Effect of Thermal Agitation on Atomic Arrangement in Alloys — II," *Proc. Royal Soc. A5*, vol. 145, no. 1934, pp. 540–566, 1935.

[88] C. N. Yang and T. D. Lee, "Statistical Theory of Equations of State and Phase Transitions. I. Theory of Condensation," *Physical Review*, vol. 87, no. 3, pp. 404–409, 1952.

[89] H. W. Huang, "Hydrodynamic solution of the timedependent Ising model," *J. Chem. Phys*, vol. 70, no. 05, pp. 2390–2392, 1979.

[90] E. W. Montroll and N. S. Goel, "Denaturation and Renaturation of DNA." *Biopolymers*, vol. 4, pp. 855–878, 1966.

[91] M. L. Frazier, J. R. Wright, A. Pokorny, and P. F. F. Almeida, "Investigation of Domain Formation in Sphingomyelin / Cholesterol / POPC Mixtures by Fluorescence Resonance Energy Transfer and Monte Carlo Simulations," *Biophysical Journal*, vol. 92, no. 7, pp. 2422–2433, 2007. [Online]. Available: http://dx.doi.org/10.1529/biophysj.106.100107

[92] M. Hohnisch, S. Pittnauer, S. Solomon, and D. Stauffer, "Socioeconomic interaction and swings in business confidence indicators," *Physica A: Statistical Mechanics and its Applications*, vol. 345, pp. 646–656, 2005.

[93] M. Jabrane, M. Youssef, E. Hafidi, and M. E. Hafidi, "Magnetocaloric Properties of Gd 5 Si 2 Ge 2 Alloy : Monte Carlo Simulation Study," *Journal of Superconductivity and Novel Magnetism*, no. I, pp. 2–10, 2019.

[94] G. D. Samolyuk and V. P. Antropov, "Exchange coupling in pure hcp Gd and magnetostructural transition in Gd 5(Si 2Ge 2)," *Journal of Applied Physics*, vol. 97, no. 10, pp. 2003–2006, 2005.

[95] A. Ikeda and H. Kawamura, "Monte Carlo study of the ordering of the pyrochlore Ising model with the long-range RKKY interaction," *Journal of Physics: Conference Series*, vol. 145, pp. 1–9, 2009.

[96] D. Comtesse, M. E. Gruner, M. Ogura, V. V. Sokolovskiy, V. D. Buchelnikov, A. Gr, R. Arr, and N. Singh, "First-principles calculation of the instability leading to giant inverse magnetocaloric effects," *Physical Review B*, vol. 184403, pp. 1–6, 2014.

[97] K. Szalowski, T. Balcerzak, and A. Boba, "Journal of Magnetism and Magnetic Materials Thermodynamic properties of a diluted Heisenberg ferro-

magnet with interaction anisotropy — Magnetocaloric point of view," *Journal of Magnetism and Magnetic Materials*, vol. 323, pp. 2095–2102, 2011.

[98] Ü. Akıncı, "Hysteresis behaviors of the crystal field diluted general spin-S Ising model," *Physics Letters, Section A: General, Atomic and Solid State Physics*, vol. 381, no. 38, pp. 3258–3265, 2017. [Online]. Available: http://dx.doi.org/10.1016/j.physleta.2017.08.023

[99] H. N. Motlagh and G. Rezaei, "Monte Carlo simulation of magnetic properties of mixed spin (3/2, 1) ferromagnetic and ferrimagnetic disordered binary alloys with amorphous structure," *Journal of Magnetism and Magnetic Materials*, vol. 445, pp. 26–36, 2018.

[100] O. Mouritsen and S. Knak Jensen, "First-order phase transitions of Ising models with multispin interactions," *Physical Review B*, vol. 23, no. 3, pp. 976–979, 1981.

[101] P. R. Willmott and J. R. Huber, "Pulsed laser vaporization and deposition," *Reviews of Modern Physics*, vol. 72, no. 1, pp. 315–328, 2000.

[102] R. Eason, *Pulsed Laser Deposition of Thin Films*, 2007, no. 1.

[103] N. Debelo, F. Dejene, K. Roro, M. Pricilla, and C. Oliphant, "The effect of argon gas pressure on structural, morphological and photoluminescence properties of pulsed laser deposited KY 3F10:Ho3+ thin films," *Applied Physics A: Materials Science and Processing*, vol. 122, no. 6, 2016.

[104] S. N. Sambandam, B. Bethala, D. K. Sood, and S. Bhansali, "Evaluation of silicon nitride as a diffusion barrier for Gd-Si-Ge films on silicon," *Surface and Coatings Technology*, vol. 200, no. 5-6, pp. 1335–1340, 2005.

[105] Z. L. Wang, D. Ugarte, W. A. Heer, P. Vincent, C. Journet, V. T. Binh, M. Poot, H. S. J. V. D. Zant, A. Aguasca, A. Bachtold, K. Kim, A. Zettl,

P. Hung, H. W. C. Postma, M. Bockrath, X. Blase, and S. Roche, "only appears when looking at the I," *Science*, vol. 325, no. August, pp. 1110–1114, 2009.

[106] J. H. Van Driel and O. De Jong, "Investigating the development of pre-service teachers' pedagogical content knowledge," *Annual Meeting of the National Association for Research and Science Teaching*, vol. 56, no. 9, 2001.

[107] L. Abelmann, S. Porthun, M. Haast, C. Lodder, A. Moser, M. E. Best, P. J. Van Schendel, B. Stiefel, H. J. Hug, G. P. Heydon, A. Farley, S. R. Hoon, T. Pfaffelhuber, R. Proksch, and K. Babcock, "Comparing the resolution of magnetic force microscopes using the CAMST reference samples," *Journal of Magnetism and Magnetic Materials*, vol. 190, no. 1-2, pp. 135–147, 1998.

[108] A. Edelstein, "Advances in magnetometry," *Journal of Physics Condensed Matter*, vol. 19, no. 16, 2007.

[109] D. O. Smith, "Development of a vibrating-coil magnetometer," *Review of Scientific Instruments*, vol. 27, no. 5, pp. 261–268, 1956.

[110] S. Foner, "Versatile and sensitive vibrating-sample magnetometer," *Review of Scientific Instruments*, vol. 30, no. 7, pp. 548–557, 1959.

[111] V. K. Pecharsky and K. A. Gschneidner, "Gd 5 (Si x Ge 1 ± x) 4 : An Extremum Material **," *Advanced Materials*, vol. 13, no. 9, pp. 683–686, 2001.

[112] Y. Mozharivskyj, A. O. Pecharsky, V. K. Pecharsky, and G. J. Miller, "On the high-temperature phase transition of Gd5Si 2Ge2," *Journal of the American Chemical Society*, vol. 127, no. 1, pp. 317–324, 2005.

[113] J. Lyubina, *Magnetocaloric Materials*, novel func ed., A. Zhukov, Ed. Springer, Cham, 2016.

[114] B. D. Josephson, "Inequality for the specific heat: II. Application to critical phenomena," *Proceedings of the Physical Society*, vol. 92, no. 2, pp. 276–284, 1967.

[115] R. S. V. Provenzano, A. Shapiro, "Inequality for the specific heat: I. Derivation," *Proceedings of the Physical Society*, vol. 92, no. 2, pp. 269–275, 1967.

[116] G. S. Rushbhooke, "On the thermodynamics of the critical region for the ising problem [4]," *The Journal of Chemical Physics*, vol. 39, no. 3, pp. 842–843, 1963.

[117] F. Kos, D. Poland, D. Simmons-Duffin, and A. Vichi, "Precision islands in the Ising and O(N) models," *Journal of High Energy Physics*, vol. 2016, no. 8, pp. 0–15, 2016.

[118] Y. C. Tseng, D. Haskel, J. C. Lang, S. Sinogeikin, Y. Mudryk, V. K. Pecharsky, and K. A. Gschneidner, "Effect of hydrostatic pressure upon the magnetic transitions in the Gd5 (Six Ge1-x) 4 giant magnetocaloric compounds: X-ray magnetic circular dichroism study," *Physical Review B - Condensed Matter and Materials Physics*, vol. 76, no. 1, pp. 3–8, 2007.

[119] A. M. Pereira, A. M. Dos Santos, C. Magen, J. B. Sousa, P. A. Algarabel, Y. Ren, C. Ritter, L. Morellon, M. R. Ibarra, and J. P. Araújo, "Understanding the role played by Fe on the tuning of magnetocaloric effect in Tb5 Si2 Ge2," *Applied Physics Letters*, vol. 98, no. 12, pp. 8–11, 2011.

[120] L. Morellon, Z. Arnold, C. Magen, C. Ritter, O. Prokhnenko, Y. Skorokhod, P. A. Algarabel, M. R. Ibarra, and J. Kamarad, "Pressure enhancement of the giant magnetocaloric effect in Tb 5Si2Ge2," *Physical Review Letters*, vol. 93, no. 13, pp. 1–4, 2004.

[121] R. L. Hadimani, Y. Melikhov, J. E. Snyder, and D. C. Jiles, "Anomalous behavior in electrical transport properties in single-crystal Gd5Si1.8Ge2.2 and polycrystalline Gd 5Si2.09Ge1.91," *IEEE Transactions on Magnetics*, vol. 45, no. 10, pp. 4368–4371, 2009.

[122] D. Vollath, *Nanomaterials : An Introduction to Synthesis, Properties and Applications.* Wiley VCH, 2013.

[123] A. O. Pecharsky, K. A. G. Jr, and V. K. Pecharsky, "The giant magnetocaloric effect between 190 and 300 K in the Gd 5 Si x Ge 4 À x alloys for 1 . 4 p x p 2 . 2," *J. Phys.: Condens. Matter*, vol. 267, no. 1604, pp. 60–68, 2003. [Online]. Available: http://iopscience.iop.org/0953-8984/16/9/010

[124] R. Bjørk, C. R. H. Bahl, and M. Katter, "Magnetocaloric properties of LaFe13-x-yCoxSi y and commercial grade Gd," *Journal of Magnetism and Magnetic Materials*, vol. 322, no. 24, pp. 3882–3888, 2010. [Online]. Available: https://arxiv.org/pdf/1410.1988.pdf

[125] K. Lowe, J. Liu, K. Skokov, J. D. Moore, H. Sepehri-Amin, K. Hono, M. Katter, and O. Gutfleisch, "The effect of the thermal decomposition reaction on the mechanical and magnetocaloric properties of La(Fe,Si,Co) 13," *Acta Materialia*, vol. 60, no. 10, pp. 4268–4276, 2012. [Online]. Available: http://dx.doi.g/10.1016/j.actamat.2012.04.027

[126] V. Lollobrigida, V. Basso, F. Borgatti, P. Torelli, M. Kuepferling, M. Coïsson, E. S. Olivetti, F. Celegato, L. Tortora, G. Stefani, G. Panaccione, and F. Offi, "Chemical, electronic, and magnetic structure of LaFeCoSi alloy: Surface and bulk properties," *Q*, vol. 115, no. 20, 2014. [Online]. Available: http://dx.doi.org/10.1063/1.4879195http: //aip.scitation.org/toc/jap/115/20

172

[127] F. Wang, J. Zhang, Y. Chen, G. Wang, J. Sun, S. Zhang, and B. Shen, "Spin-glass behavior in La(Fe1xMnx)11.4Si1.6 compounds," *Phys. Rev. B*, vol. 69, 2004.

[128] T. Palstra, G. Nieuwenhuys, J. Mydosh, and K. Buschow, "Mictomagnetic, ferromagnetic, and antiferromagnetic transitions in La(FexAl1x)13 intermetallic compounds," *Phys. Rev. B*, vol. 31, 1985.

A

Appendix

All codes, scripts and sequence files written and used for this thesis are available online at the following git repositories:

- AFM grain-size estimation:

  https://github.com/Mewapt/PhD/tree/master/GitPhDUpload/AFM

- SQUID data reader:

  https://github.com/Mewapt/PhD/tree/master/SQUIDReader

- Ising simulation code:

  https://github.com/Mewapt/PhD/tree/master/Ising

- sequence files:

  https://github.com/Mewapt/PhD/tree/master/SQUIDSequenceFiles

XRD parameters for GSG samples:

Phase Name	Space Group	Source	DB Card Number
SiO2	1m-3m	Crystallography Open Database	200383
Gd2Ge2O7	P1	Crystallography Open Database	35183
Gd2Si2O7	P-1	Crystallography Open Database	389660
Gd5Ge2Si2	Pnma	Crystallography Open Database	149051

<div align="right">B</div>

Acronyms and Abbreviations

- AFM: Atomic Force Microscopy

- BCE: Baro-Caloric Effect

- CCD: Charge-Coupled Device

- ECE: Electro-Caloric Effect

- EMF: Electro-Motive Force

- FM: FerroMagnetic

- FOPT: First Order Phase Transition

- GSG: Gadolinium Silicon Germanium - $Gd_5(Si_xGe_{1-x})_4$ $where,$ $0 \leq x \leq 1$

- GECE: Giant Electro-Caloric Effect

- GMCE: Giant Magneto-Caloric Effect

- LCR: Inductor-Capacitor-Resistor

- LFS: Lanthanum Iron Silicon - $La(Fe, Si)_{13}$

- LFSC: Lanthanum Iron Silicon Cobalt - $La(Fe, Co, Si)_{13}$

- MC: Magneto-Caloric

- MCE: Magneto-Caloric Effect

- MFM: Magnetic Force Microscopy

- Mono: Monoclinic

- Ortho: Orthorhombic

- PLD: Pulsed Laser Deposition

- PNR: Polarised Neutron Reflectometry

- PM: ParaMagnetic

- RE: Rare Earth

- RKKY: Ruderman Kittel Kasuya Yosida

- SOPT: Second Order Phase Transition

- SQUID: Super-conducting QUantum Interface Device

- VSM: Vibrating Sample Magnetometer

- XRD: X-Ray Diffraction

- XRR: X-Ray Reflectometry

C

Copyrights and Permissions